universität wien

MASTERARBEIT

Titel der Masterarbeit

„Petrography and Geochemistry of Eocene Cold – Seep Carbonates from Washington State, USA“

Verfasser

Daniel Smrzka, BSc.

angestrebter akademischer Grad

Master of Science

Wien, 2013

Studienkennzahl lt. Studienblatt:	A 066815
Studienrichtung lt. Studienblatt:	Erdwissenschaften
Betreuer	Univ.-Prof. Dr. Jörn Peckmann

This work is dedicated to my loving girl, friend and companion Jennifer…

without you, this journey would be unwritten

Contents

1 - Introduction

The ultimate carbon source of benthic organisms dwelling in the subsurface of seafloor sediments is derived from the photic zone of the oceans, where primary producers use light and inorganic carbon to synthesize organic matter (Berger et al., 1989; Rullkötter, 2006). When these planktic photoautotrophs and zooplankton die, only a small fraction of their remains reach the seafloor, whereby the bulk is oxidized in the water column (Emerson and Hedges, 1988; Wakeham and Lee, 1989; Rullkötter, 2006). With time, these organic molecules are buried and altered in the sedimentary realm and are used as a carbon source by microorganisms (e.g. Müller and Suess, 1979; Martens and Klump, 1984; Martens et al., 1992).

Over the last few decades, one of the most exciting discoveries in the field of marine science was the existence of chemosynthesis – based faunal communities and authigenic carbonate deposits related to hydrocarbon gas seepage activity at the seafloor (e.g. Paull et al., 1985; Kulm et al., 1986; Beauchamp and Von Bitter, 1992). A whole array of publications followed this discovery and interest increased rapidly. As of today, the chemical, biological and geological mechanisms controlling the functioning of these ecosystems and the genesis these deposits are fundamentally understood, even though there are aspects which remain enigmatic. Methane-seep deposits are primarily carbonate rocks, which owe their origin to microbial activity of organisms at the seafloor (Ritger et al., 1987). Seafloor sediments are habitats for a large variety of different micro and macroorganisms, which utilize different electron acceptors for their metabolism (Jørgensen, 2006). This is demonstrated by different concentrations of these terminal electron acceptors in different sediment depths, which gives the seafloor sediments their typical zonation (Froelich et al., 1979). The energy yield between the carbon source (electron donor) and the electron acceptor decreases with sediment depth. One reason for this is that organic molecules alter with depth and become more refractory. Furthermore, the different terminal electron acceptors used yield different amounts of usable energy for metabolism (Jørgensen, 2006). Nonetheless, organisms are able to metabolize at conditions where energy yields are extremely low. Methanogenesis is such a process, which occurs within the anoxic layers of seafloor sediments (e.g. Claypool and Kvenvolden, 1983; Jørgensen and Kasten, 2006; Reeburgh, 2007). There are two main origins of methane in marine sediments, a thermogenic and a biogenic origin. The former requires higher temperatures and pressures for its generation and is therefore produced deeper within the sediment (e.g. Claypool and Kaplan, 1974; Sassen et al., 1999; Milkov et al., 2005). The latter is generated by microorganisms at shallower depth as a result of fermentative decomposition of organic matter and autotrophic production with hydrogen and carbon dioxide (Claypool and Kaplan, 1974; Whiticar et al., 1986). Methane produced by both sources is one of the two key elements in the generation of seep carbonates

(Elvert et al., 1999; Aharon and Fu, 2000). This methane rises towards the seafloor via advective or diffusive flow (Ritger et al., 1987), the rate of which is largely dependent on the rate of its generation (e.g. Regnier et al., 2011). The second key element, sulfate, is derived by influx of seawater (Henrichs and Reeburgh, 1987). Compared to hydrothermal vents, hydrocarbon seeps maintain fluid flow over long periods of time and provide a relatively steady supply of methane due to the long-term accumulation, compaction and over-pressuring of pore waters rich in organic matter (Sibuet and Olu, 1998). The methane produced from below migrates upwards through the sediment column and is oxidized with sulfate (Reeburgh, 1980; Devol and Ahmed, 1981; Devol et al., 1984). This process, the anaerobic oxidation of methane via sulfate reduction (AOM) is the driving force of seep carbonate formation (e.g. Ritger et al., 1987; Suess and Whiticar, 1989; Peckmann et al., 1999) and this reaction proceeds according to the following net equation (Martens and Berner, 1974):

$$CH_4 + SO_4^{2-} \rightarrow HCO_3^- + HS^- + H_2O \qquad (1)$$

This consumption of methane by anaerobic oxidation in marine sediments tends to be especially intense in a narrow zone termed the sulfate-methane transition zone, SMTZ, where methane and sulfate concentrations overlap (Barnes and Goldberg, 1976; Reeburgh, 1976; Iversen and Jørgensen, 1985). It is interesting to note that most microorganisms are not capable of carrying out equation (1) alone, yet certain anaerobic methanotrophic organisms (ANME – 1) seem to be an exception to do so. Through use of modern molecular methods a large diversity of archaea (Orphan et al., 2002; Knittel et al., 2005) and sulfate reducing bacteria (Boetius et al., 2000; Orphan et al., 2001) has been discovered over the last two decades, which are associated with the anaerobic oxidation of methane in marine sediments. As of today, it is confirmed that AOM is a microbially mediated process carried out by a syntrophic association of methane oxidizing archaea and sulfate reducing bacteria (Hinrichs et al., 1999; Boetius et al., 2000; Knittel and Boetius, 2009). This biogeochemical reaction changes the chemistry of sedimentary porewaters by raising bicarbonate and bisulfide concentrations. By production of bicarbonate, alkalinity increases, lowering the solubility of calcium carbonate, which commonly results in the immediate precipitation of carbonate minerals under these conditions (Ritger et al., 1987; Wallmann et al., 1997) according to the following equation (Baker and Burns, 1985):

$$2HCO_3^- + Ca^{2+} \rightarrow CaCO_3 + CO_2 + H_2O \qquad (2)$$

This carbonate precipitation only occurs when the pore fluids of the sediments become sufficiently supersaturated with respect to the carbonate phase and if precipitation is not inhibited by kinetic factors (Burton, 1993). The carbonate precipitates produced this way are referred to a being biologically-induced, indicating that their genesis stems not from enzymatically-controlled biomineralization, but from changing chemical conditions produced microbial activity (Flügel, 2004). The primary carbonate phase precipitated in this environment is microcrystalline calcite, also termed micrite. Further minerals typically associated with the anaerobic oxidation of methane in seafloor sediments are iron sulfides, primarily iron monosulfides, which are subsequently transformed into pyrite (e.g. Berner, 1970; Berner, 1984; Rickard et al., 1995). When the process of AOM was first investigated, these sulfide minerals were important indicators that the methane involved in the formation of these carbonates was not being oxidized in the presence of oxygen (Ritger et al., 1987). Ferrous iron is the main form of dissolved iron in anoxic seawater (Millero et al., 1995) and therefore also present at sites where cold-seep carbonates are produced. Iron sulfides are important sinks for both sulfur and iron and are an integral part of the global cycles of both elements (e.g. Berner, 1970; Canfield et al., 1992; Jørgensen and Kasten, 2006). A further significant phenomenon observed in relation to hydrocarbon-seep carbonates – which received surprisingly little attention to date – is silicification (Himmler et al., 2008; Kuechler et al., 2012). The silica necessary for this process may either be volcanogenic or biogenic in origin (Kuechler et al., 2012). Silica phases are particularly abundant in the seep limestones studied here and are therefore one of the main topics of this thesis.

The most prominent occurrences of ancient seep deposits so far have been discovered in the United States, New Zealand, Japan and Italy (e.g. Peckmann et al., 1999; Campbell et al., 2002; Torres et al., 2003; Campbell, 2006). A distinctive set of faunal assemblages and petrographic features typical for modern seeps has been identified as being equally characteristic for ancient seep sites. These properties have been used to identify ancient seep sites in the field as well as under the microscope. The history of their discovery at the study location in western Washington State began in 1979 (Kiel, 2010), when similar fossil assemblages were discovered in various formations including the Bear River Deposit, Humptulips Formation, Lincoln Creek Formation and Astoria Formation (Goedert and Squires, 1990; Squires and Goedert, 1991; Goedert et al., 2000; Peckmann and Goedert, 2005). Most prominent macrofossils include chemosymbiotic vesicomyid bivalves, hexactinellid sponges (Rigby and Goedert, 1996), neomphalid gastropods, vestimentiferan tube worms (e.g. Goedert et al., 2000) and galatheid crustaceans (Schweitzer and Feldmann, 2008). Consequently, these deposits have evoked interest of researches leading to several publications on ancient seeps in western Washington State (e.g. Peckmann et al., 2002, 2003; Kuechler et al., 2012). This thesis concentrates two

previously undescribed seep deposits found in the Siltstone of Shoalwater Bay Formation in southwestern Washington State, USA. One site is located at the shore of the Columbia River, the other at Willapa Bay. The study uses petrographical observations made on this sections, isotopic analysis and numerical experiments to interpret the origin of the carbonate and silicate minerals. The ultimate goal is to reconstruct the environments of mineral formation with a specific focus on silicification.

2 – Locality

The name of the formation enclosing the seep deposits is Siltstone of Shoalwater Bay, located in the Pacific Northwest of the United States. Rock samples have been collected from two locations: Willapa Bay to the North and Knappton to the South at the northern shore of the Columbia River (Fig. 9).

2.1 – General geology

The tectonic unit in which most fossil seep deposits are found in western Washington is the Coast Range Terrane, consisting of early Eocene basalts overlain by a thick cover of middle Eocene to early Miocene sediments (Brandon and Calderwood, 1990; Stewart and Brandon, 2004). The seep-bearing sediments of this terrane were deposited before and after the onset of the subduction of the Juan de Fuca

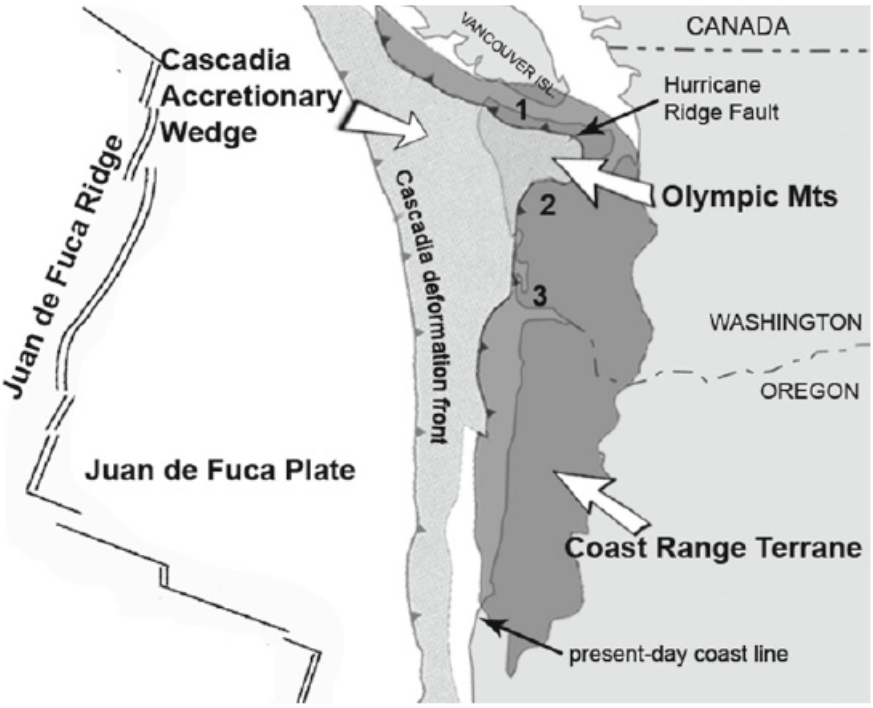

Figure 1: Sketch of the tectonic setting of the Pacific Northwest. Fossil seep sites are found in the Makah and Pysht Formations (1), Humptulips Formation and the northern part of the Lincoln Creek Formation (2) and the Astoria and Lincoln Creek Formations along the shore of the Columbia River (3) (Kiel 2010, redrawn from Stewart and Brandon 2004).

plate beneath the North American plate around 35 million years ago, implying that the oldest seep carbonates were deposited on a passive continental margin, whereas all younger seep deposits formed in an active subduction-related setting (Kiel, 2010).

The exhumation of the Coast Range terrane began around 15 million years ago when the NNW trending Cascadia subduction zone acquired its modern arched shape. This subduction zone is concave seaward, unlike most subduction zones (including the Aleutian and Java trenches), which are concave toward the arc (Kiel, 2010). The subducting slab of the Juan de Fuca plate is responsible for the uplift of the Olympic Mountains (Brandon and Calderwood, 1990). While these mountains were uplifted, the seep-bearing sedimentary cover was uplifted as well and, due to ongoing exposure and erosion, these sediments of the Coast Range terrane now crop out in a horseshoe-like fashion around the Olympic Mountains (Kiel, 2010).

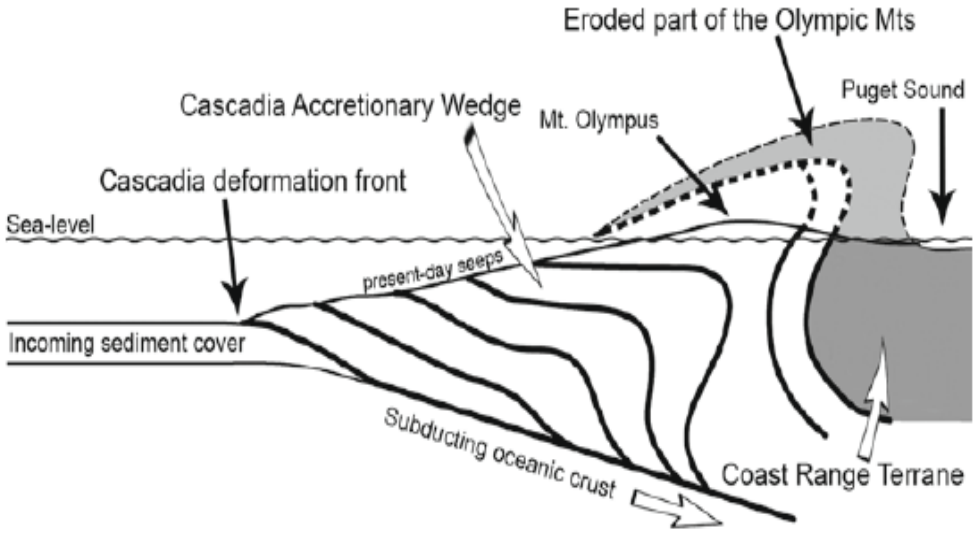

Figure 2: Cross section through the Cascadia subduction zone (Kiel 2010, redrawn from Stewart and Brandon, 2004).

Subduction of the Juan de Fuca plate underneath the North American plate was the origin of compressive forces during the Eocene in south-western Washington (Kiel, 2010). In response to these forces, subsurface methane-rich waters were squeezed towards the sediment-water interface, allowing an array of chemosynthetic and chemosymbiotic organisms to thrive.

2.2 – Siltstone of Shoalwater Bay

The Siltstone of Shoalwater Bay is part of the larger Late to Middle Eocene Siltstone and Sandstone unit, which have been described as thin-bedded, laminated concretionary siltstones and fine micaeous sandstones (Wells 1989). The Siltstone of Shoalwater Bay Formation is the youngest subunit of the Late to Middle Eocene Silt and Sandstone unit, and has been described as embodying dark grey, thin-bedded, laminated, indurated tuffaceous siltstones containing thin tuff beds, minor thin-bedded feldspathic sandstone and calcareous concretions (Wells, 1989). It is Late Eocene in age and lies in between an unconformity to the top and the Siltstone and Sandstone at Omeara Point (Wells, 1989). The Siltstone of Shoalwater Bay subunit extends from the shore of the Columbia River at Knappton (46-16'35'' N, 123-48'54'' W, see Figs. 3 and 4) to the northwest up to Omeara Point (46° 24' 07" N, 123° 57' 03" W; Figs. 3 & 4), and to the North reaching the mouth of the Naselle River. At Knappton, it lies adjacent to numerous Holocene and Pleistocene landslide deposits comprising poorly sorted colluvium and bedrock slump blocks (Fig. 4, Wells, 1989). Furthermore, the deposits lie in the proximity of Holocene fluvial, estuarine and shoreline deposits. These are characterized by unconsolidated silt, sand and gravel alluvium deposited upon the Northern bank of the Columbia River (Wells, 1989; Goedert and Benham, 2003).

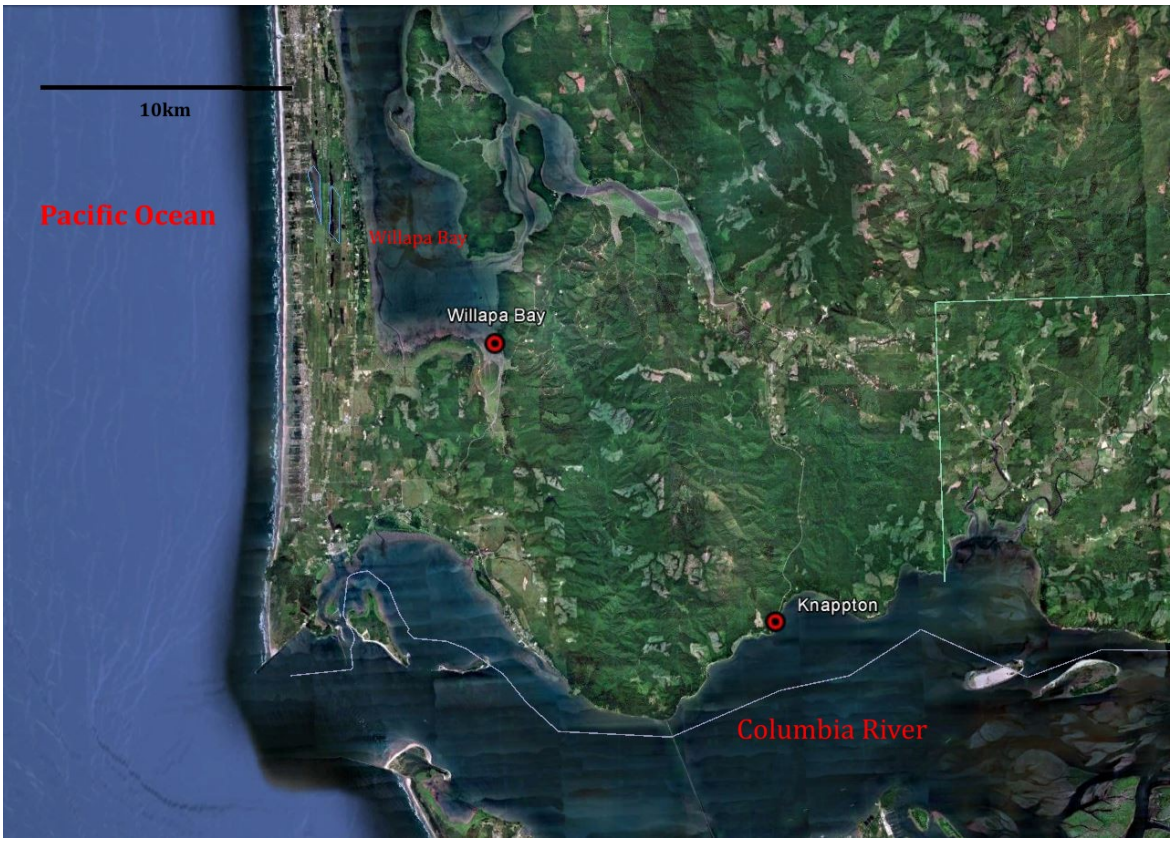

Figure 3: Topographic map of Knappton and Willapa Bay, picture taken from Google Earth

Figure 4: Geologic map of the Cape Disappointment – Naselle River area, Pacific and Wahkiakum counties, Washington

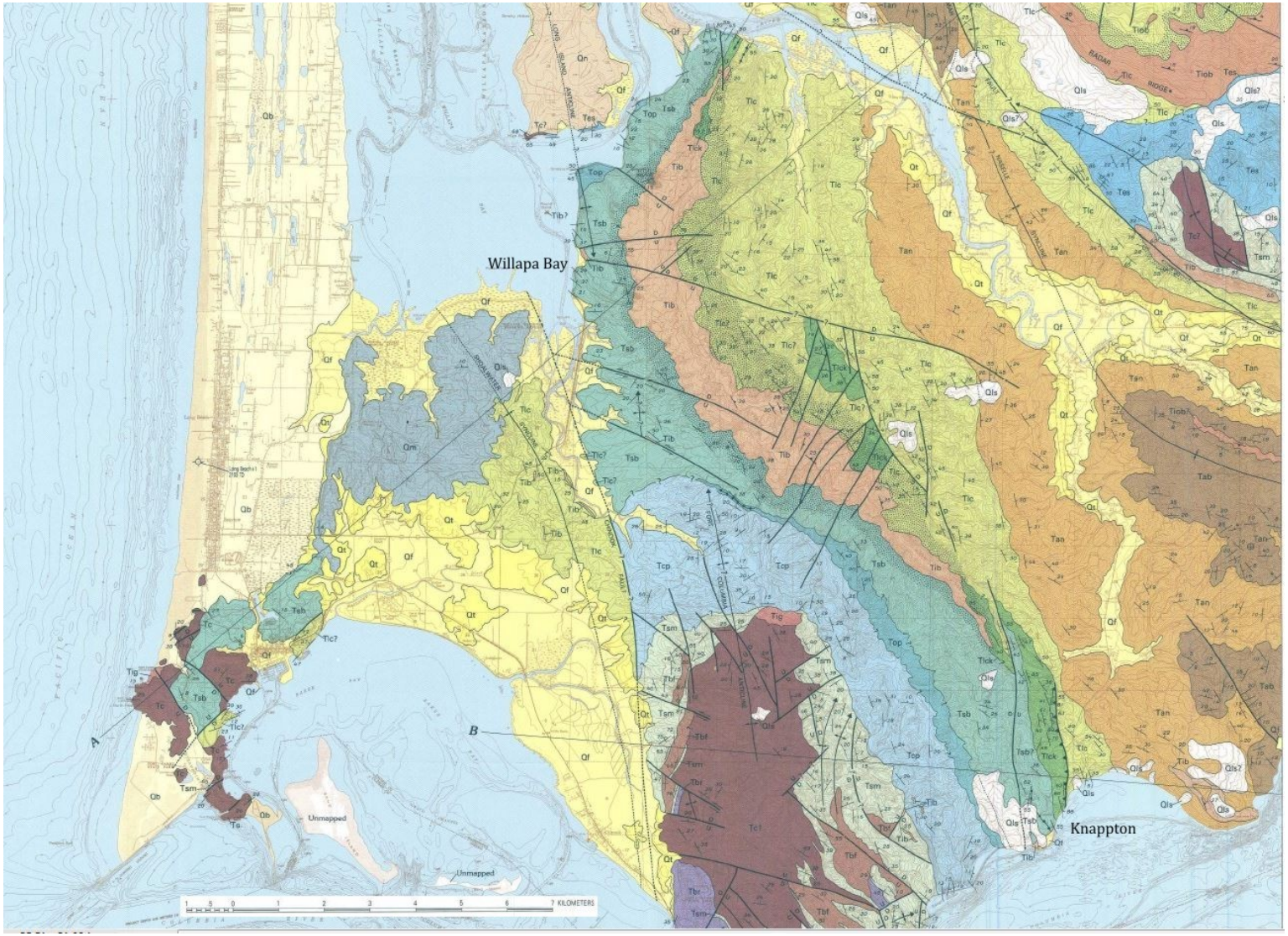

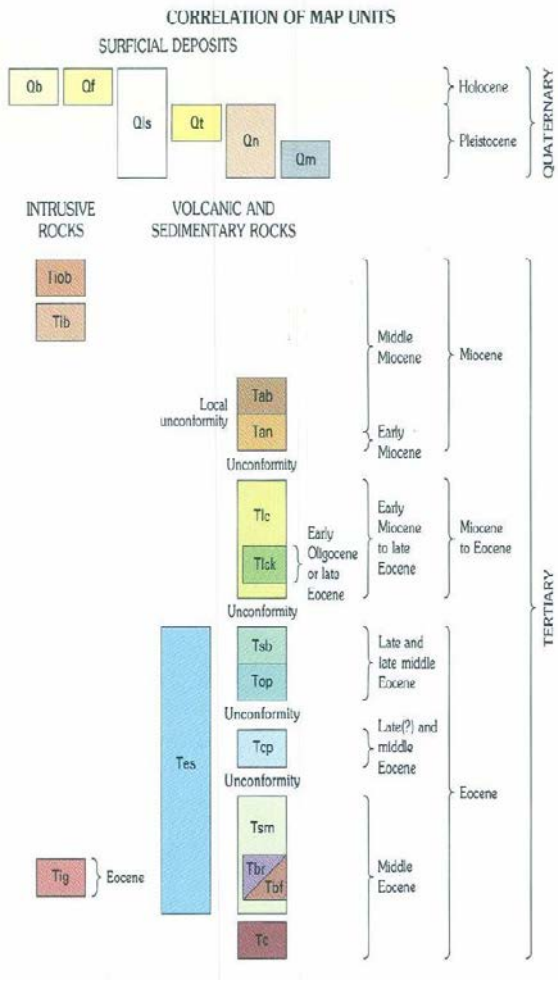

Wells, 1989

Tes Sandstone unit at Knappton (early Oligocene or late Eocene)

Tsb Siltstone and Sandstone at Omeara Point (late and middle Eocene)

Tlck Siltstone and Sandstone (late and middle Eocene)

Top Siltstone of ShoalwaterBay (late and middle Eocene)

3 – Materials and methods

3.1 – Sample collection and preparation

Rock samples were kindly provided by James L. Goedert of the Burke Museum of Natural History and Culture in Seattle. Most samples were not collected in-situ, but as lag material on river and shore-bank exposures or from strata above the beach transported downslope by recent landslides (Goedert and Benham, 2003; Kuechler et al., 2012). Knappton samples were collected at 46° 16.490 N, 123° 48.929 W, Willapa Bay samples at 46° 22.716 N, 123° 57.206 W (Fig. 3). Thin sections of each sample were prepared by Leopold Slawek at the University of Vienna in 150 x 100 mm size for standard petrographic and fluorescence analysis. Petrographic and fluorescence observations were carried out with a Nikon SMZ 1500 stereomicroscope coupled to a Prog.Res Speed XT core 5 camera, as well as a Nikon Optiphot – 2 optical microscope. For image analysis and camera control, the software Prog.Res Capture pro 2.8 was used. Samples for oxygen and carbon stable isotopes were taken from polished slabs using a handheld micro-drill at low rotational speed. These samples were analyzed at the light stable isotope laboratory of the Institute of Earth Sciences, Karl-Franzens University, Graz by Dr. Sylvain Richoz. Effective accuracy was ± 0.05 for $\delta^{13}C$ values and ± 0.11 for $\delta^{18}O$ values. All values are reported in per mil relative to the Vienna PeeDee Belemnite (V-PDB) standard. Reproducibility was checked by replicate analysis of each sample; samples with larger differences than ± 0.1 for $\delta^{13}C$ values and ± 0.2 for $\delta^{18}O$ values were designated as indicative of heterogeneity.

3.2 – Numerical experiments

The PHREEQC code (Parkhurst and Appelo, 1999) was used to simulate chemical reactions in a sediment column. The experiments incorporate aqueous equilibrium speciation, heterogeneous reactions, irreversible and kinetically controlled reactions and calculate solutions and saturation indices. They were used for batch and reactive transport calculations. For all numerical experiments, the standard "PHREEQC" –database was used (Parkhurst and Appelo, 1999). The program calculates heterogeneous reactions with solid phases under thermodynamic consideration only; however kinetic rate laws can be entered to account for precipitation and dissolution rates of minerals, which were applied to the numerical reaction – transport experiments. The PHREEQC software was used to perform numerical experiments in order to explore the relevance of geochemical mechanisms and reactions in the context of AOM. It was not intended to perform a full modeling exercise of an AOM environment.
As initial input solution for the numerical batch experiments, following parameters were used:

Input solution:

GeoB 13126-1	[mmol/L]
pH	7.55
H_2S	0.37
SO_4^{2-}	27.49
P	$2.29*10^{-3}$
Cl	572.7
Si	0.041
Fe(II)	$3.76*10^{-4}$
Ca	9.48
Mg	51
K	10.476
Sr	0.0752
Ba	$6.3*10^{-4}$
Al	0.140

Table 1: Porewater values from Congo pockmarks.
Data from Zabel et al., 2008, all values in mmol/L except pH.

This input solution was measured at ~3500 m water depth at the sediment-water interface. pH values were measured in a parallel *core*. Porewater temperatures were not measured and assumed to be 8°C for batch reaction calculations. Alkalinities were not given for this core, however values between 2 and 20 mmol/l were measured at similar seep sites (Zabel et al., 2008) and a value of 4.8 mmol/l was adopted. Na^+ was not measured and an assumed value of 350 mmol/L was used for charge balance.

Equilibrium phase assemblage

PHREEQC accepts quantitative information on the solid phases reacting with the aqueous solution. It further allows precipitation and dissolution of solids and keeps track of the concomitant changes of the solids concentration corresponding to a porewater mass of 1 kg. This can be re-calculated based on the density, sediment porosity, density of water and the solid phase and the formula weight of the solids. A sediment porosity of 0.8 was adopted, a value common for marine sediments (e.g. Luff and Wallmann, 2003; Linke et al., 2005). The mean density of the marine sediment matrix was assumed to be an averaged density of common clay minerals and set to 2.4 g/cm^3. All phases were related to this density and the amount in moles was used as initial phase assemblage. Initial amounts of phase assemblages present in the sediment were ~15 wt% $CaCO_3$ (Gross, 1965) and 33 wt% biogenic silica (Van Cappellen and Qiu, 1997a). These values were re-calculated to give 0.722 and 2.635 moles/L for calcite and silica respectively. Calcite and amorphous silica representing biogenic silica were considered to be present in the sediment before AOM. The initial solution (previous section) was equilibrated

with the phase assemblage before considering anaerobic oxidation of methane.

Anaerobic oxidation of methane

The kinetically controlled AOM reaction (1) below or its rate-law was not explicitly included in the simulation, but was included by irreversible additions of its reaction products to the aqueous solution under consideration of reaction stoichiometry and charge balance. The rate of addition of reaction products corresponds to the AOM rate.

$$CH_4 + SO_4^{2-} \rightarrow HCO_3^- + HS^- + H_2O \qquad (1)$$

The reaction products added are bicarbonate and bisulfide. Adding two anions requires the addition of either one cation with two positive charges or two cations with one positive charge. Sodium and calcium ions were added to maintain charge balance, whereby Ca^{2+} was added based on the average seawater SO_4^{2-}/Ca^{2+} ratio of 1:0.343 (using data from Culkin and Cox, 1966 and Morris and Riley, 1966). The addition of ions to solution without efflux of ions leads to an increase of the ionic strength of the solution. Due to the high ionic strength of seawater this increase was relatively small so that the effects were neglected in the numerical batch experiments. The amount of moles of the AOM products added to solution was re-calculated from measured methane fluxes from Hydrate Ridge off the coast of Oregon (Torres et al., 2002). Methane flux rates of 30-100 mmol/m^2/d were measured at bacterial mats and rates up to 10^6 mmol/m^2/d at thrust faults. A mean methane flux value of 50 mmol/m^2/d was derived from these values and applied to the numerical batch experiments. The flux values were re-calculated to apply them to the sediment cube (corresponding to1 kg pore water) on which the numerical calculations are based (see above). One surface of this cube has an area of 0.0129 m^2 and measured methane flux values were related to this area to obtain amounts of methane per time with respect to the model parameters. Re-calculating 50 mmol/m^2/d gave $5.645*10^{-4}$ moles/d and 0.206 moles/year for an area of 0.0129 m^2.

Experimental procedure

The initial solution (table 1) was equilibrated with the solid phase assemblage calcite and amorphous silica. To consider CO_2 degassing, the solution was in turn equilibrated with a gas phase containing 0.7 mole% carbon dioxide gas (amounts from Römer et al., 2012). AOM was added in every experiment in 20 incremental steps for time periods of one month and, subsequently, one year. Na^+ was added in turn with and without Ca^{2+}. Ca^{2+} was added with respect to seawater/sulfate ratio as described above. Effects on pH, calcite precipitation and dissolved Ca^{2+} in solution were graphed; all data are listed in the appendix.

3.3 – Reaction – transport experiments

Concept and solution compositions

For reaction transport calculations with PHREEQC, two solutions were defined. The model cube represents a sediment column with an initial solution present. A second solution streams through this column whereby chemical reactions and species distributions during flow are calculated. The model sediment column has a height of 10.6 cm, a volume of 1.2 dm^3 and each square surface of the cube has an area of 0.01129 m^2. This corresponds to the cell dimensions used by the program to calculate transport. The fluid entering the sediment column is sulfidic sedimentary porewater representing methane and AOM flux from below. The solid phase assemblage is present in the cell and the inflowing fluid was allowed to equilibrate with the respective phases as it passed through the column. The compositions of seawater and the inflowing fluid are given below:

Parameter	Value [mmol/L]	Source
pH	8.1	Assumed for seawater
Temperature	8	Assumed for seawater
Alkalinity	2.26	(Bradshaw et al., 1981)
Na	469	(Culkin and Cox, 1966)
Mg	52.8	(Culkin and Cox, 1966)
K	10.2	(Culkin and Cox, 1966)
Ca	10.4	(Culkin and Cox, 1966)
Cl	546	(Morris and Riley, 1966)
Fe	$8.06*10^{-7}$	(Bacon et al., 1980)
Al	$3.85*10^{-5}$	(Mackenzie et al., 1978)
Si	0.0997	(Edmond, 1974)
P	$2.87*10^{-4}$	(Tréguer and Le Corre, 1979)
Ba	$1.09*10^{-4}$	(Bacon and Edmond, 1972)
SO_4^{2-}	28.2	(Morris and Riley, 1966)
NO_3^-	0.0804	(Gundersen and Mountain, 1973)

Table 2: Composition of oxygenated seawater, temperatures in °C

Parameter	Value [mmol/L]
Alkalinity	40.57
Na	350 (not measured) *
Mg	50.8
K	16.43
Ca	5.8
Cl	537.82
Fe	$3.58*10^{-4}$
Al	0.119
Si	0.36
P	3.986
Ba	$5.42*10^{-3}$
SO_4	2.66
H_2S	16.55

*Table 3: Composition from Congo pockmarks, GeoB 13125 bottom layer, 1.3 m sediment depth Data from Zabel et al., 2008. *Assumed value for charge balance*

Fluid flux and AOM rates

Transport was assumed to be advective only and no dispersivities or diffusion coefficients were applied for the experiments. Considering the parameters of fluid flux and sediment column length, the total time required for one complete fluid exchange inside the column had to be determined. Methane flux rates from bottom waters measured at Hydrate Ridge range from 10 to 250 cm/a (Torres et al., 2002). A value within this range of 60 cm/a was applied for the reaction - transport experiments and recalculated in seconds per cell height, giving $5.724*10^6$ seconds or 66.25 days for one pore volume exchange. This value corresponds to one time step in the transport experiment. By defining the number of shifts through the cell, the total time of the simulation was determined. Several runs were simulated with different total simulation times, fluid flux rates and AOM rates. AOM flux rates were adopted from Wallmann et al., (2006) who measured 31.1mmol/m^2/d for submarine mud volcanoes in the Black Sea. This value is in the same order of magnitude comparable to other measured values reported by Dale et al., (2008; 16.3 mmol/L/d), Linke et al., (2005; 588 µmol/cm^2 /a) and Luff and Wallmann, (2003; 925 µmol/cm^2 /a). This value (31.1 mmol/ m^2 /d) was used and recalculated for the model sediment column, corresponding to $4.05*10^{-9}$ mol/0.01129 m^2/s.

Equilibrium phase assemblage

The phase assemblage in the numerical reaction-transport experiments represents phases present within the transport cell. Both solutions are therefore allowed to equilibrate with the input phase assemblage during transport. The initial solution present is oxygenated seawater, which was equilibrated with the phase assemblage described above. The equilibrium phase

assemblage is identical to the one used for the batch reaction experiments. An additional phase was defined representing biogenic silica with a higher solubility than quartz. The solubility constant was taken from the PHREEQC MINTEQ database (logK = −2.71 at 25°C, Parkhurst and Appelo, 1999)

Silica dissolution kinetics

pH dependent silica dissolution kinetics were considered during transport simulations. To accomplish this, a dissolution rate equation was used (Dove, 1994), which determines the rate of dissolution as a function of a ph-dependent change of silica surface group distribution:

$$Rate = e^{-10.7}Te^{\frac{(-66000)}{(RT)}}(\theta_{>SiOH})^1 + e^{4.7}Te^{\frac{(-82700)}{(RT)}}\left(\theta_{>SiO^-_{tot}}\right)^{1.1} \quad (3)$$

The silica dissolution rate in mol/m²/s is determined by temperature T in kelvin, $\theta_{>SiOH}$ (the fraction of surface complexes as >SiOH) and $\theta_{>SiO^-_{tot}}$(the fraction of surface complexes as >SiO⁻ plus >SiO-Na⁺). The equation gives the concentrations of surface reactants in units of moles per m², the standard state for ΔH_{xp} and ΔS_{xp}, the experimentally determined apparent enthalpy and entropy is chosen for 1 mole of surface sites per m² (Dove, 1994). A summary of constants obtained from regression fits of over 250 dissolution rate measurements using equation (3) are given in Dove (1994). This equation is an empirical description of quartz dissolution kinetics, its properties suggesting robustness and applicability over a wide range of pH values and temperatures (Dove, 1994). The surface complex distributions for equation (3) used in the numerical reaction-transport experiments were taken from Dove 1994 for a 0.5 mole sodium solution and are listed below:

pH range	**Fraction >SiOH**	**Fraction >SiO_{tot}**
10.8 – 10.4	0.74298	0.25737
10.4 – 10	0.76641	0.23390
10 – 9.6	0.78958	0.21069
9.6 – 9.2	0.81244	0.18780
9.2 – 8.8	0.8349	0.16530
8.8 – 8.4	0.85687	0.14330
8.4 – 8	0.87822	0.12191
8 – 7.6	0.89877	0.10133
7.6 – 7.2	0.91828	0.08179
7.2 – 6.8	0.93642	0.06364

Table 4: Calculated surface complex distributions for a 0.5 molar sodium solution using equation (3); data from Dove (1994).

The temperature using equation (3) in all numerical reaction-transport experiments was set to 281.15°K or 8°C.

Reactive surface area

Equation 3 normalizes the dissolution rate to the reactive surface area (in m^2) of silica. Therefore, the rate must be related to the reactive surface area of silica in the phase assemblage of the modeled sediment column. Specific surface areas of biogenic silica predominantly fall within the range of 25 – 250 m^2/g (Dixit et al., 2001) and biogenic silica surface areas have been reported using the N_2 BET method for biosiliceous ooze (101 m^2/g; Dixit and Van Cappellen, (2002)). However, silica dissolution rates are not only dependent on total specific surface area available, but also on the intrinsic reactivity of the exposed silica surfaces (Stumm, 1992). Previous work on silica solubility and dissolution rates has shown that this surface reactivity decreases with sediment depth (Van Cappellen and Qiu, 1997b). These observations were interpreted as progressive removal of reactive surface sites during early diagenesis (aging) (Van Cappellen et al., 2002). Aged biogenic silica particles in marine sediments exhibit lower solubilities based on their reactive surface area than fresh diatom frustules (e.g. Dixit and Van Cappellen, 2002). This decrease of reactivity was implemented in the numerical experiments in terms of a decrease of reactive surface area, while keeping the surface area normalized reaction rate constant. The question was how much of the silica in the phase assemblage can be regarded as reactive silica, i.e. how much reactive surface area is available for silica dissolution? Reactive surface areas are not easy to establish (Van Cappellen, 1996) and to determine a reasonable amount, numerical experiments were run to calibrate the reactive surface area to silica solubilities reported in the literature. Silica solubilities at 8°C and pH 8 in the range of 800 – 1200 µmol have been reported by Van Cappellen and Qiu (1997) and Dixit et al., (2001). The numerical experiment was adjusted to let silica solubilities fall into the range of measured values from the literature. Calibrating the reactive silica surface area using equation (3) revealed that 200 – 250 m^2 of silica surface area are available to react, and thereby achieve dissolved silica concentrations during the numerical experiment runs without AOM similar to those reported from Van Cappellen and Qiu (1997) or Dixit et al., (2001).

4 – Results

4.1 – Sample description – Willapa Bay

Both localities, Willapa Bay and Knappton belong to the Siltstone of Shoalwater Bay Formation. However, overall fabrics and bulk compositions are different. The fabric of Willapa Bay samples is supported by a microcrystalline calcite matrix, making up the bulk of the rock volume (Figs. 7 & 11). The bulk rock exhibits smaller and larger cavities, which have been filled by secondary phases. Furthermore, some samples are penetrated by large and small veins, which have also been filled by secondary precipitates. The matrix micrite occurs in various phases, which differ in color, texture and detrital components. The two most common micrite phases are brown and gray micrite, which are best distinguished by color as their largely homogenous textures are similar (Fig. 5). Both micrites contain detrital grains consisting of carbonate fragments. The content of pyrite varies greatly. In places large quantities of idiomorphic crystals occur. Pyrite aligned along aggregates of gray and brownish micrite and forms coatings (Fig. 5 B). Other components recognized in the micritic matrix are pieces of wood as well as shell fragments and

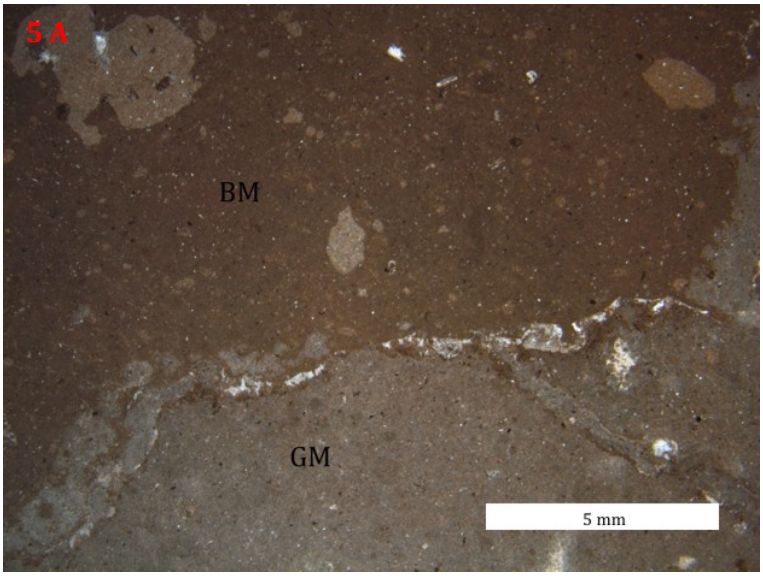

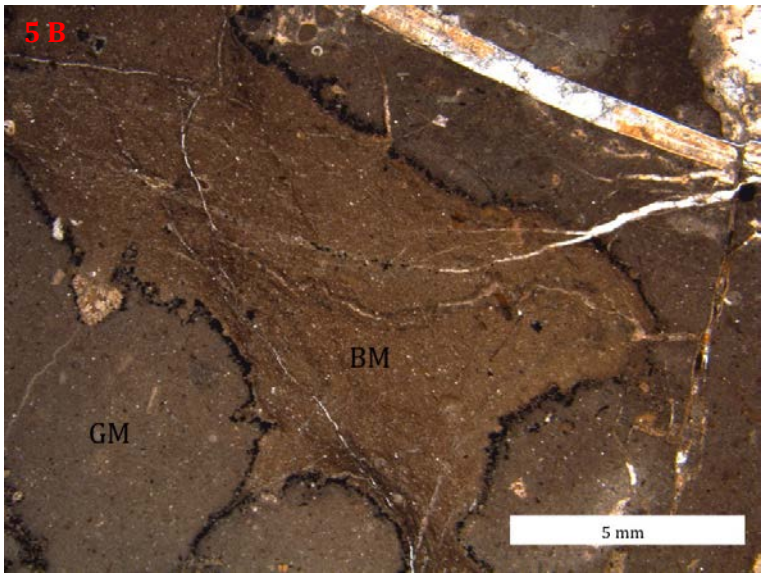

Figure 5 A: Brown (BM) and gray (GM) micrite in the Willapa Bay deposit. 5 B: Pyrite grains surrounding the boundary of both micrites.

benthic foraminifera. Besides the common homogenous (aphanitic) microcrystalline texture, some micrite reveals a peloidal texture (Fig. 6 A & B). This texture comprises oval and spherical pellets showing sharp as well as blurred boundaries. Some of the pellets are feces of decapod crustaceans belonging to the ichnogenus *Palaxius*, identified by their crescent shaped canals (Fig. 6 B).

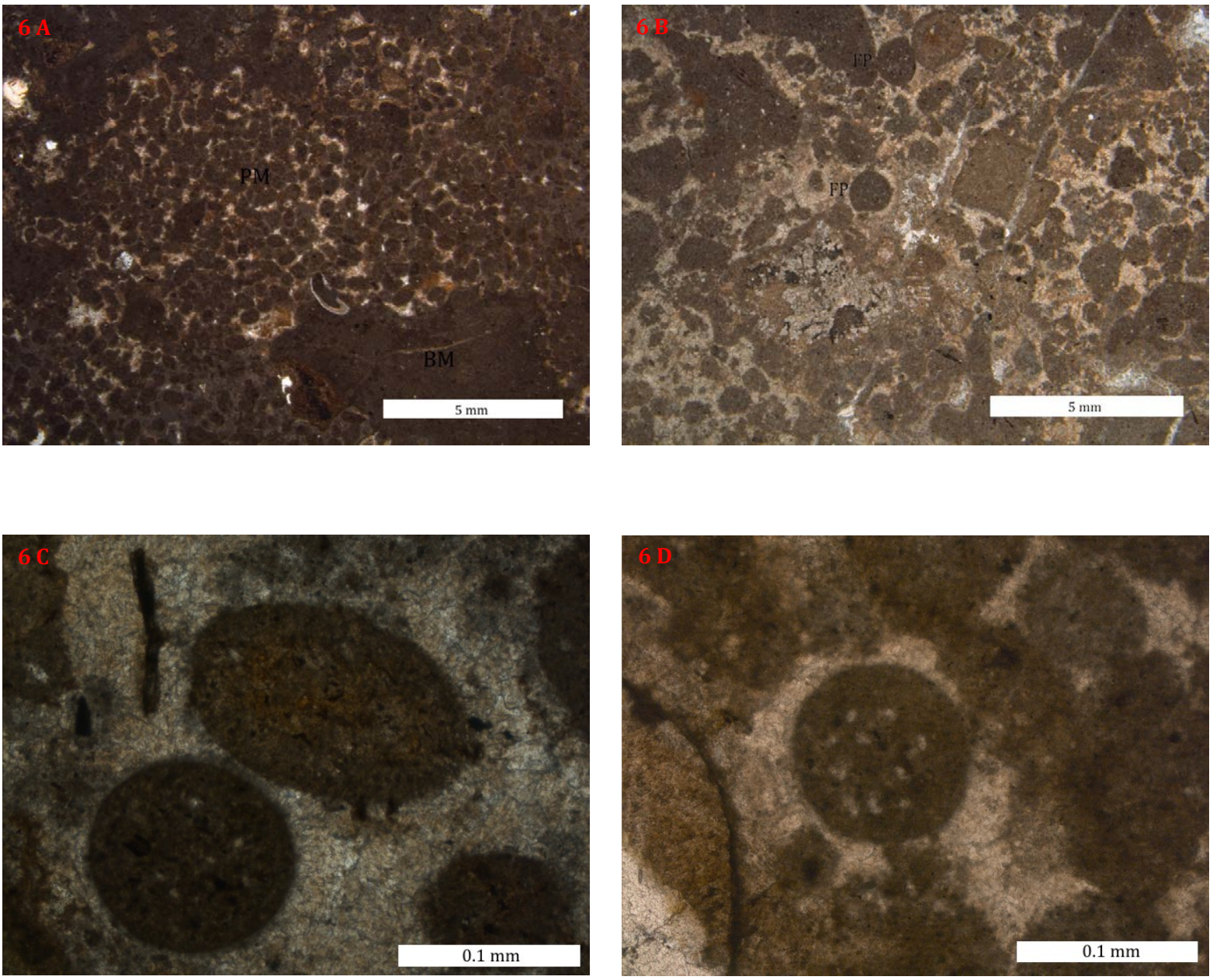

Figure 6 A: Peloidal micrite (PM) consisting of small, oval pellets enclosed by brown primary micrite (BM). 6 B: Fecal pellets (FP) within peloidal micrite. 6 C: Oval and spherical fecal pellets. 6 D: Spherical pellet with crescent – shaped voids.

Brown, gray and peloidal micrites are commonly penetrated by large burrows (Fig. 7). Gray micrite was apparently consolidated earlier on than brown micrite. The latter phase was affected by ductile deformation during early diagenesis and was injected into the rock matrix (Figs. 8 & 9). Gray micrite blocks have been squeezed together, creating structures related to pressure solution (Fig. 8 A & B).

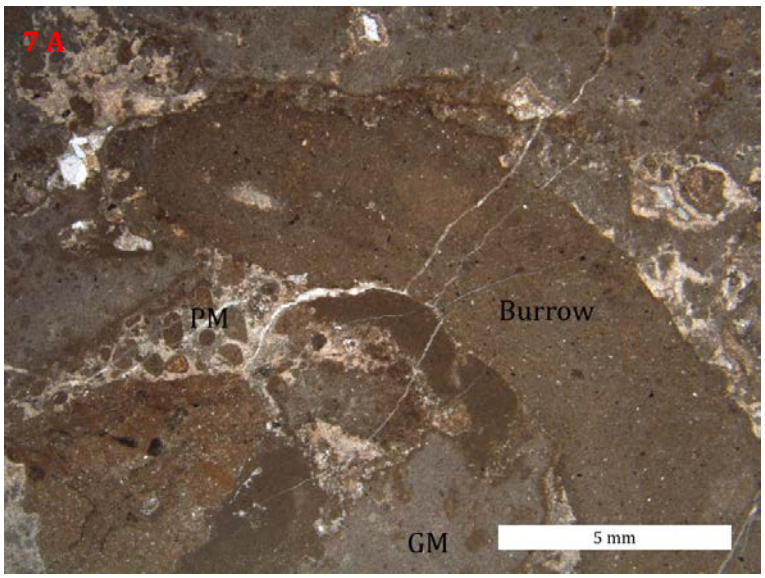

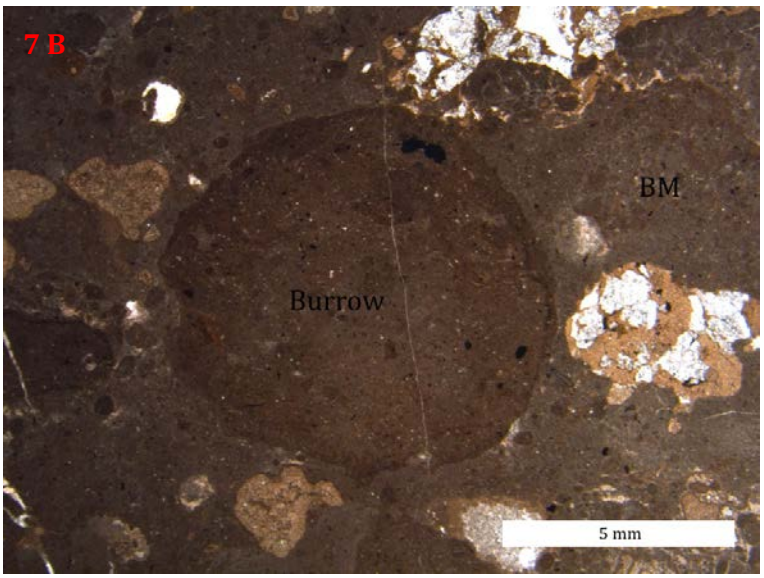

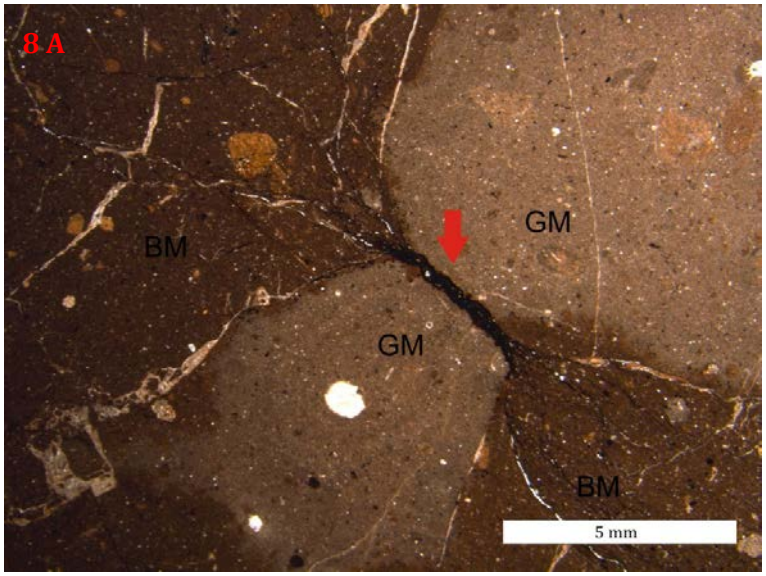

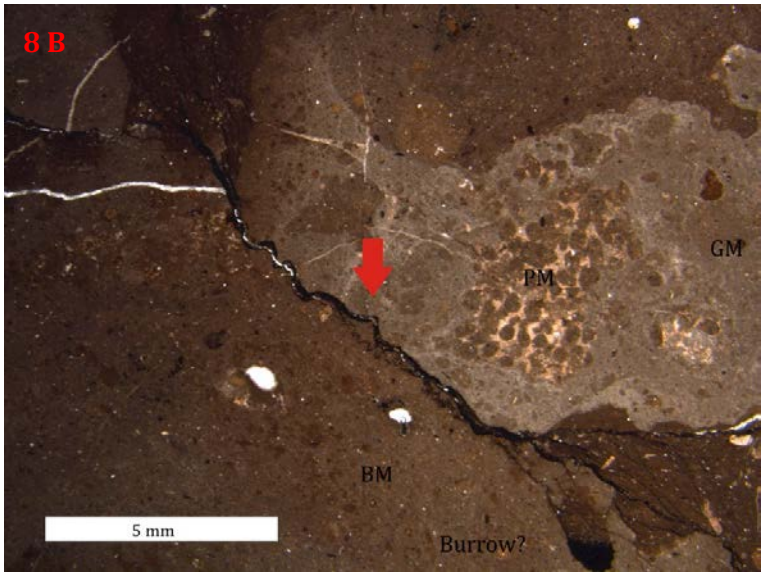

Figure 7 A: Tubular structure penetrating primary micrite phases gray (GM) and peloidal (PM) micrites. 7 B: Large, spherical structure within brown micrite (BM).

Figure 8 A & B: Gray and brown micrite showing pressure solution.

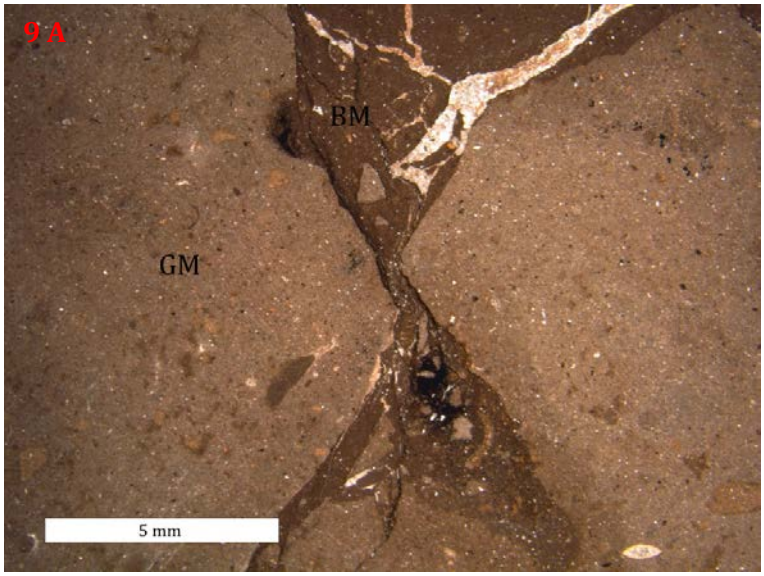

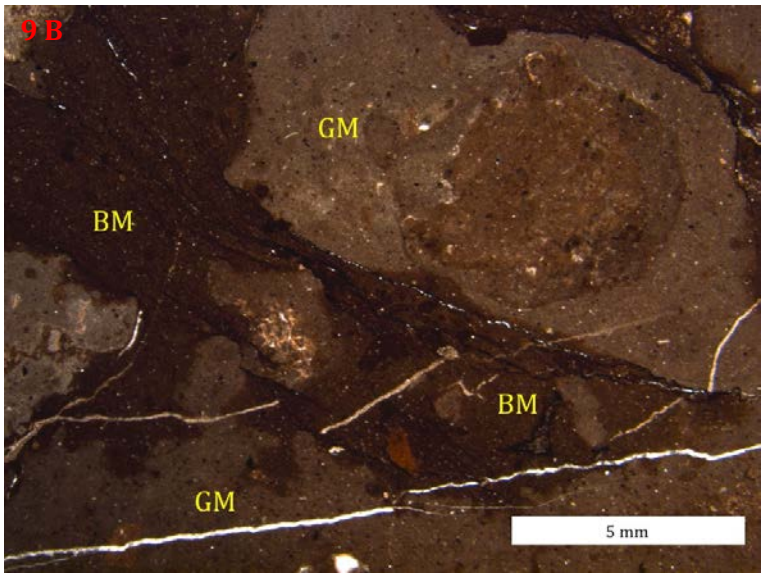

9 A & B: Consolidated gray micrite (GM) and more viscous brown micrite (BM).

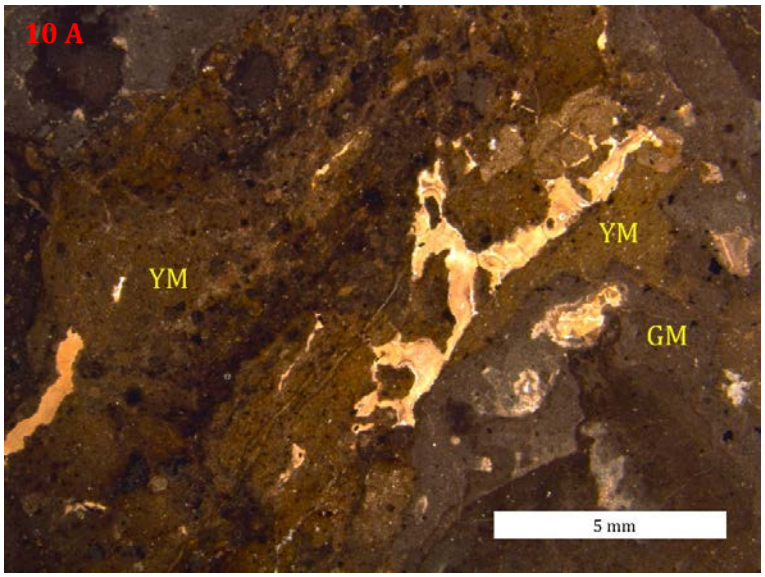

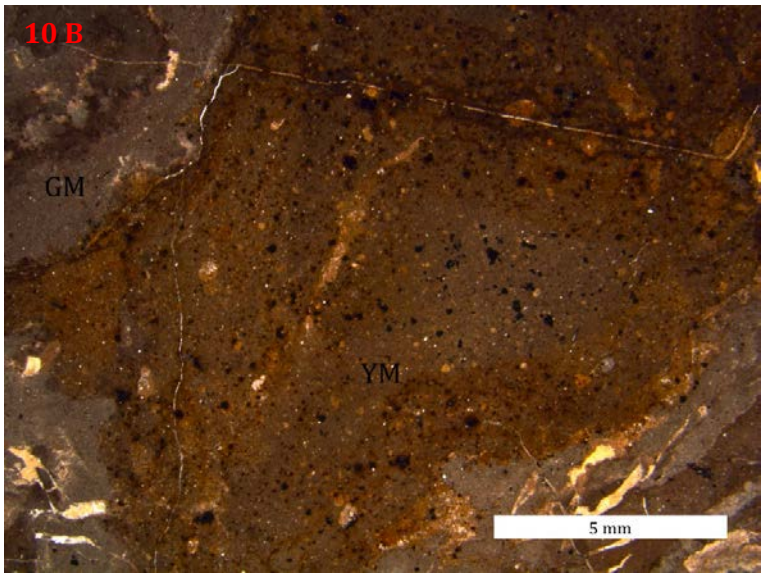

Figure 10 A & B: Yellow micrite (YM) containing abundant opaque pyrite grains and enclosed by the surrounding gray micrite (GM).

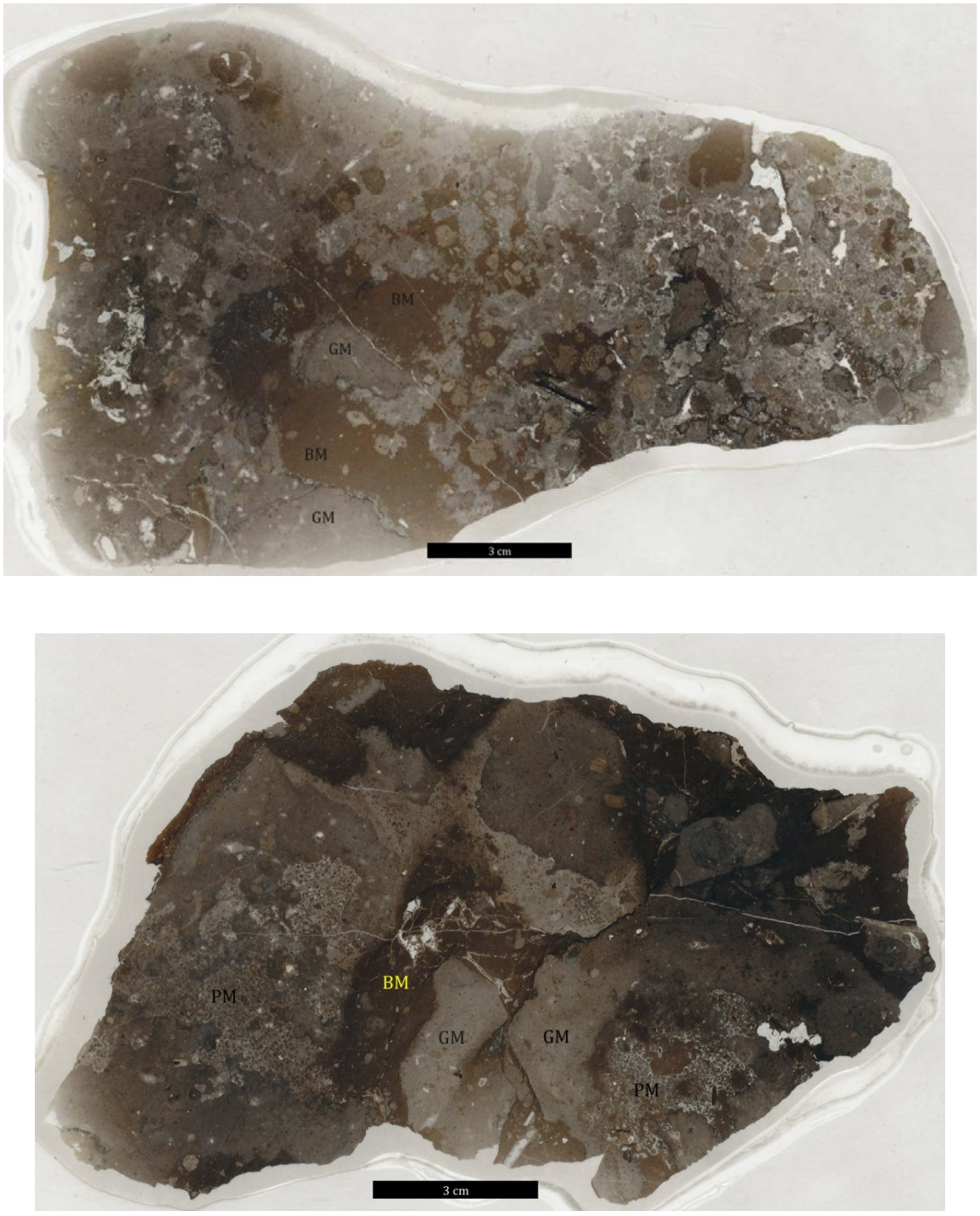

Figure 11: Two scans of Willapa Bay thin sections, 15 x 10 cm. Gray (GM) and brown (BM) micrite make up the bulk of the samples. Peloidal micrite (PM) is not as common as PM and BM.

Another, rare variety of micrite is yellowish micrite, typified by high amounts of pyrite (Fig. 10). The cavities of Willapa Bay samples are filled by numerous secondary phases. One of the earliest phases is a gray microcrystalline calcite, forming irregular seams around aggregates of gray and brown micrite. This variety is much less abundant than gray and brown micrite. It exhibits a cloudy, blurred fabric and typically lines the inner rims of cavities. This seam micrite is virtually free of detritus (Fig. 12).

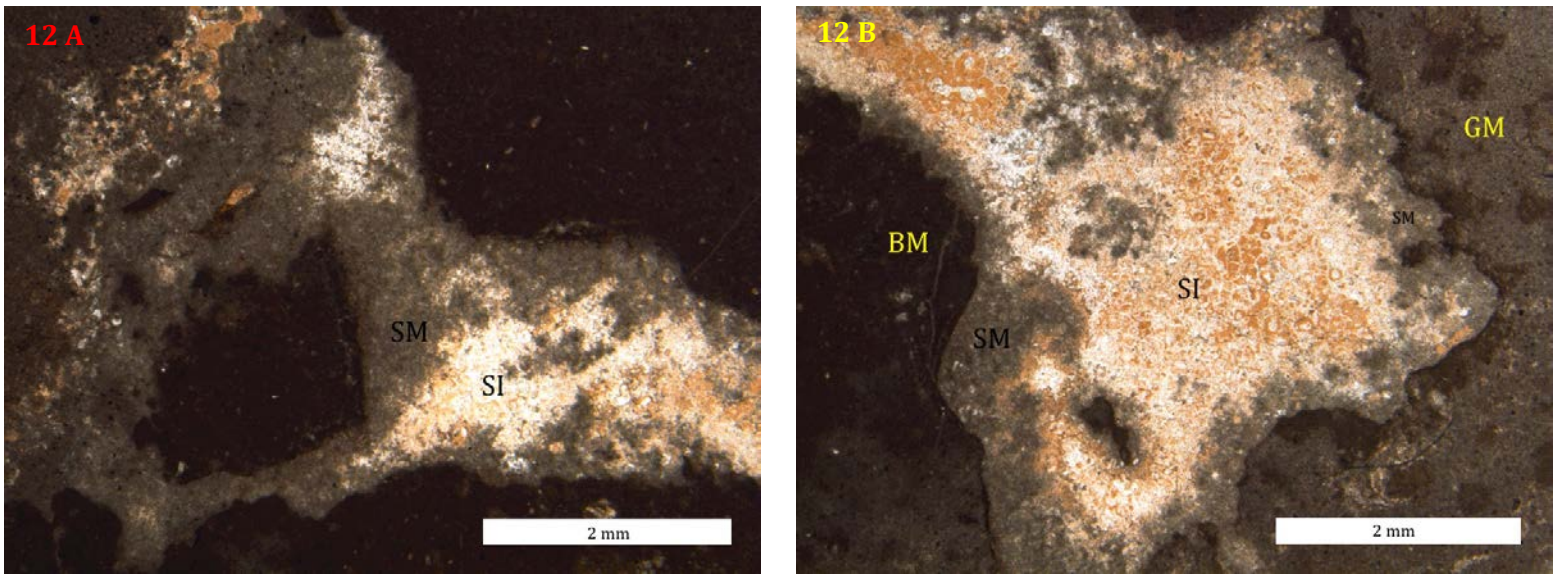

Figure 12 A: Seam micrite (SM) growth on the inside of cavities filled with silica (SI).
12 B: Cavities are surrounded by gray (GM) and brown (BM) micrite.

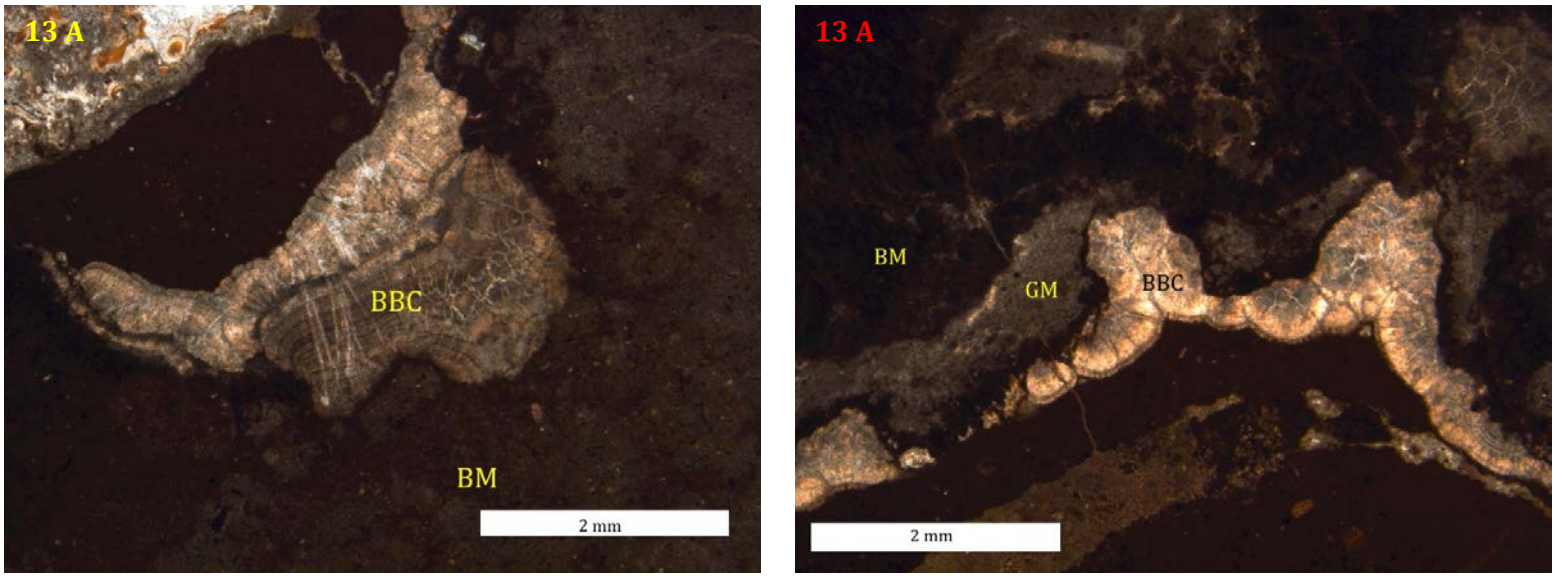

Figure 13 A & B: Banded botryoidal cement (BBC) growing on the inside of cavities surrounded by primary brown (BM) and gray (GM) micrites

Banded and botryoidal cement (BBC) is a further, but rare cavity-filling phase occurring in the Willapa Bay deposit. The botryoids consist of fibrous crystals and reveal a banded dark-light

zonation perpendicular to crystal growth (Fig. 13). If seam micrite and banded and botryoidal cement occur within same cavity, banded and botryoidal cement is mostly earlier than seam micrite. The phase that formed next in the paragenetic sequence is silica. However, it can also occur isolated with gray and brown micrites. Silica is mostly micro to cryptocrystalline and occasionally fan-shaped with a chalcedony- appearance, resembling the fabric of BBC (Fig. 14). Silica mostly very light gray to white, but also light brown to beige (Fig. 14 A).

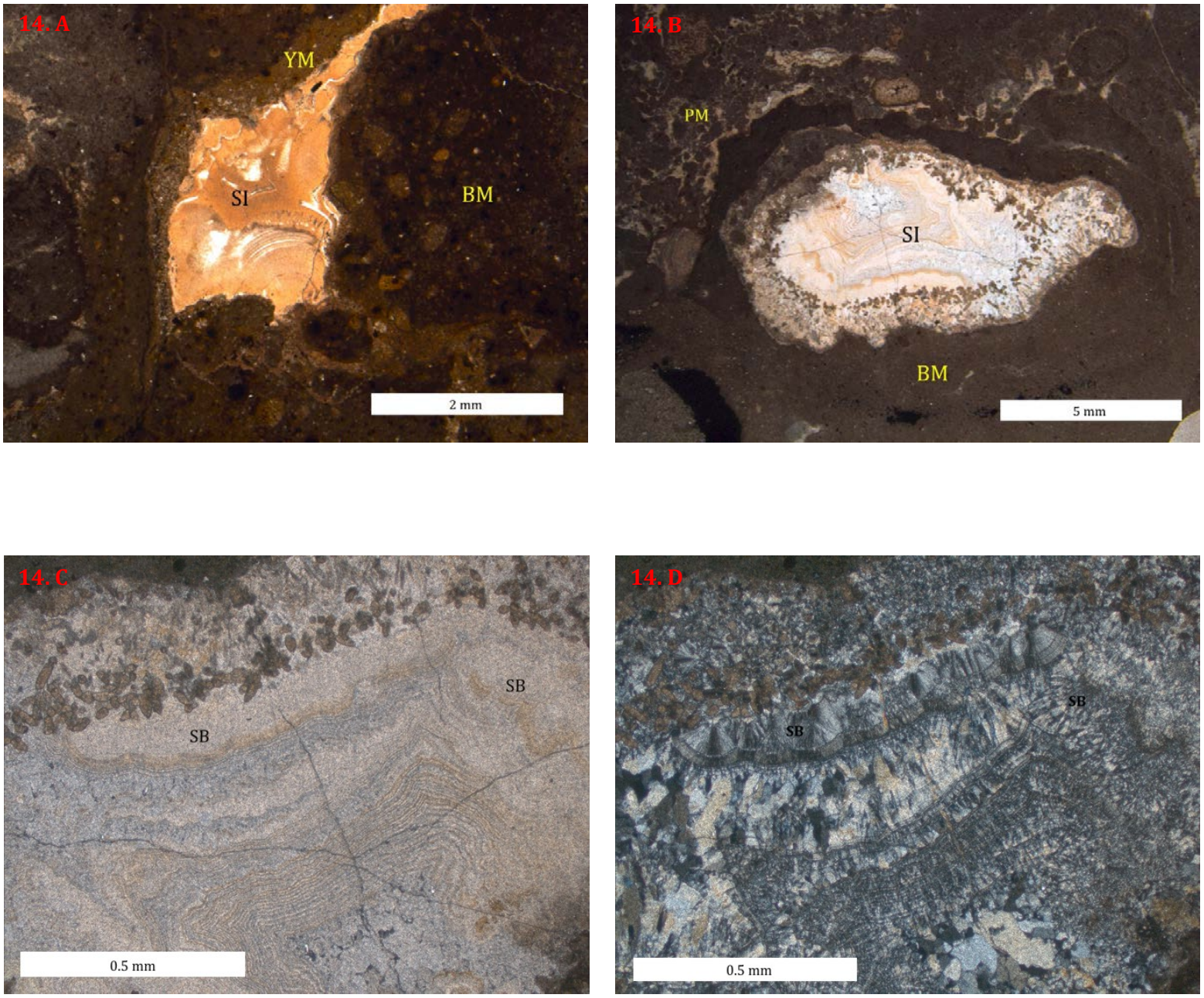

Figure 14: Various occurrences of silica (SI) in the Willapa Bay deposit. 11 A: Brownish silica within a cavity enclosed by yellowish micrite. 14 B: Silica within a larger cavity surrounded by brown micrite (BM). 14 C: Silica texture resembling botryoidal carbonate cement (SB) without and with (14 D) crossed – polarized light.

A further phase is late micrite. It can be distinguished from gray and brown micrites by its color and texture. It exhibits a different brown tone than brown micrite and contains much less detrital material (Fig. 15). It occurs within cavities and its position in the paragenetic sequence reveals that it formed after banded and botryoidal cement, seam micrite and silica.

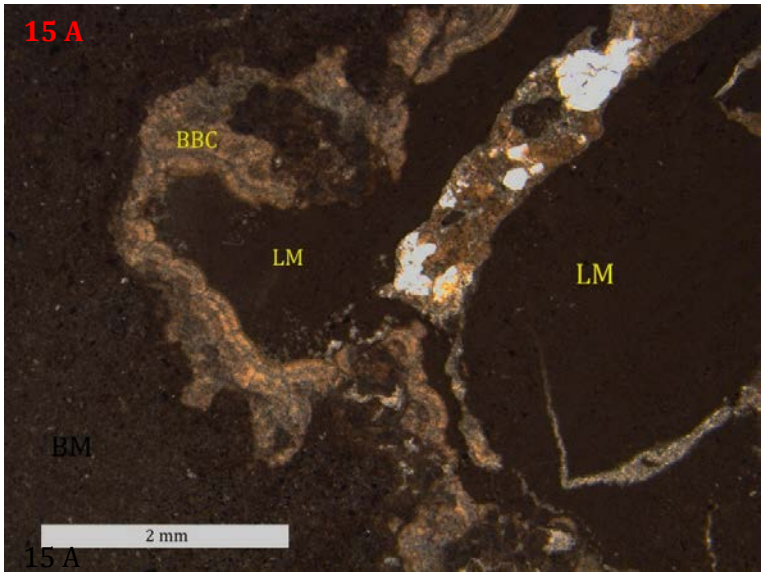

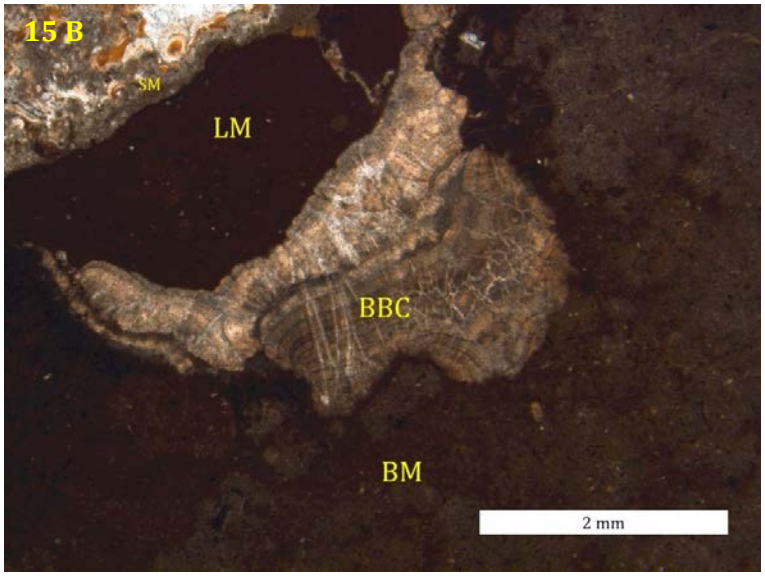

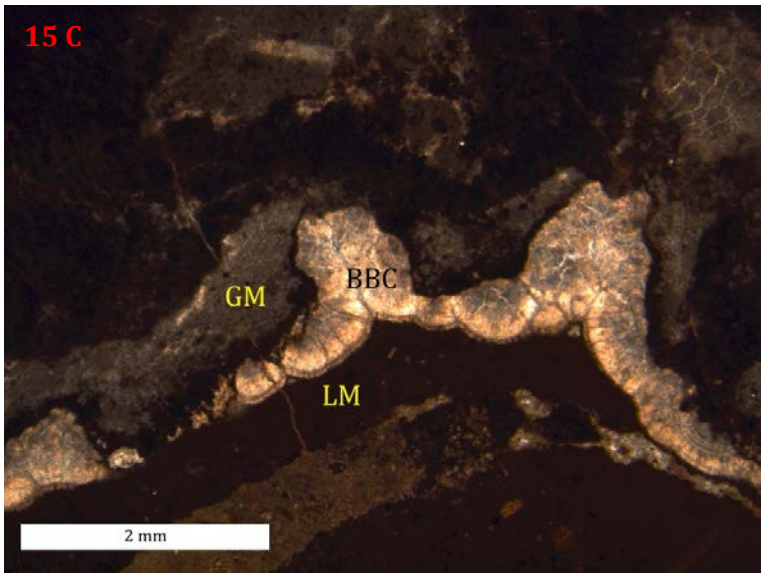

Figure 15 A & C: Brown micrite (BM), BBC and late micrite (LM).
15 B: Brown micrite (BM), BBC, late micrite and seam micrite (SM) in sequence.

The following paragenetic sequences were identified in individual samples: (i) Gray or brown micrite – BBC – late micrite (Fig. 15); (ii) gray or brown micrite – seam micrite – silica (Fig.12). The most common observation is that gray or brown micrite make up the bulk matrix of the rock and that most cavities are filled with silica (Figs 12 & 14). BBC and seam micrite follow brown or gray micrite as first pore – filling phase if they occur (Figs 12 & 15). Late micrite occurs within cavities mostly after banded and botryoidal cement (Fig. 15).

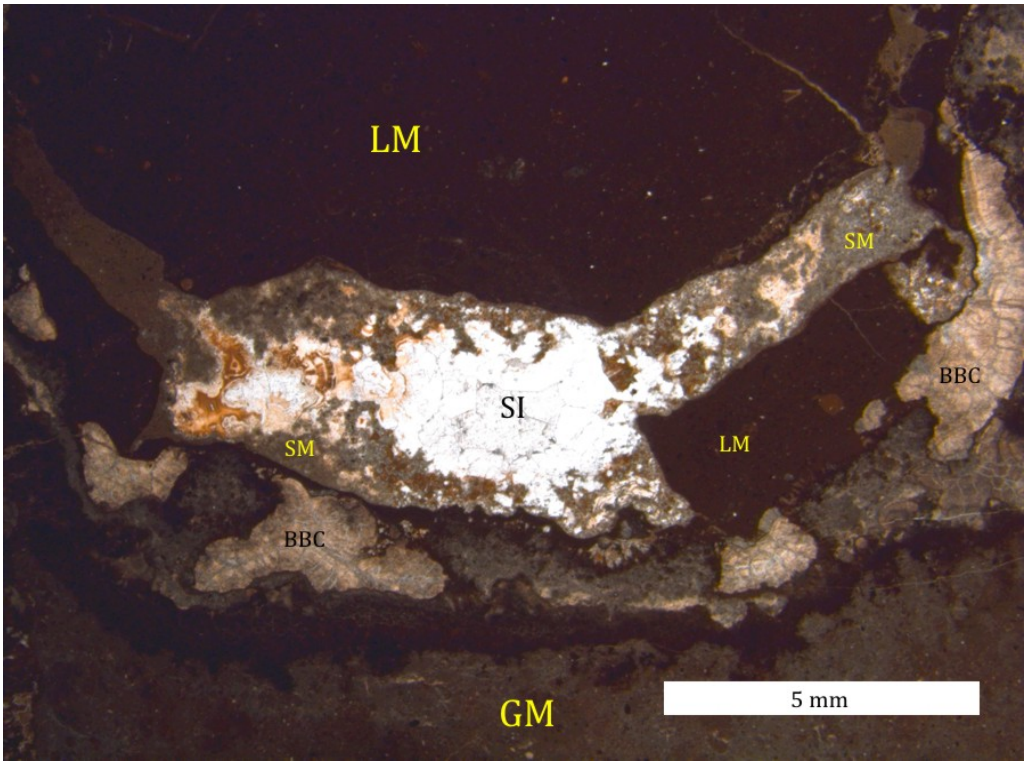

Figure 16: Paragenetic sequence in the Willapa Bay deposit: Gray micrite (GM), banded botryoidal cement (BBC), seam micrite (SM), silica (SI) and late micrite (LM).

4.2 – Sample description – Knappton

Rock samples from Knappton have a fundamentally different rock fabric than Willapa Bay samples. The rock is characterized by more and larger cavities, most of which have been filled by secondary precipitates. By far the most abundant cavity-filling phase is banded and botryoidal cement (BBC), which forms the framework of most Knappton limestone. Therefore, Knappton rocks can be classified as a cement framestone (Flügel, 2004).

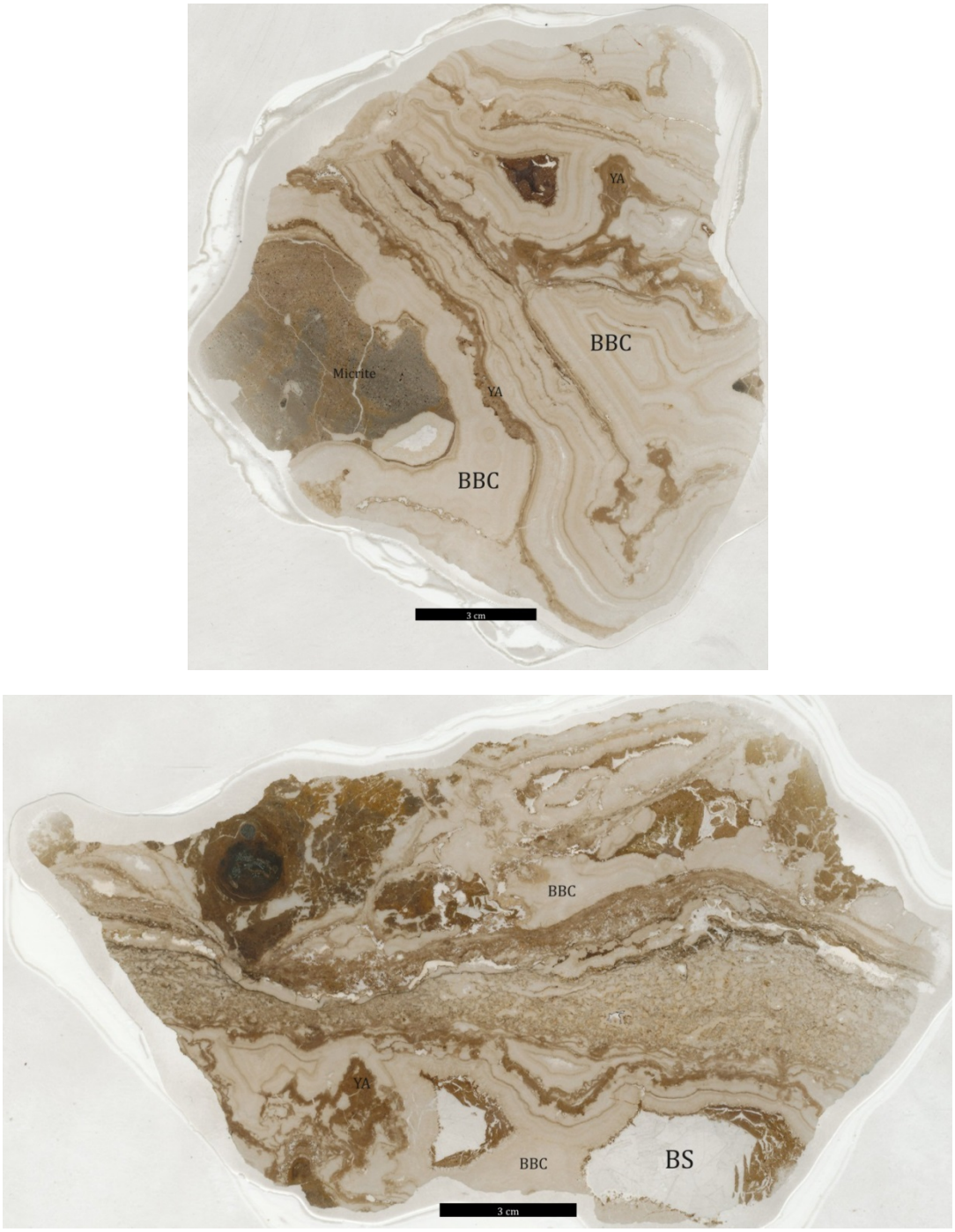

Figure 17: Thin section scans of Knappton rock samples. Banded botryoidal cement (BBC) comprises the major constituent of the bulk rock. Equant calcite (blocky) spar (BS) also fills larger cavities. Black scale bar equals 3 cm.

Main constituents of the Knappton seep deposit are different varieties of micrite (i.e., microcrystalline calcite) that formed at different stages in the paragenetic sequence. Authigenic, primary micrite exhibits abundant, small pyrite crystal aggregates and quartz grains. Some of the micrite reveals a clotted or peloidal fabric. Micrite is often cross cut by a multitude of veins of variable size, which are mostly filled by carbonate cement (Fig. 18).

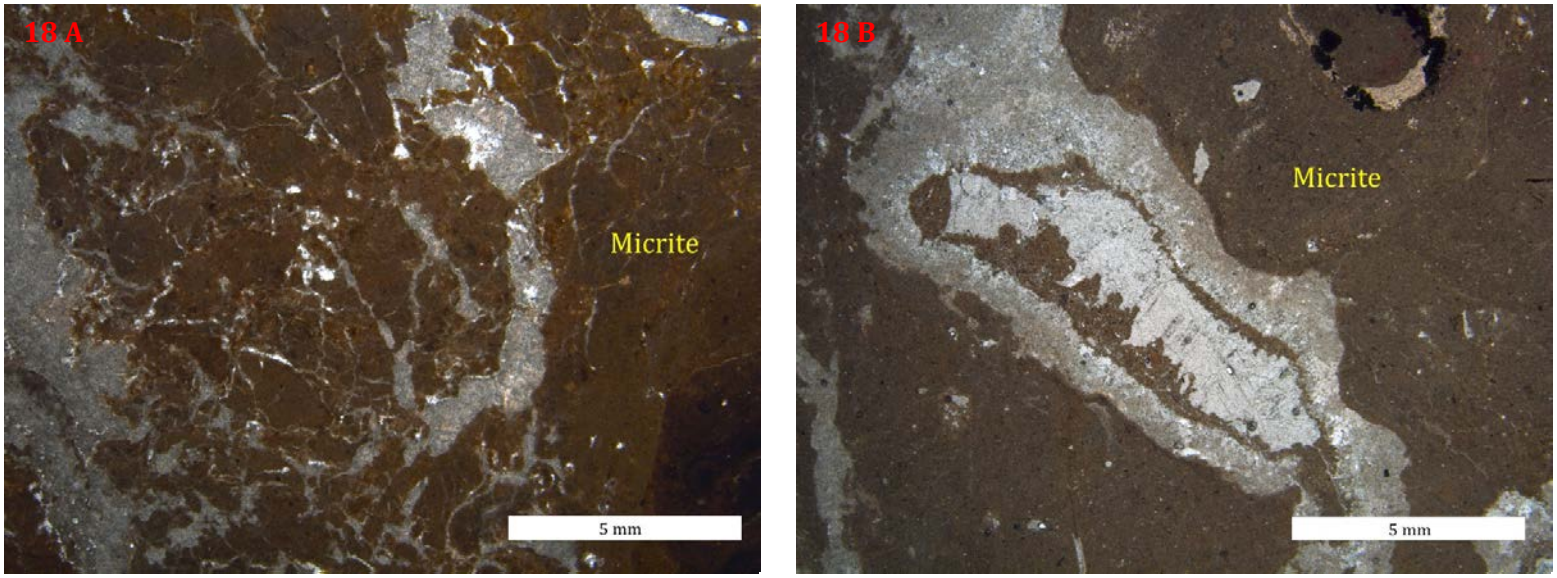

Figure 18: Micrite at Knappton showing different shades of brown. 18 A: Micrite penetrated by several veins filled by secondary phases

The most abundant phase at Knappton is banded and botryoidal cement (BBC). It is prominent in all samples and makes up most of the bulk volume of the rock. Banded and botryoidal cement is an aggregate of acicular crystals that form isopachous rims or botryoids (Fig. 19 A). Some of the aragonite botryoids are silicified (Fig. 21). The tips of these botryoids show a needle-like, flayed fabric and point towards the center of cavities (Fig. 19 B). There is a second, early diagenetic cement, which can be distinguished from BBC by its yellowish to light brown color (Fig. 19 D). Its reveals a patchy occurrence within the BBC and exhibits mostly crypto- to microcrystalline crystal habit. Commonly irregular bands of this phase referred to as yellow aragonite are intercalated within the banded variety of the banded and botryoidal cement (Fig. 19 C). The darker color of the yellow aragonite compared to BBC is possibly caused by fluid inclusions or other impurities.

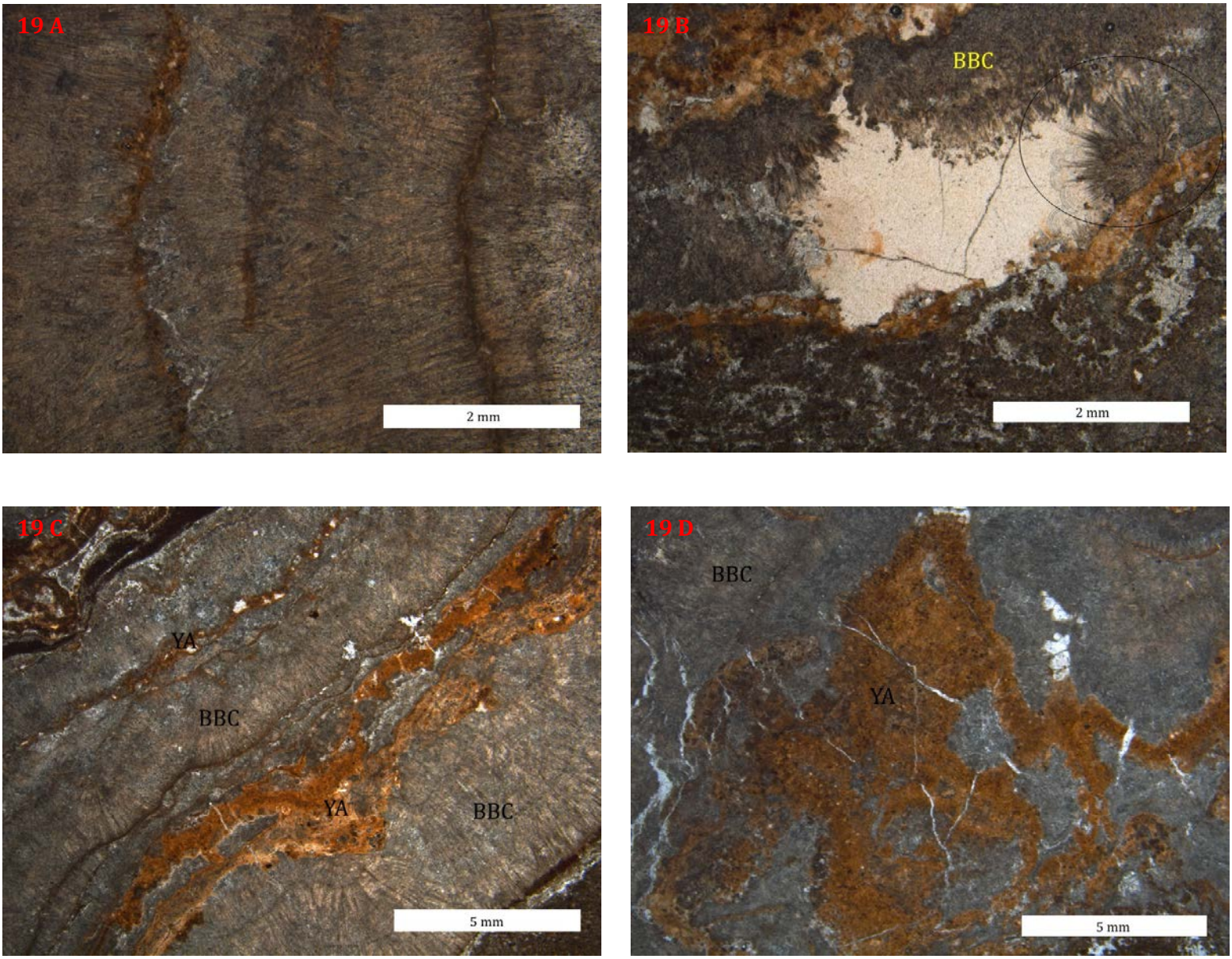

Figure 19 A: Banded and botryoidal cement (BBC) with crystals forming small fans. 19 B: BBC crystals pointing towards the centre of a cavity (denoted by the black circle). 19 C: Intercalated bands of BBC and yellow aragonite (YA).

19 D: Patchy distribution of yellow aragonite (YA) within banded and botryoidal cement.

In places the yellow aragonite displays a botryoidal texture made of fibrous crystals in addition to a cryptocrystalline texture (Fig. 20). These yellow to gray botryoids with growth zonation are similar to those described from Willapa Bay. Where both varieties of yellow aragonite are developed, the crypto- to microcrystalline variety evolves into a fibrous, botryoidal aragonite.

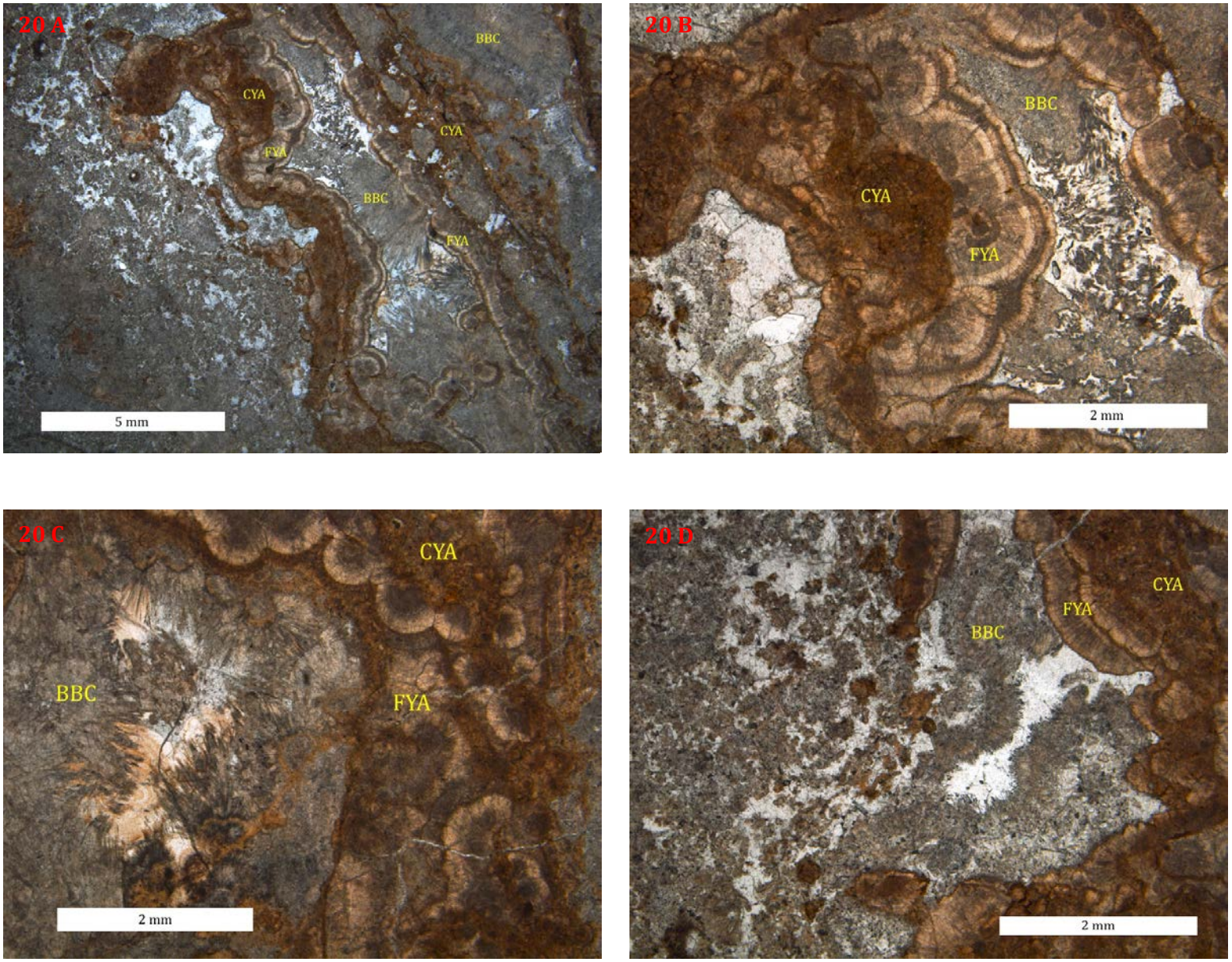

Figure 20 A - D: Cryptocrystalline yellow aragonite (CYA) evolving into fibrous (botryoidal) yellow aragonite (FYA). BBC occurs between and after yellow aragonite.

In most places cryptocrystalline yellow aragonite occurs alongside the banded and botryoidal cement. However, compared to banded and botryoidal cement and cryptocrystalline yellow aragonite, fibrous yellow aragonite seems to be rare, having been observed only in one sample.

Silica is the next phase in the paragenetic sequence. It is often found in association with banded and botryoidal cement, filling the remaining cavity space. Its texture is crypto- to microcrystalline or occasionally fibrous forming crystal fans (Fig. 21 D). These fans show rolling extinction under crossed-polarized light. Although present in every sample analyzed, silica represents only a small fraction of the rock volume, corresponding to approximately 5%. Under transmitted. light, the silica phases are predominantly whitish (Fig. 21 C) and occasionally light brown (Fig. 21 A).

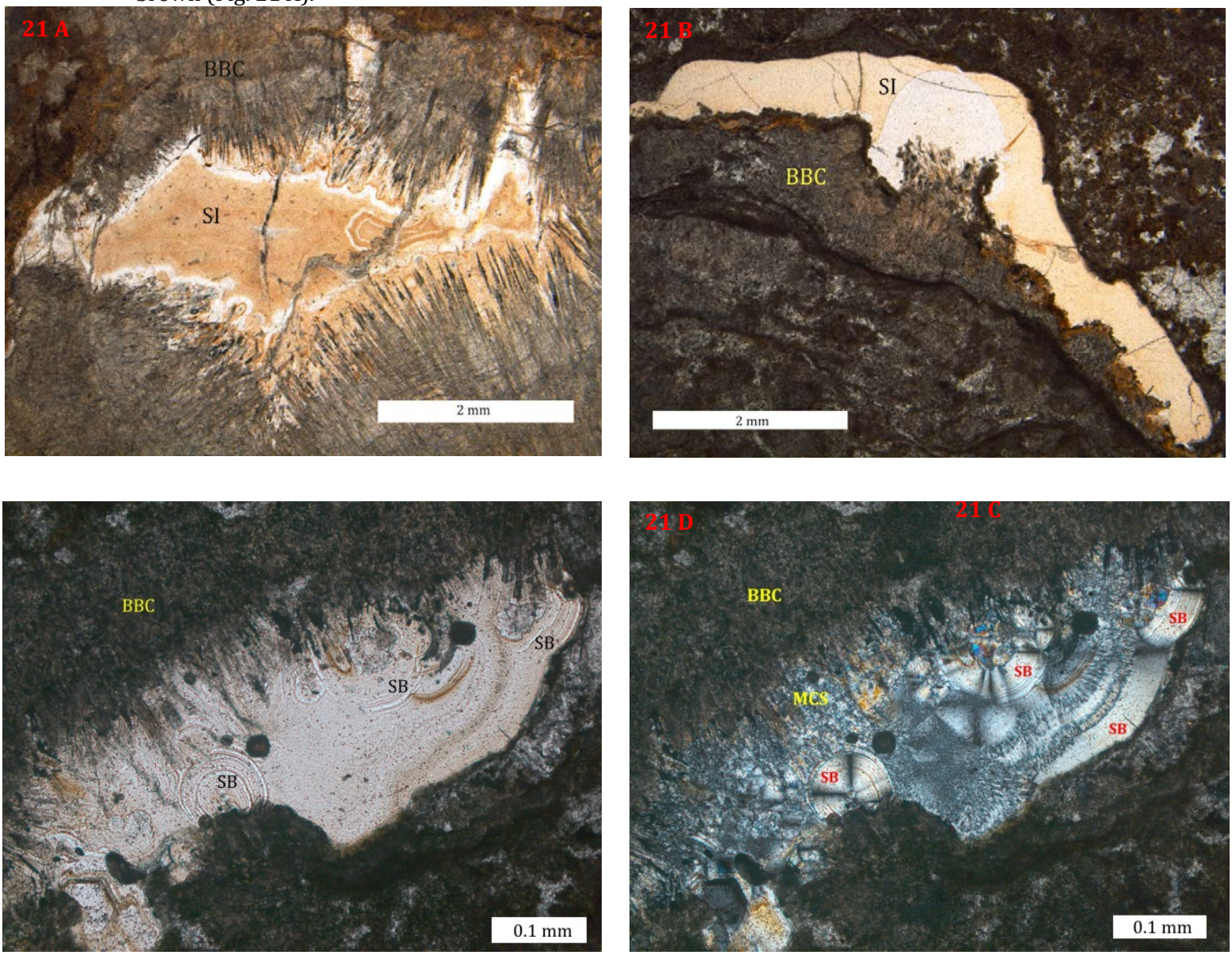

Figure 21 A: Brownish silica (SI) filling a larger cavity surrounded by banded and botryoidal cement (BBC). 21 B: Brownish silica (SI) within a pore adjacent to BBC. 21 C: Silica displaying botryoidal texture (SB) within a smaller cavity. 21 D: Same photograph as 21 C under crossed – polarized light. Botryoidal silica texture (SB) alongside microcrystalline silica surrounded by banded botryoidal cement (BBC).

Apart from banded and botryoidal cement and silica, a microcrystalline calcite phase occurs within cavities. This micrite corresponds to the late micrite described for the Willapa Bay deposit. With respect to the Knappton deposit, this phase is a microspar (Fig. 22).

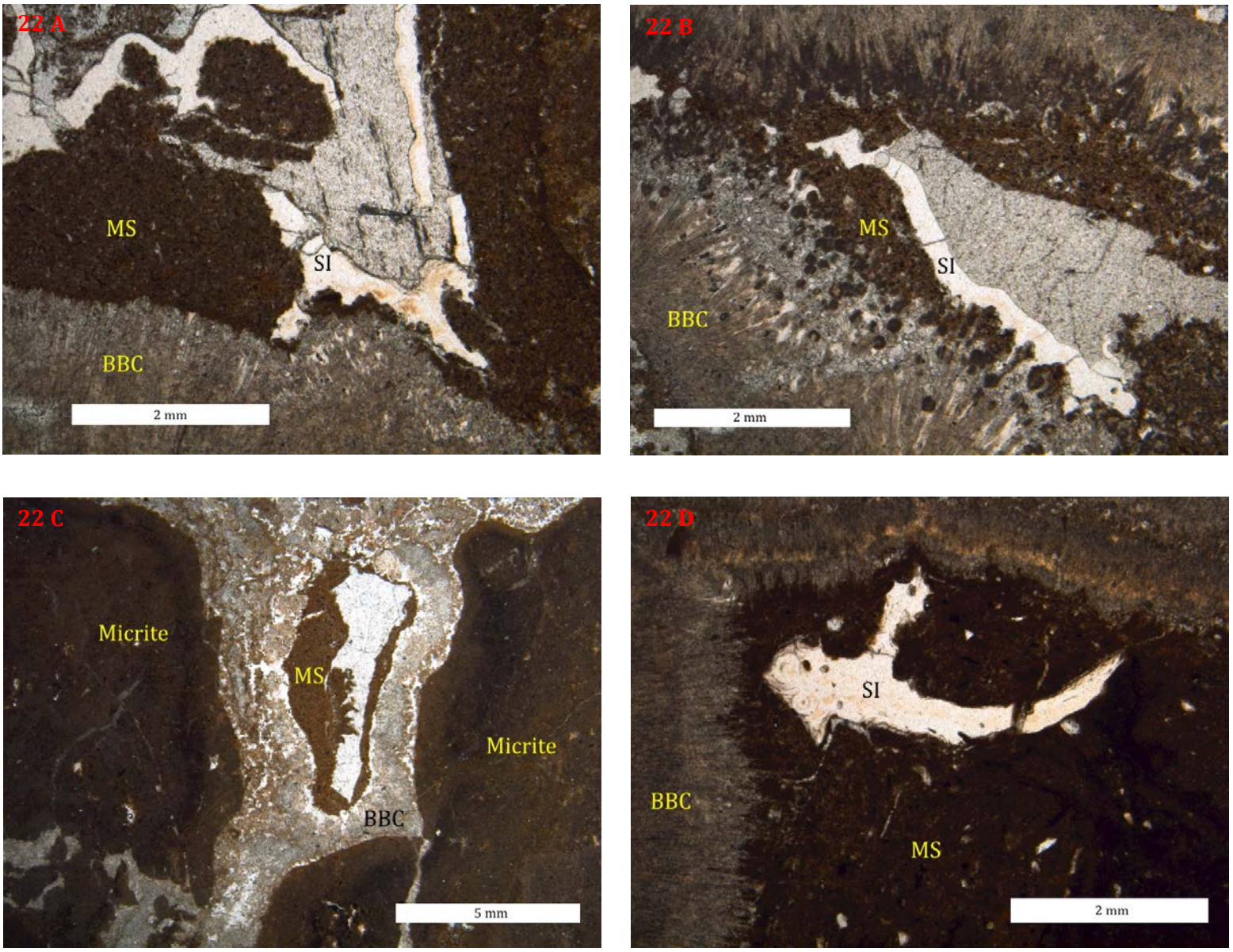

Figure 22 A, B & D: Microspar adjacent to banded and botryoidal cement (BBC) and silica (SI) 22 C: Primary micrite enclosing a cavity filled with BBC and microspar.

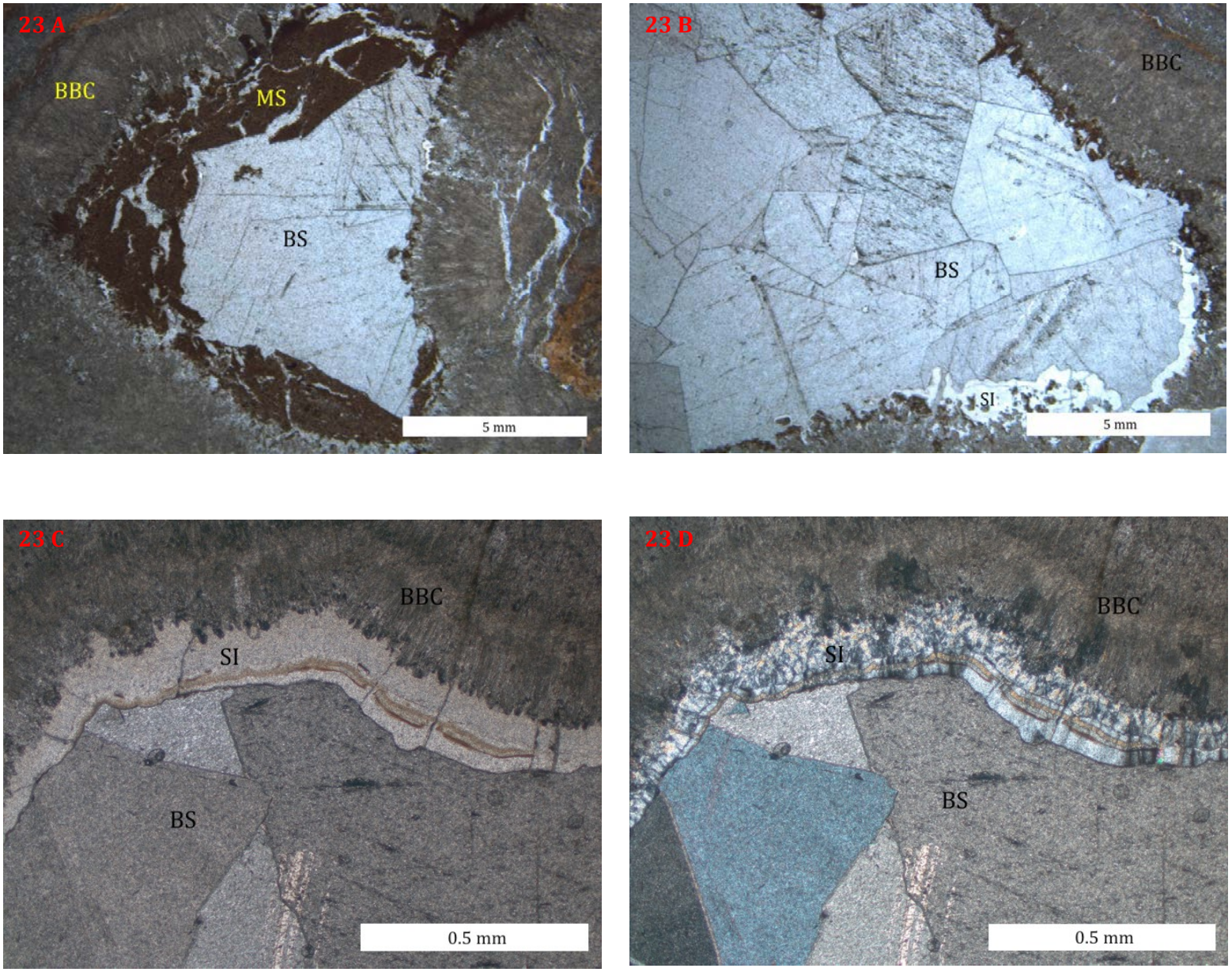

Figure 23 A: Equant calcite spar within the middle of a cavity adjacent to microspar (MS) and banded and botryoidal cement (BBC); plane porized light 23 B: A large cavity filled by equant calcite spar (BS) in contact with silica (SI) and BBC; cross polarized light.

The light to dark brown microspar crystals are larger than those of the matrix micrite (Fig. 22 D and 22 C). The youngest phase is equant calcite spar. It is a minor phase with regard to the bulk composition, but dominant in some cavities (Fig. 23). Different cleavage domains within individual crystals are apparent under crossed polarized light (Fig. 23 D).Most phases at Knappton show very little autofluorescence when exited with UV light. The only exception is the late microspar, revealing much stronger fluorescence compared to all other phases (Figs. 25 B & D).

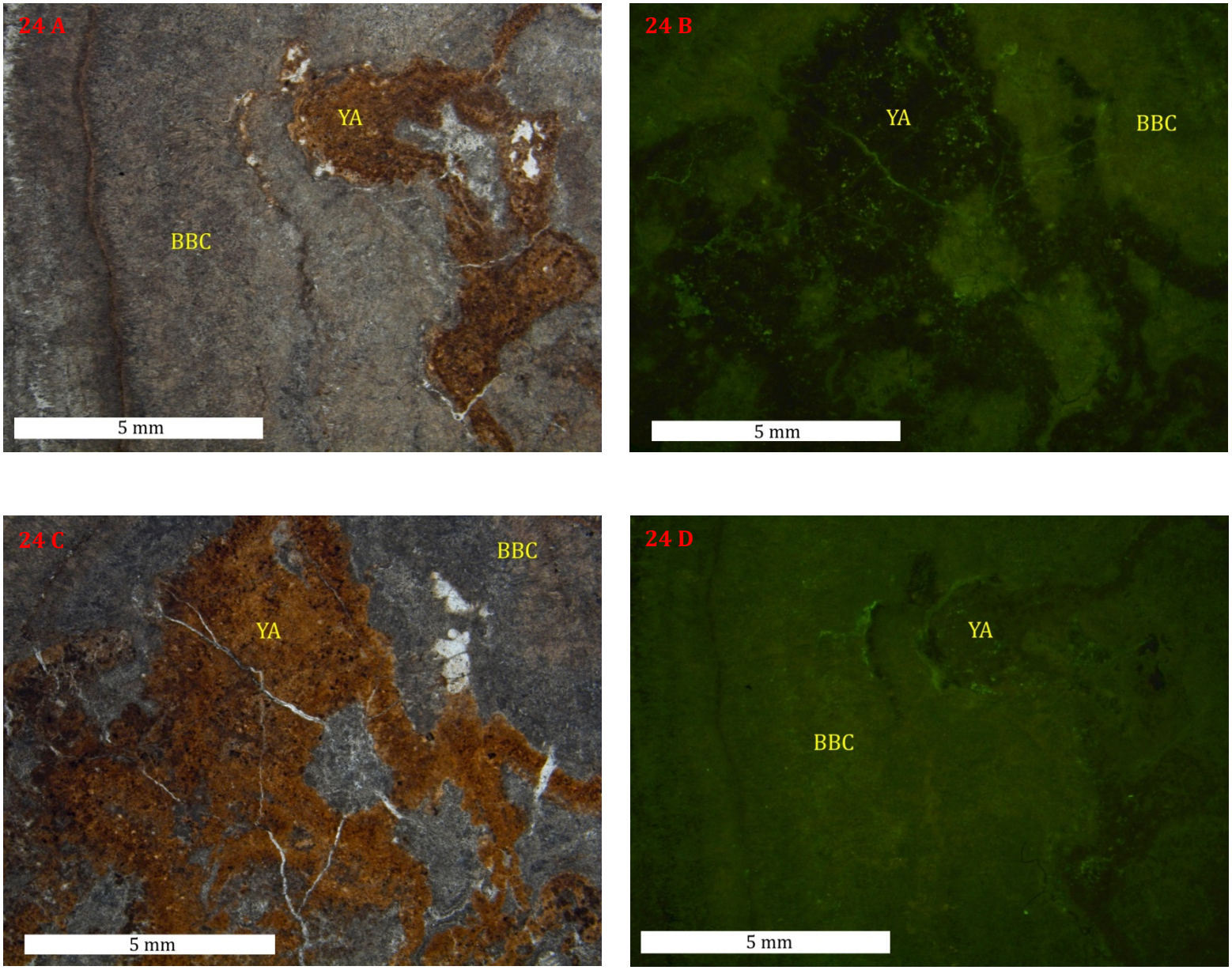

Figure 24: BBC and yellow aragonite (YA) under transmitted (left) and fluorescent (right) light.

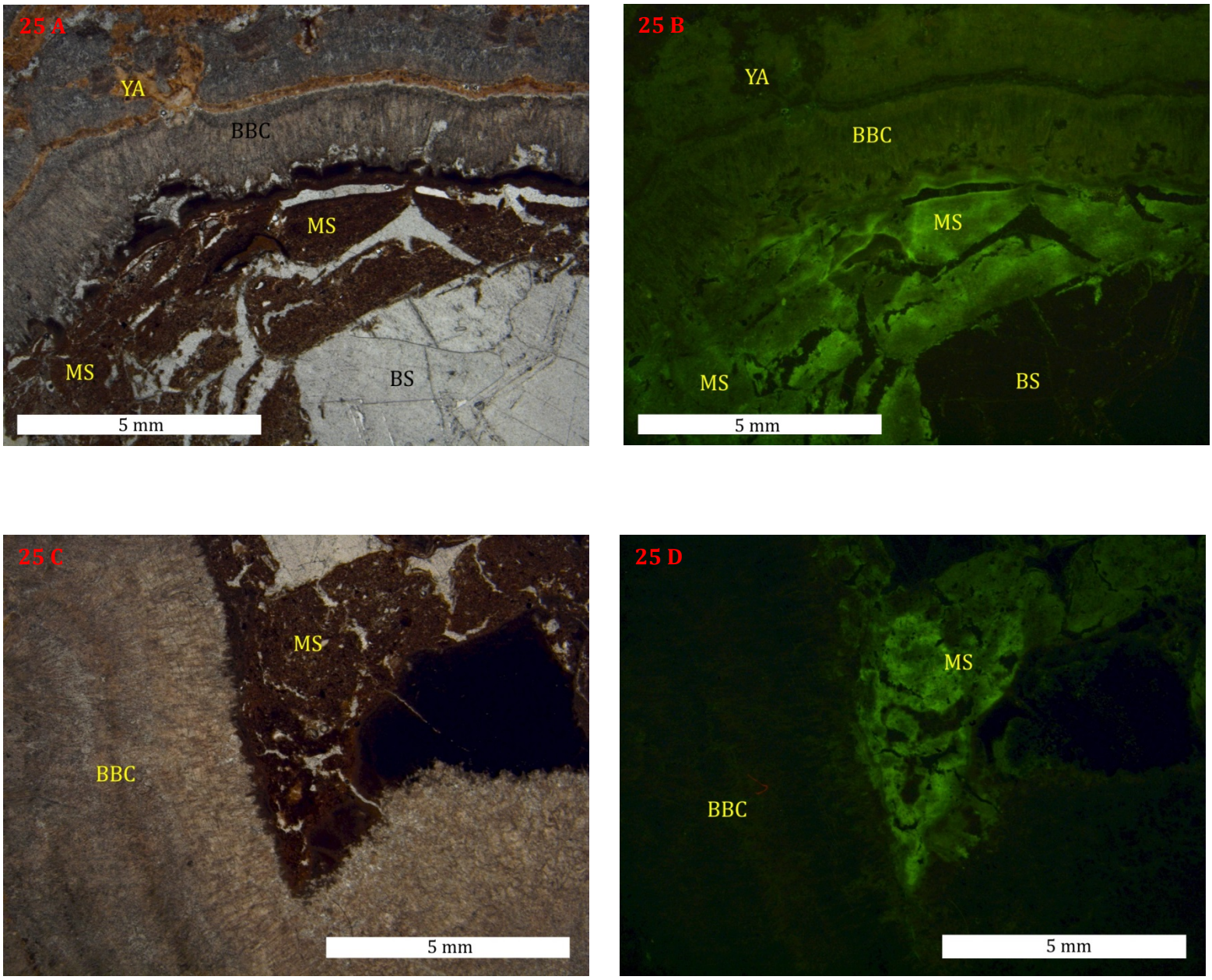

Figure 25: Yellow aragonite (YA), BBC, microspar (MS) and equant blocky calcite spar (BS) under transmitted (left) and fluorescent (right) light.

The matrix micrite is the first phase at Knappton followed by either clear (BBC) or yellow aragonite. This is the most common and recurring sequence in all samples. After the aragonite cements, silica and finally equant calcite (blocky) spar formed. However, this general sequence varies locally, suggesting a recurrent mode of mineral formation. Where microspar occurs, it tends to be present between BBC and silica of between banded and botryoidal cement and equant calcite.

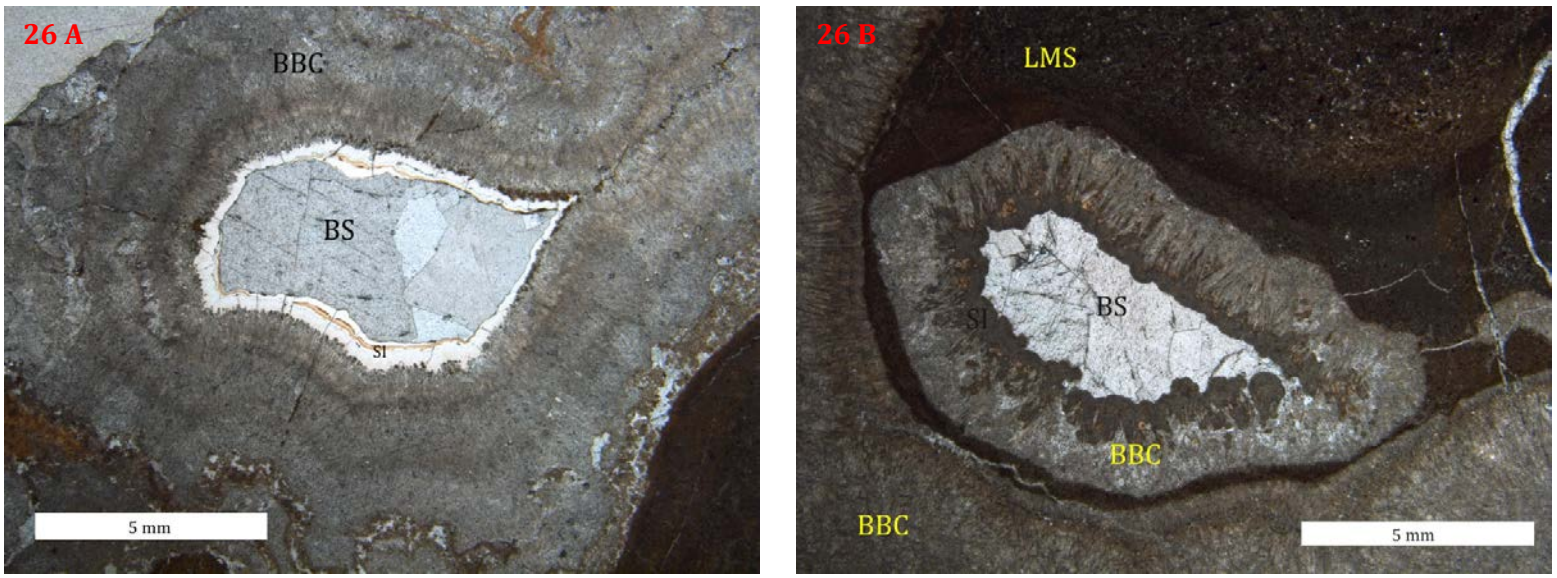

Figure 26 A: Phase sequence at Knappton: BBC – silica (SI) – equant blocky calcite spar. 26 B: Alternative sequence BBC – microspar (LMS) – BBC – silica (SI) – equant blocky calcite spar (BS).

4.3 – Isotope geochemistry

The seep limestones from Knappton and Willapa Bay were analyzed for stable carbon and oxygen isotope compositions of individual carbonate phases. 15 samples from Willapa Bay and 17 from Knappton were analyzed.

4.3.3. – Willapa Bay

The $\delta^{13}C$ values of the dark brown micrite fall between −11.9 and −0.8‰, $\delta^{18}O$ values fall between −13.9 and −13.6‰. Gray micrite revealed $\delta^{13}C$ values from −12.8 to −10.6‰ and $\delta^{18}O$ between −14.2 and −11.4‰. The isotopic composition of late micrite was found to be variable, showing $\delta^{13}C$ values between −5.9 and 1.1‰ as well as $\delta^{18}O$ values between −14 to −12.4‰. The yellowish micrite revealed $\delta^{13}C$ values between −4.0 and −3.9‰ and two $\delta^{18}O$ values of −13.9‰.

4.3.4. – Knappton

Micrite revealed $\delta^{13}C$ values between −7.8 and −7.3‰ and $\delta^{18}O$ values between −10.2 and −8.9‰. The $\delta^{13}C$ values of yellow aragonite range from −26.6 to −23.2‰, $\delta^{18}O$ values from −6.9 to −6.6‰. Banded and botryoidal cement yielded $\delta^{13}C$ values ranging from −27.6 to −12.3‰ and $\delta^{18}O$ values from −12.4 to −9.3‰. The $\delta^{13}C$ values of equant calcite fall between 4.4 and 7.1‰, $\delta^{18}O$ values fall between −11.7 to −11.1‰.

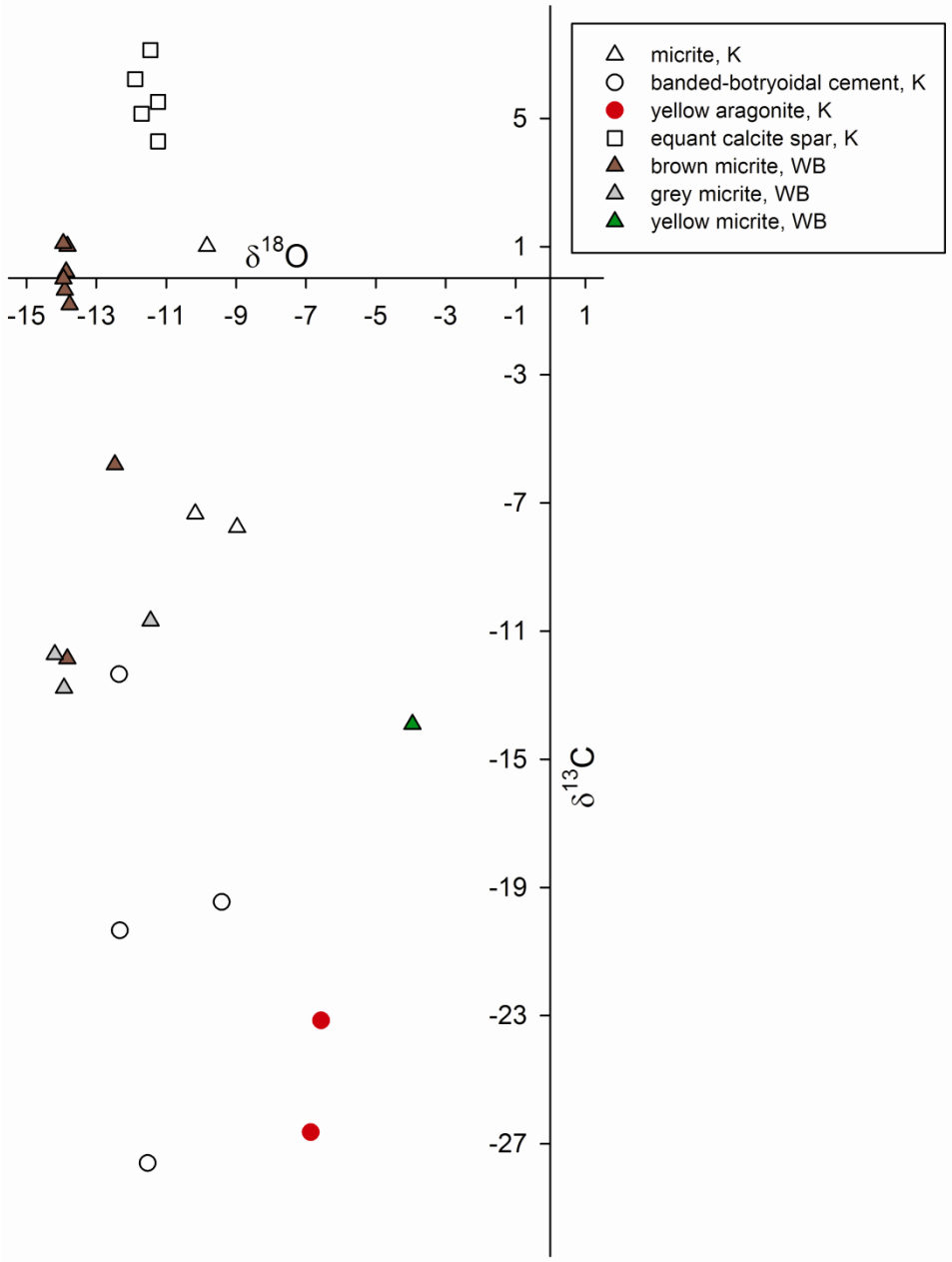

Figure 27: Isotope cross-plot showing all sampled phases.

5 – Discussion

5.1 – Implications from petrography

Carbonates

Microcrystalline calcite is one of the most common phases found in seep limestones, although microcrystalline aragonite and dolomite may occur as well (Roberts and Aharon, 1994; Peckmann et al., 2001). Volumetrically, micrite dominates the limestones from Willapa Bay, accounting for more than 90% of the rock volume (Fig. 11). At Knappton, micrite is less abundant, accounting for 15 to 25%. A large number of biogeochemical processes can lead to localized changes in porewater chemistry, affecting carbonate speciation and favoring carbonate precipitation or its dissolution (Riding and Liang, 2005). The process responsible for changing the chemical environment and triggering precipitation of micrite at Willapa Bay and Knappton is the sulfate-dependent anaerobic oxidation of methane. This reaction (1) produces bicarbonate ions, which subsequently react with porewater calcium leading to calcium carbonate precipitation. Peloidal micrite is especially abundant in the Willapa Bay deposit (Figs. 6 & 11). Peloidal textures result from fecal pellets attributed to seep invertebrates (e.g. Kauffman et al., 1996; Peckmann et al., 2002), which are a sign of intense biological activity at the seep site (Beauchamp and Savard, 1992). Fecal pellets are produced by burrowing organisms thriving on organic particulates (Flügel, 1982, 2004) by ingesting carbonate mud, digesting the required components and subsequently excreting non-digested carbonate mud as well rounded pellets (Tucker and Wright, 1990). Some of the pellets in the Willapa Bay deposit reveal small, crescent-shaped canals aligned in symmetrical groups (Fig. 6 D). Such trace fossils have been described as microcoprolites produced by invertebrates such as decapod crustaceans, which are predators or scavengers at seeps (e.g. Peckmann et al., 2007). Peloidal micrite textures and individual fecal pellets point towards extensive micro- and macrofaunal activity within the Willapa Bay deposit, whereas both features are virtually absent in the Knappton deposit. Furthermore, the tube-shaped burrowing structures representing bioturbation (Fig. 7) are additional indicators of macrofaunal activity. It seems plausible that gray and brown micrite precipitation was linked to repeated stages of on-going and ceasing AOM and increasing burial, allowing earlier phases to consolidate and later phases to be washed in. This is reflected by figures 8 and 9, showing consolidated gray, and more viscous brown micrite.

In situ brecciation, indicated by intense fracturing of the bulk rock (Fig. 28) is a common feature of seep limestones (e.g. Beauchamp and Savard, 1992; Peckmann et al., 2003). Brecciation and fracturing has been attributed to gas hydrate dissociation, producing short-term disruptions at shallow seafloor seeps (MacDonald et al., 2003), causing sediment deformation in methane rich environments (Peckmann and Thiel, 2004). Sediment injections (Figs. 8 & 9) describe the forcing of sedimentary material under pressure into a preexisting deposit (Neuendorf et al., 2005). These features require (i) liquefaction for mud mobilization and (ii) failure of the host rock, producing cracks and fissures (Peckmann et al., 2011; Figs. 18 A, 28). Rock failure was most likely produced by *in situ* brecciation as described above. Weakly lithified lime mud (brown micrite) was subsequently injected into more consolidated, gray micrite (Fig. 8). Intense fracturing by gas pressure may have also lead to the observed pressure solution structures (Figs. 8 & 9). The red arrows in figures 8 A & B indicate styloliths, produced by movement and squeezing of more consolidated carbonate blocks and are late diagenetic processes.

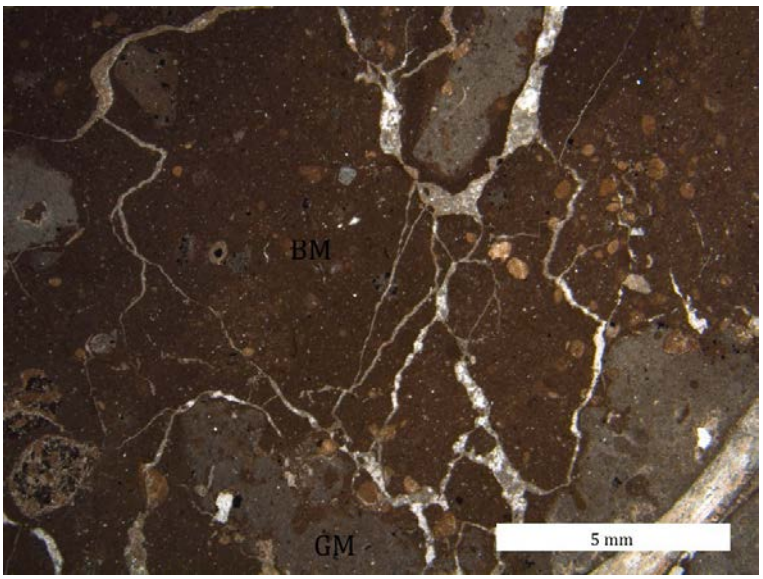

Figure 28: In situ brecciation causing cracks and fissures within brown (BM) and gray (GM) micrite in the Willapa Bay deposit

Seam-micrite mostly occurs as a growth rim on the inside of cavities postdating the micrite matrix and predating silica formation (Figs. 12 & 16). Peckmann et al. (2003) reported similar micrite phases from Washington State. It only occurs at Willapa Bay; its purity and fabric is indicative of *in situ* precipitation (cf. Peckmann et al., 2003). Carbonate cements are a common feature of seep limestones (e.g. Beauchamp and Savard, 1992; Savard et al., 1996; Peckmann et al., 2002, 2003; Himmler et al., 2008; Kuechler et al., 2012). The botryoidal fabric has been interpreted to represent recrystallization of aragonite cement derived from AOM (Beauchamp and Savard, 1992). Calcite and aragonite are the two most common minerals in marine carbonate environments (Burton, 1993). In modern seawater several factors influence the stability of aragonite versus calcite, the most prominent being the Mg/Ca ratio of the solution (Morse et al., 1997; Davis et al., 2000), temperature (Wilkinson et al., 1984; Mackenzie and Morse, 1992), sulfate concentrations (Bots et al., 2011) and CO_2 partial pressure (Burton and Walter, 1991; Burton, 1993). Precipitation of aragonite rather than calcite in seawater is common due to the inhibiting effect of hydrated Mg^{2+} ions on the calcite structure (Bathurst, 1975). However, the role of calcium and magnesium on carbonate precipitation is difficult to assess without porewater data from seep locations, but it can be assumed that at least in shallow

sediments near the sediment-water interface, seawater Mg^{2+}/Ca^{2+} ratios favor aragonite over calcite precipitation (Ritger et al., 1987; Peckmann et al., 2001).

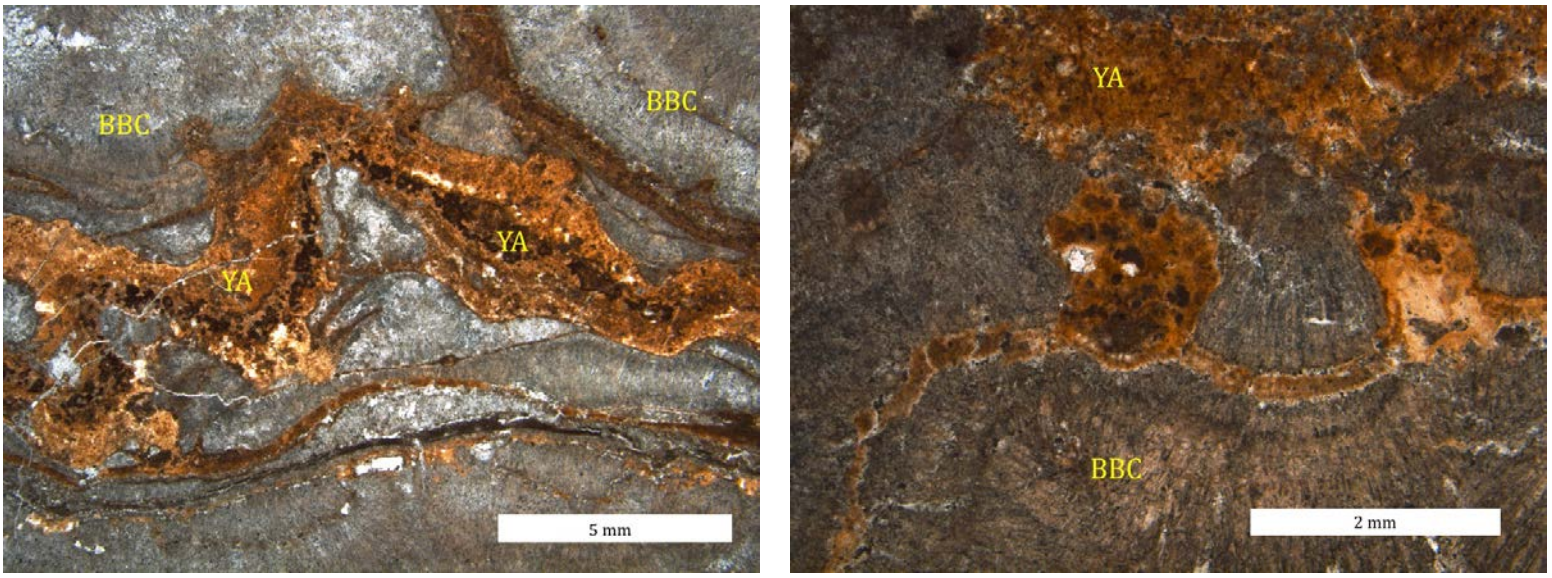

Figure 29: Yellow aragonite (YA) occurrence at Knappton.

The banded and botryoidal cement is dominant phase of the Knappton deposit, where it comprises 50 to 75% of the total rock volume (Figs 17 & 19). In the Willapa Bay deposit, this banded and botryoidal cement is totally absent. However, Willapa Bay shows a somewhat different variety of botryoidal cement texture as shown in figures 10, 12 and 13. Its darker color is attributed to the presence of organic matter trapped in fluid inclusions. The fact that these botryoidal cements are not as extensive as at Knappton points to less vigorous methane seepage than at Knappton (c.f. Peckmann et al., 2009). Yellowish calcites and aragonites have been reported from several cold-seep sites (e.g. Beauchamp and Savard, 1992; Campbell et al., 2002; Peckmann et al., 2002, 2003; Himmler et al., 2008; Kuechler et al., 2012). The yellowish color may result from significant amounts of organic matter inherent within this phase. However, it does not show an intense fluorescence as would be expected. It is noteworthy that this phase occurs in all Knappton samples, but is completely absent at Willapa Bay. Furthermore, the yellow aragonite is always present in contact with banded and botryoidal cement (Fig. 16). The yellow aragonite has been interpreted as fossilized remains of biofilms growing on and within carbonate cements (e.g. Hagemann et al., 2013). It is plausible that the aragonite formed on top of the banded and botryoidal cement during conditions of active seepage by microbial activity. This would explain the intercalation of banded and botryoidal cement and yellow aragonite. This feature has previously been described by Peckmann et al. (2001). On the other hand, the yellow aragonite also chaotically cross-cuts the banded and botryoidal cement (Fig. 16 D). At this point, the formation conditions of the yellow aragonite are not satisfactory explained and more work is

needed to reveal the details of this common mineral phase. The equant calcite spar, occurring within the center of larger cavities, is an abiotically formed carbonate cement precipitated during increased burial and, possibly, after cessation of AOM. This argument is supported by (i) its occurrence as innermost, cavity-filling phase within paragenetic sequences and (ii) by its $\delta^{13}C$ values pointing towards a carbon source other than methane (Fig. 27). The final carbonate phase, late microspar, occurs rather randomly within cavities at Willapa Bay and Knappton. It is an authigenic mineral phase that formed *in situ* within pre-existing cavities. Additionally, it offers an interesting detail: it is the only mineral phase from Siltstone of Shoalwater Bay that displays significant fluorescence.

Pyrite

Pyrite is a common mineral in modern and ancient marine sediments (e.g. Raiswell and Berner, 1985; Wilkin et al., 1996; Wilkin and Barnes, 1996; Peckmann et al., 2001; Peckmann and Thiel, 2004; Neumann et al., 2005). It is an important indicator mineral for past environmental conditions and the formation of its precursor minerals (i.e. iron monosulfides) exerts a strong influence on the chemical composition of the solution in which it formed. Because pyrite is abundant at Willapa Bay, dissolved sulfide played a relevant role in influencing the chemical conditions during seep carbonate precipitation. Pyrite, FeS_2, forms during early diagenesis and shallow burial in marine sediments via the reaction of solid iron minerals with dissolved hydrogen sulfide (Berner, 1984; Raiswell and Berner, 1985), and is the most stable iron sulfide mineral in marine sediments (Neretin et al., 2004). The dissolved hydrogen sulfide is produced by bacterial reduction of seawater sulfate within the sediment column (Berner, 1970, 1984; Raiswell and Canfield, 1998; Schippers and Jørgensen, 2001), in the case of Willapa Bay by the anaerobic oxidation of methane via sulfate reduction. The formation of pyrite essentially depends on, and is limited by, three factors: The amount of organic matter in the sediment, the amount of reactive iron minerals and the amount of available dissolved sulfide (Fig 30.; Berner, 1984).

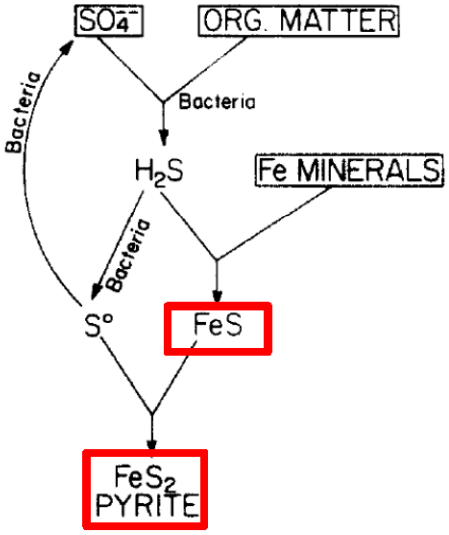

Figure 30: Diagram showing the overall process of sedimentary pyrite formation after Berner (1984)

Since AOM produces dissolved sulfides via sulfate reduction, it is not surprising that pyrite has been frequently observed in methane-seep carbonates (e.g. Peckmann et al., 2001, 2003; Peckmann and Thiel, 2004; Himmler et al., 2008; Kuechler et al., 2012).

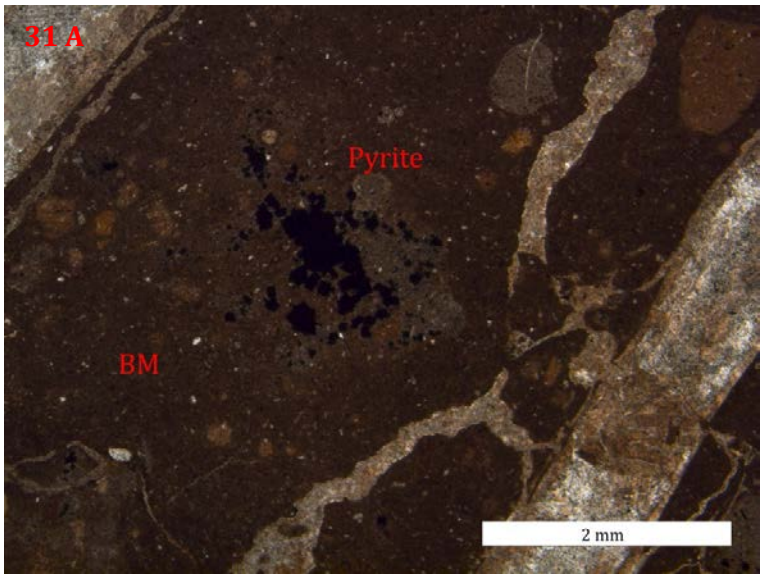

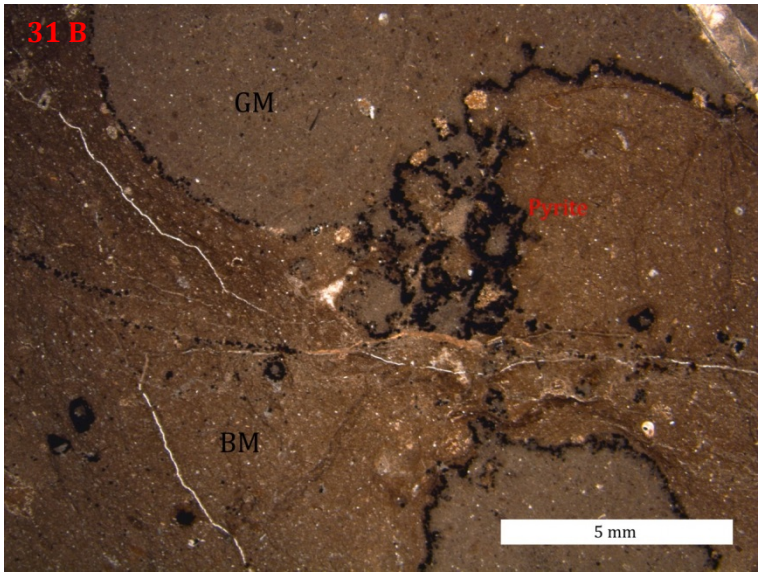

Figure 31 A: Pyrite occurring as larger grains within brown micrite (BM). B: Framboidal pyrite forming rims between gray (GM) and brown (BM) micrite.

Pyrite in Willapa Bay samples is observed in two forms: Larger crystals (Figs. 10 & 31 A) and smaller aggregates forming rims around gray and brown micrites (Figs. 5 B & 31 B). Different crystal morphologies are controlled by crystal structure, defects and growth environment, whereby the latter is considered most important (Wang and Morse, 1996). Both morphologies can be described as framboidal, a texture commonly observed in marine sediments (Wilkin et al., 1996; Butler and Rickard, 2000). The Willapa Bay samples show an inhomogeneous distribution of pyrite, suggesting the importance of microenvironments on pyrite formation (c.f. Jørgensen, 1977; Coleman and Raiswell, 1995; Wang and Morse, 1996). These microenvironments are shaped by sulfate reduction rates, diffusive losses to and from the surrounding porewaters and rates of calcite and pyrite precipitation (Coleman and Raiswell, 1995).

It has been shown that iron sulfide formation has distinct effects on the carbonate buffer and therefore on carbonate formation (Coleman and Raiswell, 1995). Where iron reduction and sulfate reduction are coupled and occur contemporaneously, alkalinity can be increased by the consumption of protons and the production of bicarbonate ions after the following reactions (Coleman and Raiswell, 1995; Peckmann and Thiel, 2004):

$$CH_2O + 4FeOOH + 7H^+ \rightarrow HCO_3^- + 4Fe^{2+} + 6H_2O \qquad (4)$$

$$4CH_4 + CH_2O + 4SO_4^{2-} + 4FeOOH + 3H^+ \rightarrow 5HCO_3^- + 4FeS + 10H_2O \qquad (5)$$

Reaction (5) does not imply that AOM via sulfate reduction and iron reduction are necessarily coupled, but if these processes occur in close proximity, carbonate formation can be even more

favored than by AOM alone (Peckmann and Thiel, 2004). Additionally, Beal et al. (2009) showed that AOM can also be coupled to iron reduction. Pyrite rims, as shown in figure 17, have been reported in seep limestones and often associated with corrosion surfaces (e.g. Campbell et al., 2002; Peckmann et al., 2003; Peckmann and Thiel, 2004). Carbonate corrosion and iron sulfide precipitation can be caused by the migration of ferrous iron and hydrogen sulfide to the reaction site (Coleman and Raiswell, 1995), whereby iron sulfide formation results in increasing acidity:

$$Fe^{2+} + H_2S \rightarrow FeS + 2H^+ \qquad (6)$$

Coleman (1985) showed that sulfate reduction can increase and decrease the pH value of the solution, depending on the availability of iron. Iron oxides can be microbially reduced (Curtis, 1977; Lovley et al., 1990), a process involving the consumption of protons, assisting the precipitation of carbonates. Judging from petrographic observations, micrite from the Willapa Bay deposit precipitated under predominantly anoxic conditions.

Silica

Silica occurs mostly between banded and botryoidal cement and equant calcite spar (Fig. 26). Similar sequences were also observed in other seep carbonates from Washington State (e.g. Peckmann et al., 2002; Kuechler et al., 2012). It has been suggested that AOM, leading to changing porewater chemistry, triggers dissolution during AOM activity and later re-precipitation of silica after AOM activity had ceased (Kuechler et al., 2012). Petrographic observations suggest that such a scenario is feasible since (i) all samples are now devoid of siliceous microfossils, (ii) silica precipitated after the formation of AOM-related phases such as BBC and yellow aragonite, (iii) carbonate cement textures such as aragonite botryoids are partially silicified, pointing towards silicification after AOM. On the other hand, Kuechler et al. (2012) pointed out that the origin of secondary silica phases in sedimentary rock may also be linked to volcanic activity. In the case of the Siltstone of Shoalwater Bay deposits this possibility is theoretical, but not probable. The Siltstone of Shoalwater Bay Formation is in the vicinity of the Miocene Astoria Formation investigated by Kuechler et al. (2012), and overlies intrusive basalts; however there are no intrusive dykes in the proximity of the Siltstone of Shoalwater Bay deposits (J. Goedert, pers. comm., 2012). Mechanisms and processes surrounding silica chemistry, dissolution and precipitation including silica diagenesis are discussed in detail in the "geochemistry" chapter.

5.2 – Implications from stable C and O isotopes

A common feature of seep carbonates is depletion in ^{13}C, as the parent biogenic methane is strongly depleted in this isotope reaching values as low as −110‰ (e.g. Whiticar et al., 1986; Peckmann et al., 2003; Peckmann and Thiel, 2004; Himmler et al., 2008; Kuechler et al., 2012). Isotope values of Willapa Bay micrites are quite heavy compared to other studied seep carbonates. Heavier, even positive carbon signatures at seeps have been reported from certain locations (Peckmann et al., 1999, 2002) and were attributed to methanogenesis due to the ^{13}C enrichment in the CO_2 pool (Irwin et al., 1977). ^{13}C values from various Willapa Bay micrites are all within the range of −14.0 to 1.1‰, micrites from Knappton show similar $\delta^{13}C$ values (−7.8 to −7.3‰) Since carbonates inherit their isotopic signature from their carbon sources, slightly heavier ^{13}C values have also been attributed to mixing of carbon sources from which authigenic carbonates formed, such as marine carbonate, decomposed organic matter or other hydrocarbons than methane (Peckmann et al., 2003; Peckmann and Thiel, 2004: Kuechler et al., 2012). Higher values can also result from the oxidation of thermogenic methane, which is less depleted in ^{13}C than biogenic methane (Stakes et al., 1999). Despite different attempts to explain such high $\delta^{13}C$ values for seep deposits, it remains difficult to separate the reduced carbon sources for mineral authigenesis at ancient cold seeps. Micrites from Willapa Bay and Knappton possibly stem from various carbon sources. The yellow aragonite and BBC on the other hand are more strongly depleted in ^{13}C, showing values between −26.2 and −23.2‰ and −27.6 to −19.3‰ respectively. Considering that yellow aragonite and BBC occur in direct proximity to each other, it is likely that both phases inherited their carbon signatures from the anaerobic oxidation of methane. Equant calcite (blocky) spar, the latest pore filling carbonate, revealed $\delta^{13}C$ values ranging from 4.3 to 7.1‰. Such positive values suggest that this phase precipitated after the cessation of AOM. During progressive burial, the Knappton sediments apparently entered the zone of methanogenesis and the blocky spar precipitated from a pool of dissolved carbonate species affected by methanogenesis, resulting in ^{13}C enrichment. The carbon isotope signatures from the Siltstone of Shoalwater Bay carbonates do not allow a straightforward interpretation. If AOM was the primary mechanism, this should be reflected by rather strongly depleted ^{13}C values, which is not the case. On the other hand, the widespread abundance of iron sulfides, at least at Willapa Bay, requires a productive sulfide source. Most fluids at cold seeps do not contain large amounts of sulfide prior to the onset of AOM (Sibuet and Olu, 1998). It is therefore likely that AOM is the process generating appreciable amounts of dissolved sulfide necessary of pyrite formation, and was also involved in the precipitation of authigenic carbonates.

Oxygen isotope values of micrites reflect strong depletion of ^{18}O reflected in values between −14 to −9.0‰. $\delta^{18}O$ values of Knappton samples are also exclusively negative, ranging from −11.5 to −9.0‰. Previous studies of seep carbonates have shown that earlier phases such as micrite and

banded and botryoidal cement are less depleted than later phases (e.g. Campbell et al., 2006; Himmler et al., 2008). This is a general trend; however micrite is more affected by remineralization than later phases, resulting in the low values. The oxygen isotopic composition of minerals is influenced by mineralogy, temperature during mineral precipitation and the composition of the fluids from which minerals precipitate (Stakes et al., 1999). Processes such as post depositional dissolution and re-precipitation during advanced burial may shift the isotope composition to more negative values; this effect is on orders of magnitude stronger for oxygen isotopes than for carbon isotopes (Campbell et al., 2002; Peckmann et al., 2003). The reason for this is that the surrounding porewater contains much more oxygen than carbon available for isotope exchange (Aharon and Fu, 2000; Campbell et al., 2002; Peckmann et al., 2003). It is most likely that during advanced burial carbonate phases where enriched in ^{16}O due to isotope exchange at elevated temperatures. It is likely that seepage fluids from which the Siltstone of Shoalwater Bay carbonates precipitated had a composition very close to that of marine waters. Isotopic composition of these waters then altered during a later stage after increased burial by interaction with ^{18}O depleted formation waters. *In situ* brecciation may have additionally allowed fluids of various compositions to alter the isotopic signature of the carbonates. Dissociation of gas hydrates can be tracked by heavy oxygen isotope signals (e.g. Bohrmann et al., 1998; Aloisi et al., 2000). However, the reliability of this application with regard to ancient seep carbonates is questionable, particularly due to the ease of oxygen isotope exchange during rock alterations (Peckmann and Thiel, 2004). Since the $\delta^{18}O$ values from Willapa Bay are rather low, it seems feasible that signatures of gas hydrate destabilization were obscured by early diagenetic processes.

5.3 – Conclusion

Petrographic observations suggest that the Knappton seep was a very active one, whereas Willapa Bay experienced less vigorous seepage. Both deposits show abundant seep-specific carbonate fabrics such as peloidal micrites, banded and botryoidal cements, yellow microcrystalline and fibrous botryoidal aragonite. Fecal pellets, which are commonly encountered at ancient seeps, are also abundant. The occurrence of pyrite within large portions of authigenic micrite is a further indicator that the deposits were initially formed in an anoxic, reducing environment, and that sulfides for pyrite formation may have been derived from AOM. Finally, biomarker evidence, which is not included in this study, revealed the presence of the anaerobic consortium of sulfate-reducing bacteria and methanotrophic archaea responsible for AOM. However, ^{13}C compositions of carbonates are not low enough to exclude formation possibilities other than AOM. These values are rather high for seep carbonates, indicating substantial admixture of other carbon sources (e.g. marine carbonate) than methane-derived carbon.

6 – Geochemical modeling

As of today there have been many different attempts trying to model conditions and processes in marine sediments (e.g. Boudreau and Canfield, 1988; Boudreau, 1996; Wang and Van Cappellen, 1996; Hunter et al., 1998; Treude et al., 2003; Thullner et al., 2005; Dale et al., 2008; Thullner et al., 2009). Hydrate Ridge off the coast of Oregon is one example of modern cold seep environments where several modeling efforts have been conducted. These studies have focused on fluid flow, species flux, precipitation of authigenic phases and porosity and permeability changes of the sediment (Luff and Wallmann, 2003; Luff et al., 2004, 2005). Anaerobic oxidation of methane, being the main cause of carbonate generation and important process preventing methane from escaping the sediment, has also received interest in terms of geochemical modeling. An extensive review was published by Regnier et al., (2011), including diffusive and advective species transport, metabolic and biomass modeling and degradation of organic matter.

All of the mentioned studies focus on modern cold seep environments. Direct measurements of fluxes and concentration distributions can be compared to the model results and thus the model can be calibrated to reflect and predict the observed processes as good as possible. This study on the other hand deals with ancient cold seeps. The purpose of this modeling exercise is not to arrive at a full quantitative description of the ancient seep system, but to identify key processes and parameters that have been controlling the system. Sensitivity analyses have been conducted to highlight the relevance of these processes in the system. It was not the purpose to build a complete model. For example, issues such as local porosity and permeability changes of the sediment were not considered here. In order to relate the numerical experiments accomplished here to the conditions which prevailed in the past, thin section description, isotopic composition and biomarker analyses have been conducted, whereby the latter are not included in this work. Comparing the numerical simulation of processes with the sedimentological evidence allows us to ascertain the relevance of geochemical processes under investigation. The main goal of this model is to arrive at a mechanistic understanding of the distribution and dissolution – precipitation history of silica, a common phase at Shoalwater Bay. The PHREEQC code (Parkhurst and Appelo, 1999) was used to describe changing conditions in ancient seep sediments leading to concentration changes and altering species distributions. We performed numerical experiments using the geochemical equilibrium/transport model PHREEQC in order to test the following hypotheses:

1) Anaerobic oxidation of methane leads to a local pH increase in porewaters
2) Increasing pH leads to increasing silica solubilities and dissolution rates
3) Silica dissolution is followed by silica re-precipitation along a pH gradient from AOM hotspots into existing carbonate deposits

An overview of all numerical batch reaction experiments is shown below:

Numerical experiment	Solution species	Heterogeneous reactions			Ca addition	Time [d]
		$CaCO_3$(s)	SiO_2(s)	CO_2(g)		
1	✓	✓				30 & 365
2	✓	✓			✓	30 & 365
3	✓	✓			✓	365
4	✓	✓		✓	✓	365
5	✓	✓	✓	✓	✓	365

Table 5: Overview of numerical batch experiments including or not including solution species, heterogeneous reactions and Ca^{2+} addition.

6.1 – Batch reaction calculations

Numerical experiments simulating simple batch reactions using the PHREEQC code were used to test hypothesis 1 (above) on pH changes as a result of AOM-generated alkalinity increase during carbonate mineral precipitation. The initial porewater composition for the calculations was taken from data from sedimentary porewaters adjacent to seafloor bacterial mats off the coast of Congo (Zabel et al., 2008; see methods). This solution was then equilibrated with the phase assemblage calcite, amorphous silica and a gas phase containing 0.7 mole% carbon dioxide gas. The porosity of the sediment was assumed to be 0.8. AOM was simulated by addition of AOM reaction products to the batch in 10 step increments. The addition of AOM reaction products can be related to time in a real system assuming an AOM reaction rate of 50 mmoles/m^2/d (Torres et al., 2002).

In order to identify the sensitivity of the changing geochemical conditions in a fixed volume of sedimentary porewater over time with respect to individual geochemical processes we performed a series of batch calculations. By comparing the outcomes of numerical experiments that either did or did not include individual geochemical processes, we arrived at a better understanding of the sensitivity of the system towards these processes. The processes under investigation included heterogeneous reactions between the solution and mineral phases (i.e. dissolution and precipitation reactions) and between the solution and a gas phase (i.e. the methane/CO_2 gas mixture characteristic for a cold seep).

Numerical batch experiment	pH change	Ca addition	$CaCO_3$ precipitation	CO_2 degassing	Silica dissolution	Time [d]
1	✓		✓			30 & 365
2	✓	✓	✓			30 & 365
3	✓	✓	✓			365
4	✓	✓	✓	✓		365
5	✓	✓	✓	✓	✓	365

Table 6: Numerical experiments listed with respect to relevant processes considered respectively.

All batch experiments included the full aqueous speciation given by the PHREEQC database and always considered solubility equilibria with calcite and silica. All calculated data for each experiment are listed in the appendix.

6.1.1 – Numerical experiment 1

AOM in a sediment column

The first numerical experiment investigates pH change and calcite precipitation under influence of AOM over a period of one month. The amount of AOM reaction products added were recalculated from values from Torres et al., (2002) and added to the batch in 20 steps.

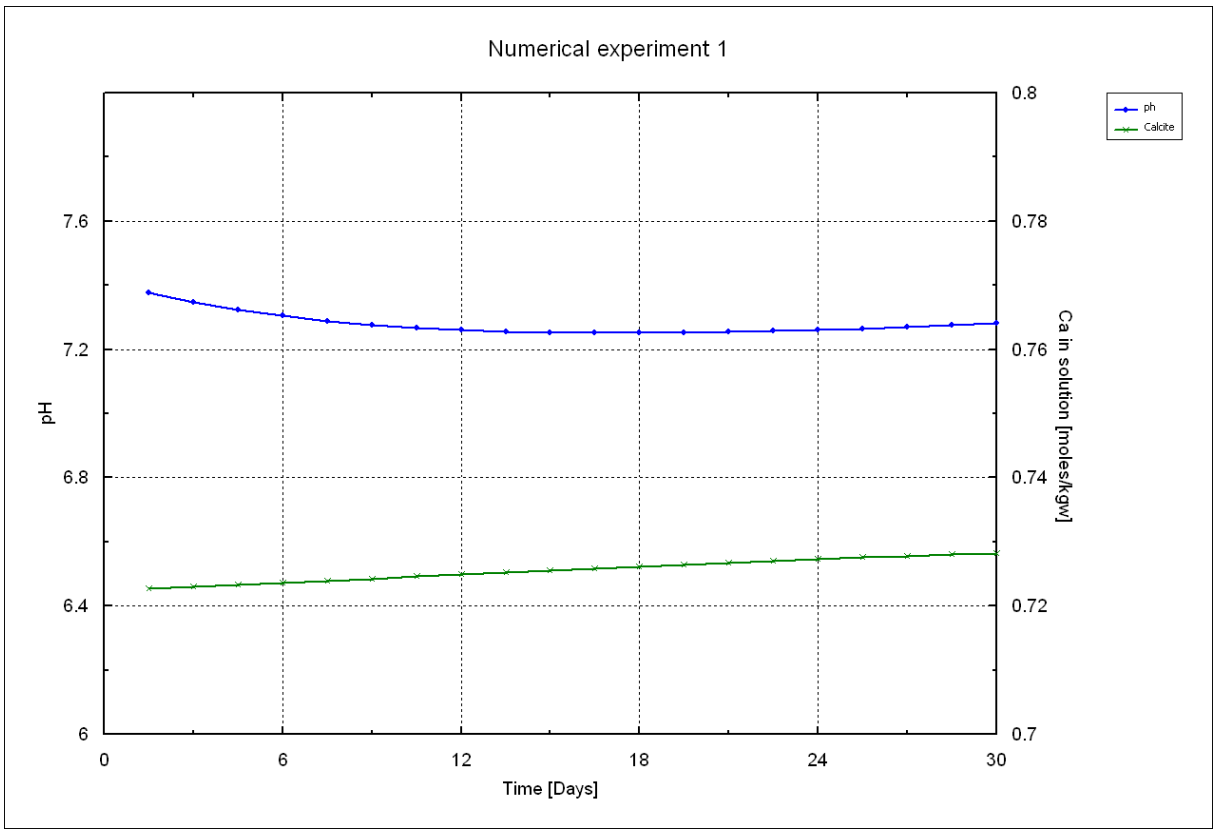

Figure 32: Results from numerical batch experiment 1 showing pH and calcite in the phase assemblage during a period of one month.

Figure 32 shows the results of AOM batch reaction calculations over a period of one month. pH decreases, remains fairly stable and then rises slightly. AOM over one month does not lead to an immediate pH increase. The alkalinity increases simply due to the AOM reaction (data shown in the appendix). This is also the main cause for carbonate precipitation described in the literature (e.g. Luff and Wallmann, 2003; Peckmann et al., 2003). Figure 33 shows calcium concentrations in solution vs. pH using the exact same conditions. Calcium is depleted steadily due to constant calcite precipitation.

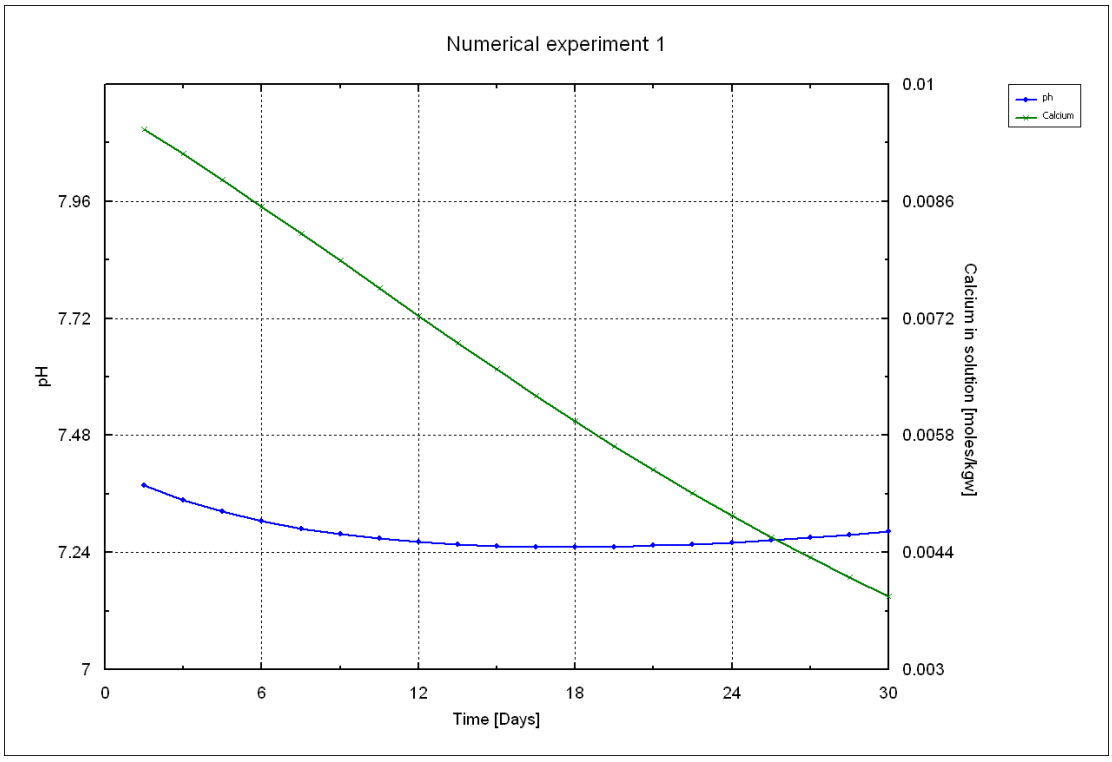

Figure 33: Results from numerical batch experiment 1 showing pH and calcium in solution over a period of one month.

To further illustrate the effect of AOM and calcite precipitation, the same experiment was run over a period of one year:

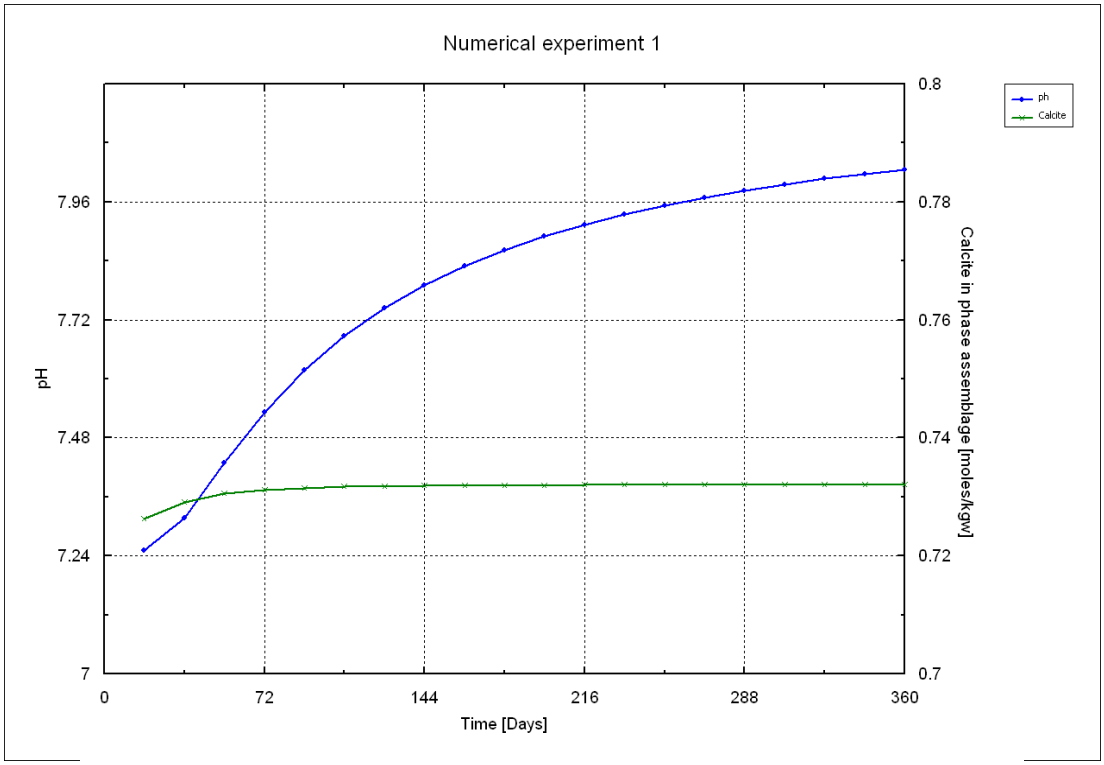

Figure 34: Results from numerical batch experiment 1 showing pH and calcite in the phase assemblage over a period of one year.

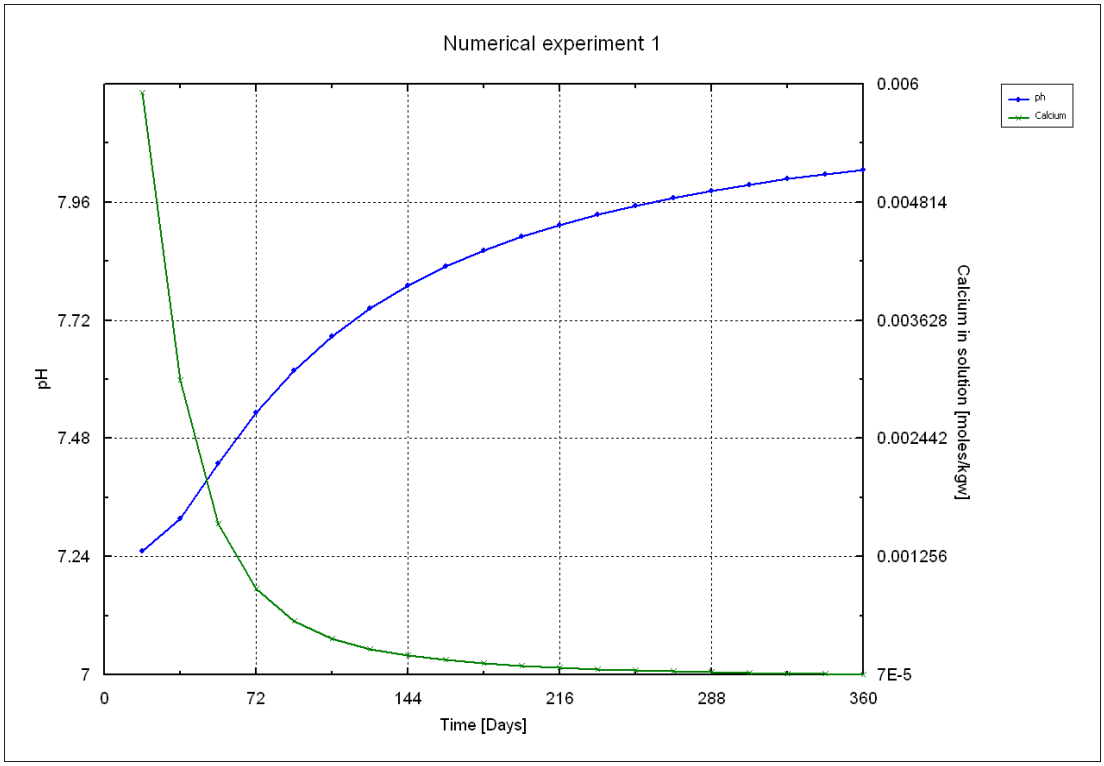

Figure 35: Results from numerical batch experiment 1 showing pH and calcium in solution over a period of one year.

The same experiment conducted over a period of one year shows that pH rises to values over 8 under these conditions. Calcite precipitation reaches a steady – state condition after a period of about two months (Fig. 35) due to rapid calcium depletion in the porewaters (Fig. 36).

The reason why pH decreases initially can be explained by examining which processes occur if bicarbonate is added to a solution:

$$CO_2\,(g) \leftrightarrow H_2CO_3 \leftrightarrow H^+ + HCO_3^- \leftrightarrow CO_3^{2-} + H^+ \qquad (7)$$

Increase ← pH → Decrease

If bicarbonate is added to a solution, it may deprotonate further to carbonate and then react with Ca^{2+} to produce calcite. The reaction to the right of bicarbonate in equation (7) releases protons to the solution, thus decreasing pH:

$$HCO_3^- + Ca^{2+} \rightarrow CaCO_3 + H^+ \qquad (8)$$

Being an amphoteric substance, bicarbonate can also accept protons from solution forming carbonic acid:

$$H^+ + HCO_3^- \rightarrow H_2CO_3 \qquad (9)$$

As calcium is continuously removed from solution, calcite precipitation also declines during each reaction step (data in the appendix), and pH increases.

6.1.2 – Numerical experiment 2

AOM with stoichiometric Ca^{2+} addition

Ca^{2+} depletion in the batch occurs due to calcite precipitation as shown in experiment 1. Such a scenario would eventually lead to a complete calcium depletion and impede calcite precipitation. In this numerical experiment, calcium was added to the solution according to the stoichiometric ratio of calcium to sulfate in seawater as described in the methods section. According to reactions 7 – 9, this addition of calcium to solution should affect pH and calcite precipitation over a period of one month. The idea behind this experiment is to verify that reaction (8) produces a decrease in pH. Addition of Ca^{2+} to solution simulates the influx of seawater Ca^{2+} into shallow sediments, since complete depletion of Ca^{2+} due to carbonate precipitation close to the sediment-water interface (SWI) is unlikely. This idea is supported by the fact that carbonates from Siltstone of Shoalwater Bay show very little porosity and intense pore-filling carbonate cementation.

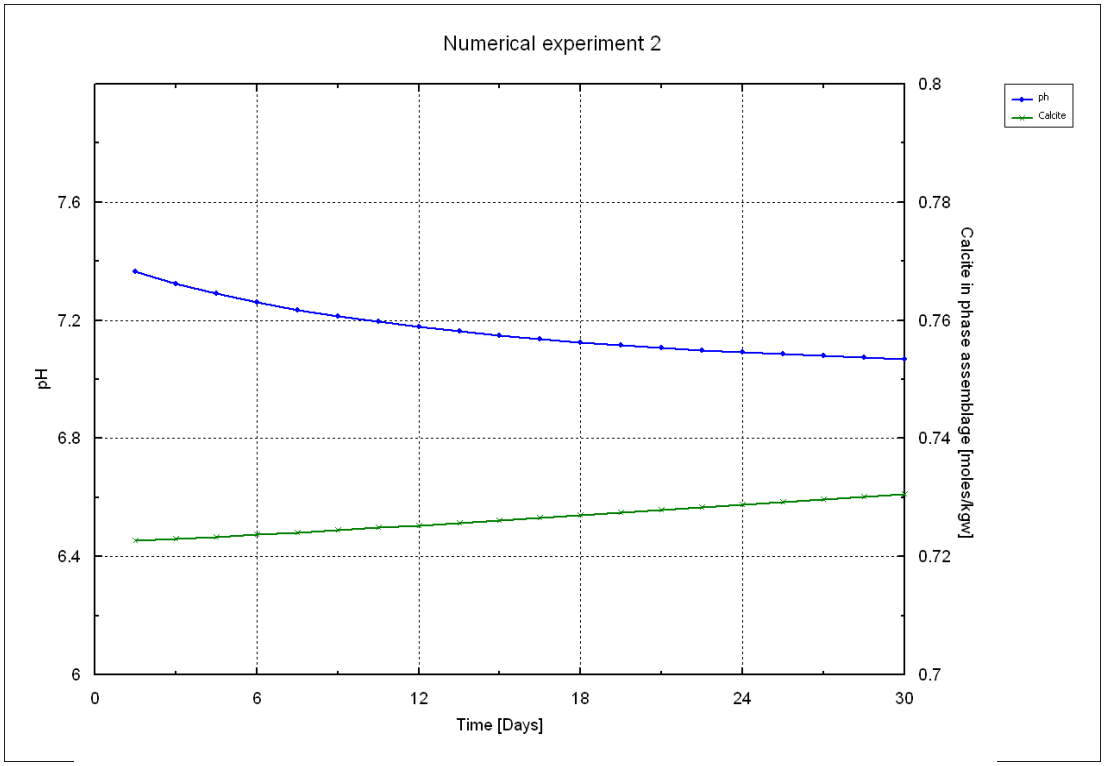

Figure 36: Results from numerical batch experiment 2 showing pH and calcite in the phase assemblage over a period of one month.

In this simulation setup, pH decreases steadily over the entire time period due to ongoing calcite precipitation and reactions (8) and (9) dominating the system (Fig. 36). However this scenario is only valid over a period of one month. The next figures 37 and 38 illustrate pH, calcite and

calcium trends over a period of one year. Amounts of AOM added to solution were recalculated from Torres et al., (2002).

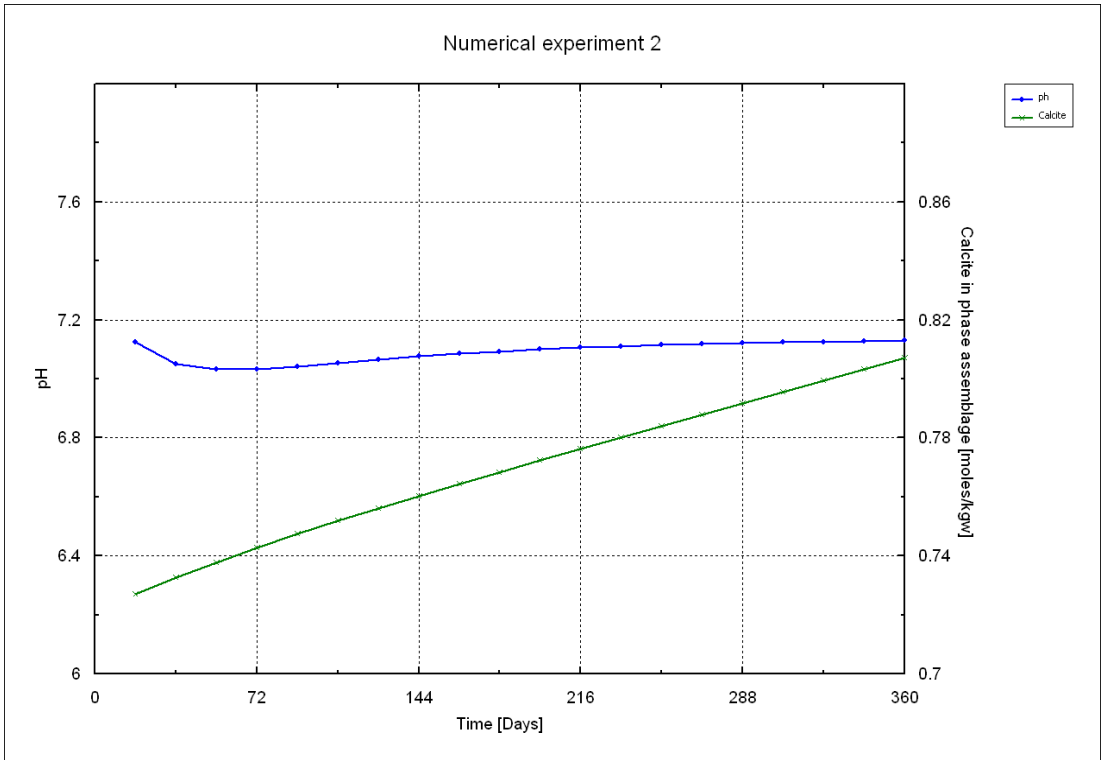

Figure 37: Results from numerical batch experiment 2 showing pH and calcite in the phase assemblage over a period of one year.

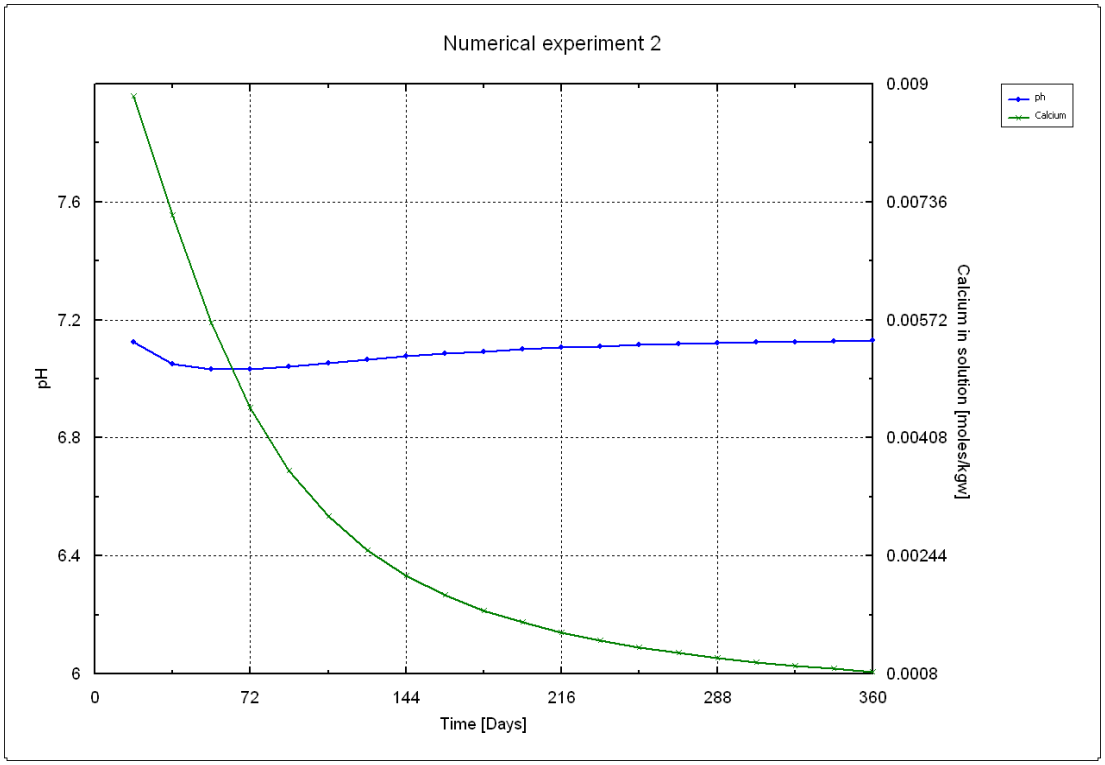

Figure 38: Results from numerical batch experiment 2 showing pH and calcium in solution over a period of one year.

Figures 37and 38 illustrate an initial pH change followed by pH stabilization with constant calcite precipitation and Ca^{2+} depletion. If Ca^{2+} is added to the batch solution corresponding to the seawater SO_4^{2-}/Ca^{2+} ratio, ongoing calcite precipitation still leads to rapid local Ca^{2+} depletion. However, it does not account for higher pH values possibly encountered at cold seep hotspots or as simulated in the first numerical experiment under exclusion of Ca^{2+} addition (Figs. 39 & 40).

6.1.3 – Numerical experiment 3

AOM with stoichiometric Ca^{2+} addition and CO_2 degassing

Clearly, homogeneous and heterogeneous carbonate equilibria control the pH of the solution. So far, we have considered addition of bicarbonate by AOM and precipitation of $CaCO_3$. Another potentially important heterogeneous equilibrium is the removal of carbon dioxide by degassing favored by seepage. This process may become especially relevant at very active seeps where larger amounts of methane are being transported via advection though the sediment column. Torres et al. (2002) reported methane flux rates of up to 10^6 mmoles per m^2 per day along thrust faults and up to 100 mmoles per m^2 per day at bacterial mats. The amount of methane escaping into the water column is controlled by the amount of methane delivered and the efficiency of the methane oxidizing bacterial community to remove methane from porewaters (e.g. Reeburgh, 2007; Knittel and Boetius, 2009; Mogollón et al., 2009). The efficiency of microorganisms to oxidize methane may be as high as 70 – 80% (Wallmann et al., 2006) however if methane fluxes are high enough, higher amounts of methane may escape into the water column. If carbon dioxide cannot escape the sediment and is trapped locally, it may lead to microenvironments in which pH values are constantly low. If gaseous methane is transported rapidly through sediments along faults or conduits or even produces *in situ* brecciation, CO_2 may be additionally removed by this process. Römer et al. (2012) measured up to 0.7 mole% CO_2 in gas phases from high-flux seep areas of the Black Sea. According to equation (7), a decrease of carbon dioxide from solution should result in a shift towards higher pH values. In the next simulations, this degassing effect on local pH and phase precipitation was tested.

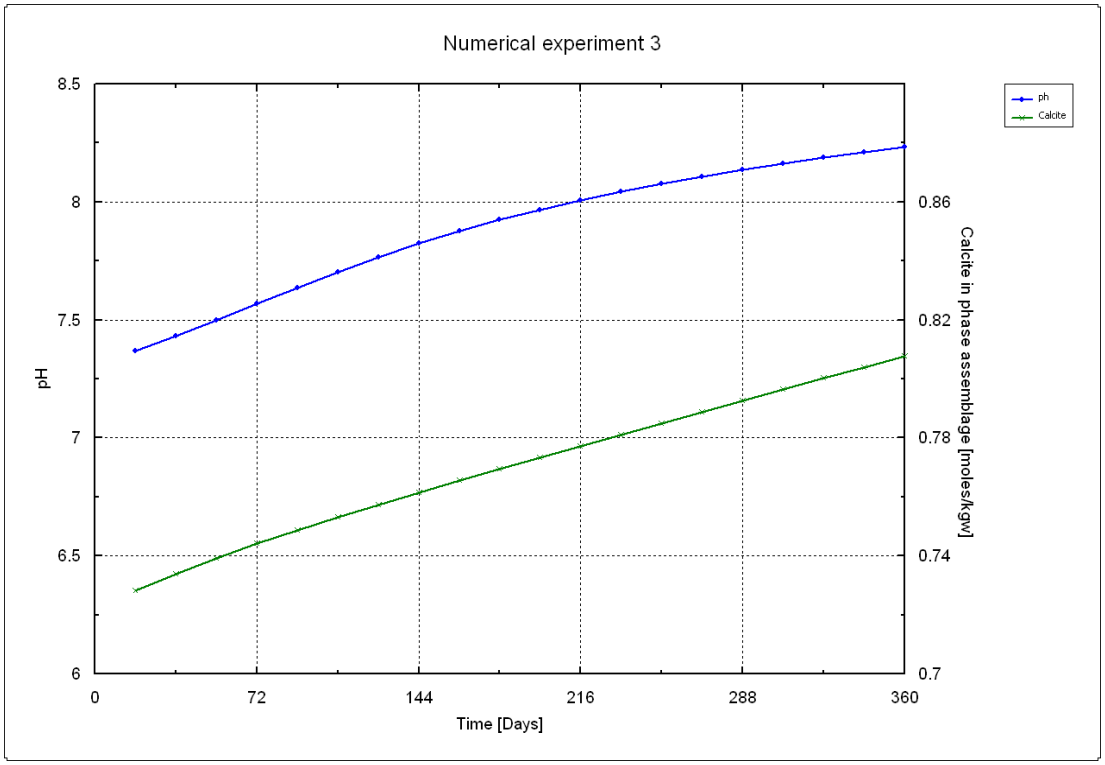

Figure 39: Results from numerical batch experiment 3 showing pH and calcite in phase assemblage over a period of one year.

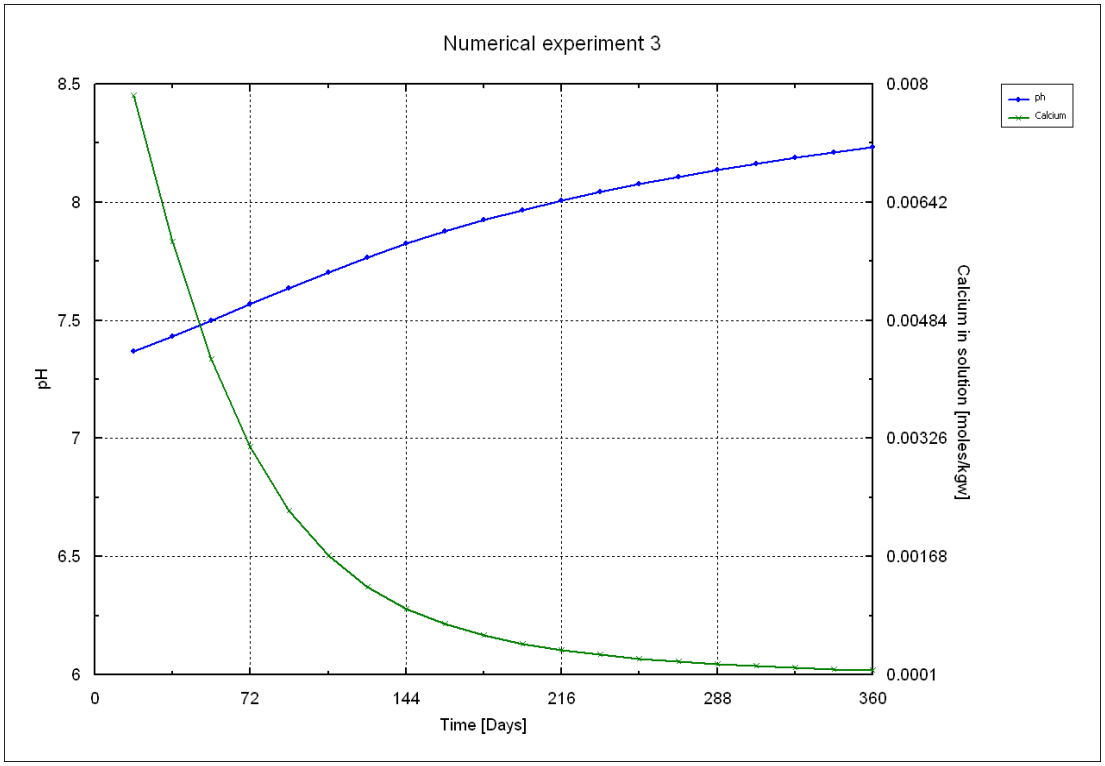

Figure 40: Results from numerical batch experiment 3 showing pH and calcium in solution over a period of one year.

Figures 39 and 40 depict AOM under consideration of stoichiometric calcium addition and CO_2 degassing. The effect on pH is clear when comparing these graphs to those of numerical experiment 2. pH rises up to a value of 8.2 under CO_2 degassing conditions, whereas pH without degassing remains fairly stable at around 7.1 (Figures 37 & 39 for comparison; data available in the appendix). We can conclude from these experiments that CO_2 degassing and calcium availability exert a direct influence on the pH of the solution. These findings lead us to the last numerical batch experiment in which all processes are tested with respect to silica dissolution.

6.1.4 – Numerical experiment 4

AOM with stoichiometric Ca^{2+} addition and CO_2 degassing including heterogeneous reactions with amorphous and crystalline silica

The last numerical batch experiment considered heterogeneous reactions with amorphous silica and quartz. Ca^{2+} addition and CO_2 degassing, as well as the total simulation time were adopted from numerical experiment 3.

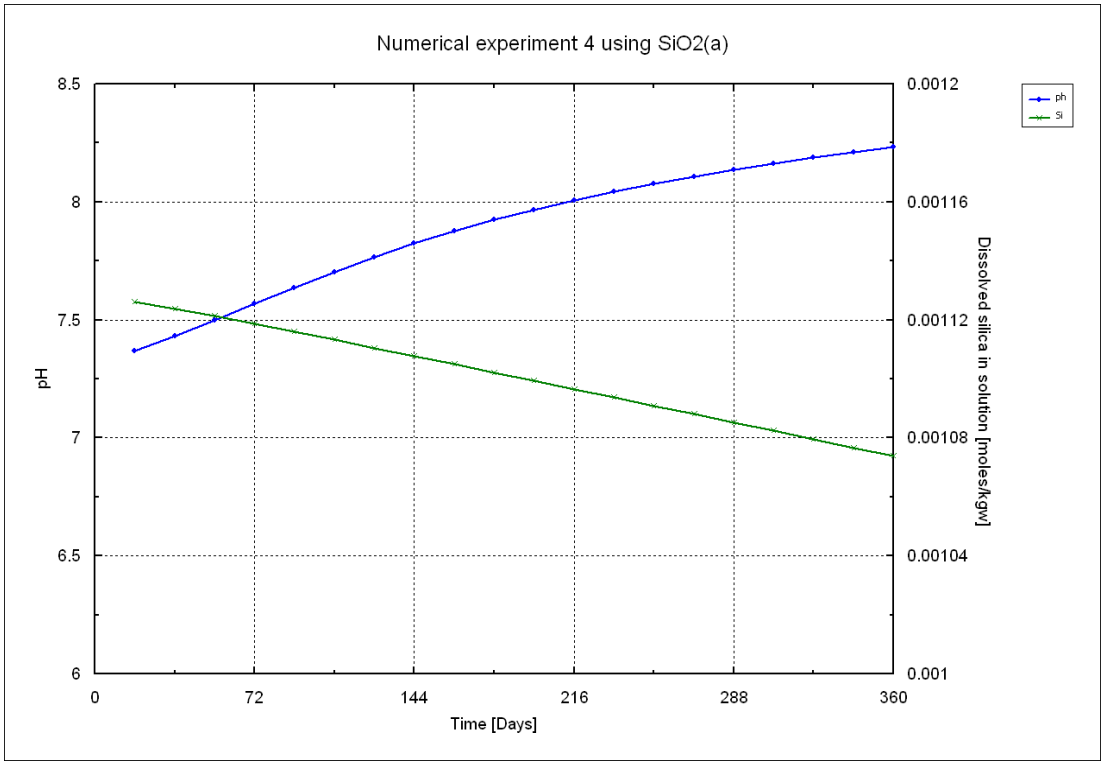

Figure 41: Results from numerical batch experiment 4 showing pH and dissolved silica in solution using amorphous silica in the solid phase assemblage over a period of one year.

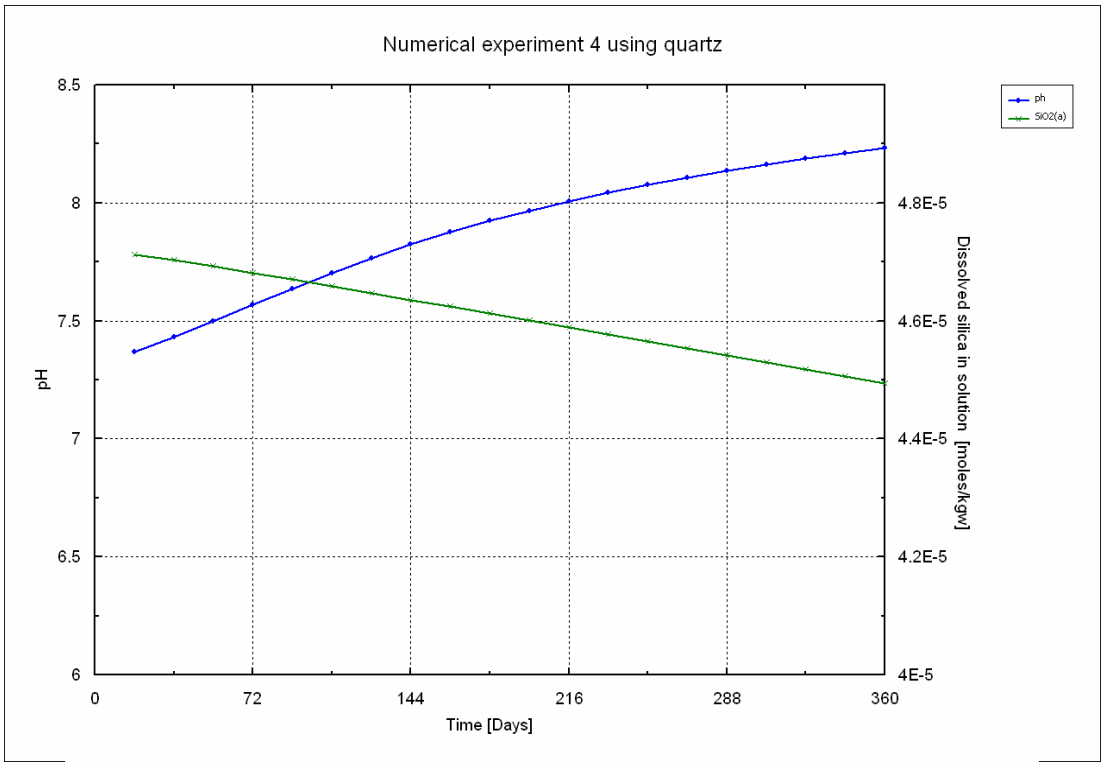

Figure 42: Results from numerical batch experiment 4 showing pH and dissolved silica in solution using quartz in the solid phase assemblage over a period of one year.

Numerical experiment 4 shows that thermodynamically, both silica phases precipitate from solution. The amount precipitated is very low in both cases and increases slightly at higher pH values (data in the appendix). This last batch experiment shows that thermodynamics alone cannot account for silica precipitation and dissolution behavior. Therefore, a second experimental setup was constructed considering silica dissolution kinetics as well as varying AOM and fluid flux rates.

6.2 – Reaction – Transport calculations

One limitation of the batch calculations discussed above is the accumulation of AOM reaction products (e.g. alkalinity) and depletion of solutes by precipitation (e.g. Ca^{2+}) within the reaction volume. This has been dealt with to some degree by additions of Ca^{2+} over time and by keeping the equilibrium gas composition constant. Under natural conditions, advective processes lead to the constant addition of reactants and the removal of products from zones of high AOM rates. Inclusion of flow at flow-rates consistent with field observations (e.g. Torres et al., 2002) allows a more realistic simulation of the geochemical environment in the reaction volume. As discussed above, the silica concentrations in sediment pore waters are not controlled by equilibration with silicate minerals (Van Cappellen and Qiu, 1997a). Therefore, we included a kinetic model of silica dissolution according to Dove (1994). A number of different numerical experiments were conducted and the results are evaluated and discussed in the following section. An overview of the different processes discussed and considered in the following numerical experiments is shown below:

Numerical experiment	Varying AOM rates	pH change	CO_2 degassing	Varying fluid flux	Silica dissolution
5	✓	✓	✓		
6				✓	
7					✓

Table 7: Overview of numerical reaction – transport experiments. This table shows which processes are discussed in the respective experiment.

Numerical experiment	Varying AOM rates	pH change	CO_2 degassing	Varying fluid flux	Silica dissolution
5	✓	✓	✓		
6	✓	✓	✓	✓	
7	✓	✓	✓		✓

Table 8: Overview of numerical reaction – transport experiments. This table shows which processes are considered in the respective experiment and in which section they are discussed.

6.2.1 – Numerical experiment 5

Reactive transport; effect of changing AOM rates over 12 years with and without CO_2 degassing

This numerical experiment simulated a volume equal to the batch calculation and under similar conditions, but with fluid-flow through the reaction zone consistent with previously observed flow-rates of 0.16 cm per day (using data from Torres et al., 2002). This flow rate was re-calculated in terms of the time required to completely exchange one pore volume of the reaction volume, corresponding to 66.25 days. The influent solution had the same composition as the initial pore water composition of the batch experiments discussed above. The total simulation time for the first runs was set to 12 years, corresponding to 66 porewater exchanges in the reaction volume using a fluid flux rate of 66.25 days for one exchange. In this numerical experiment we explored the effect of changing AOM rates over time as shown below:

AOM rate [mmol/m²/d]	**AOM rate [mol/0.01129m²/s]**	**Fraction of AOM rate**	**Time step [a]**
31	$4.05*10^{-9}$	Initial rate	0 - 2
61.3	$8.01*10^{-9}$	2x	2 - 3
$1.24*10^{2}$	$1.62*10^{-8}$	4x	3 - 4
$2.48*10^{2}$	$3.24*10^{-8}$	8x	4 - 5
$3.10*10^{2}$	$4.05*10^{-8}$	10	5 - 5.5
$6.20*10^{2}$	$8.1*10^{-8}$	20x	5.5 - 6
$9.30*10^{5}$	$1.215*10^{-7}$	30x	6 - 6.5
$1.24*10^{3}$	$1.62*10^{-7}$	40x	6.5 - 7
$1.72*10^{3}$	$2.25*10^{-7}$	50x	7 - 7.5
$1.86*10^{3}$	$2.43*10^{-7}$	60x	7.5 - 8
$2.48*10^{3}$	$3.24*10^{-7}$	80x	8 - 9
1.57	$2.05*10^{-10}$	1/10	9 - 10
0.703	$9.19*10^{-11}$	1/100	10 - 11
0	0	0	11 - 12

Table 9: AOM rates and time steps for reaction – transport numerical experiments. Initial rate re-calculated from Wallmann et al., (2006).

The chosen AOM rates are in the range of previously observed AOM rates in cold-seep environments (e.g. Treude et al., 2003; Linke et al., 2005; Wallmann et al., 2006; Dale et al., 2008; Holler et al., 2011). Modifying AOM rates over time enabled the construction of graphs showing differences of parameters of interest as a function of AOM-rates over the total simulation time. Simulated AOM rates span a wide range to better illustrate their effects on other parameters. CO_2 was allowed to degas so that it equilibrated with methane gas containing a constant 0.7 mole% CO_2 as in batch experiments (see above and methods section). The solid phase assemblage was also adopted from the batch reaction calculations.

pH changes as a function of AOM rates

Changing AOM rates (table 9) have a distinct effect on pH, which correlates well with them. An increase of AOM rates between 2 and 9 years by a factor of 80 leads to a corresponding pH increase (Fig. 43 A). During the 8^{th} year of the simulation AOM rates are 80 times higher than those measured by Wallmann et al. 2006. Similar high values have been reported for an AOM community by Holler et al. (2011). This leads to a pH maximum during this time interval. Over the following 4 years AOM rates were lowered to an almost complete stop resulting in low pH near to the pH of the influent solution (Fig. 43 A).

Calcium concentrations and calcium carbonate precipitation

Total calcium concentrations in solution are controlled by a balance of calcium-carbonate precipitation and in- and outflux of calcium by advection through the reactive zone. Calcium carbonate precipitation is driven by alkalinity increases due to AOM (Ritger et al., 1987). Therefore, it is not surprising to find a direct dependence of Ca^{2+} concentrations on AOM rate. Figure 43 A demonstrates that increasing AOM rates lead to a decrease in Ca^{2+} concentrations in solution and vice versa. Solid calcite in the phase assemblage increases steadily during the entire time (Fig. 43 B). The strongly varying AOM rates have only a mild effect on calcite precipitation rates. Comparing figures 43 A and 43 B it becomes apparent that calcite precipitation becomes limited by the depletion of dissolved Ca^{2+}. At maximum AOM rates, the calcite precipitation rate essentially corresponds to the rate of Ca^{2+} influx by advection.

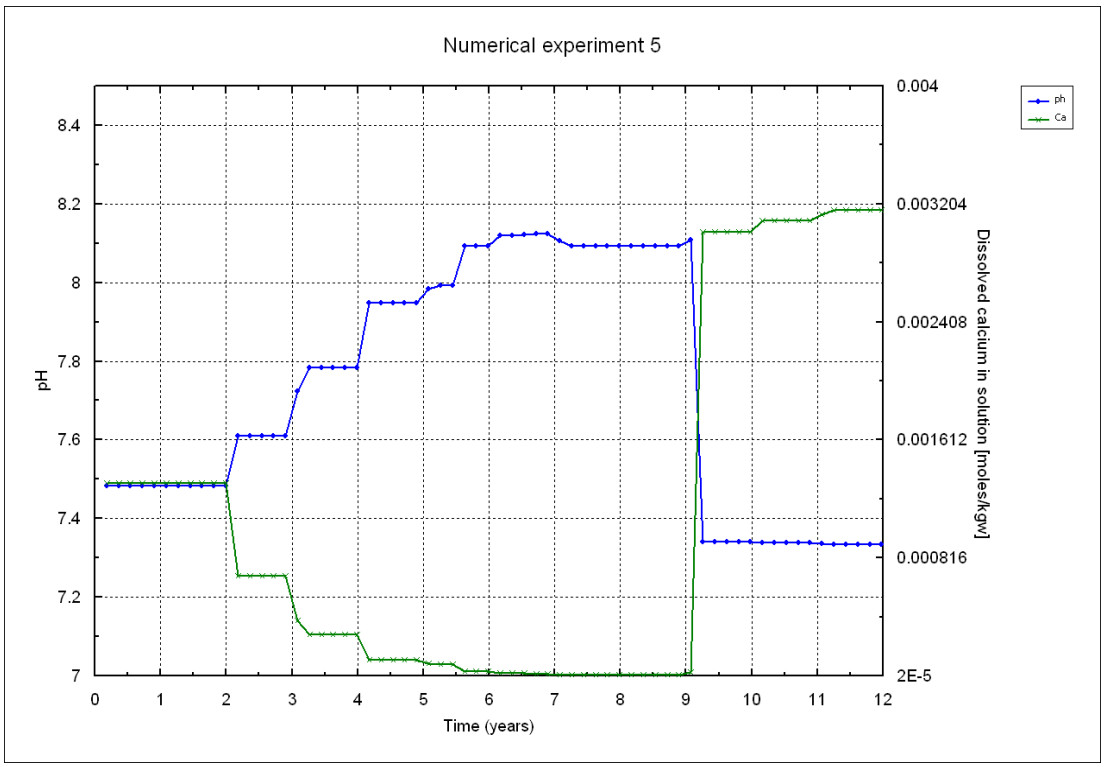

Figure 43 A: Results from numerical experiment 5 showing pH and Ca^{2+} in solution using AOM rates and time steps from table 9.

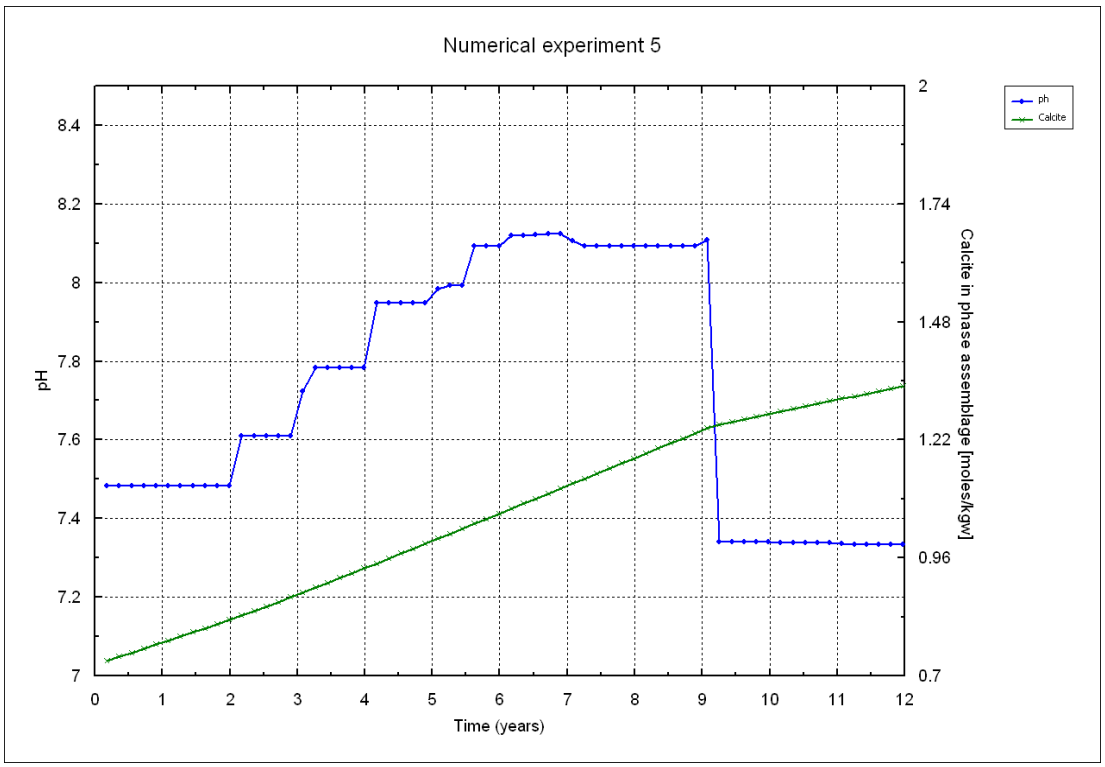

Figure 43 B: Results from numerical experiment 5 showing pH and calcite in phase assemblage using AOM rates and time steps from table 9.

Effect of CO_2 degassing on pH and calcite precipitation

It seems reasonable that CO_2 degasses into discharging fluids flowing through the sediment at a methane seep. However, in systems where methane would be completely oxidized within the zone of AOM, no such degassing would be possible. This would have clear geochemical consequences on the system as was already shown during the batch reaction simulations. Comparing figure 44 A (including CO_2 degassing) with figure 45 A (without CO_2 degassing), it becomes apparent that CO_2 degassing leads to an increase of pH throughout the simulation. However, the amount of calcite in the phase assemblage (Fig. 45 B) remains almost identical with or without CO_2 degassing, as it is largely controlled by advective Ca^{2+} influx rather than pH.

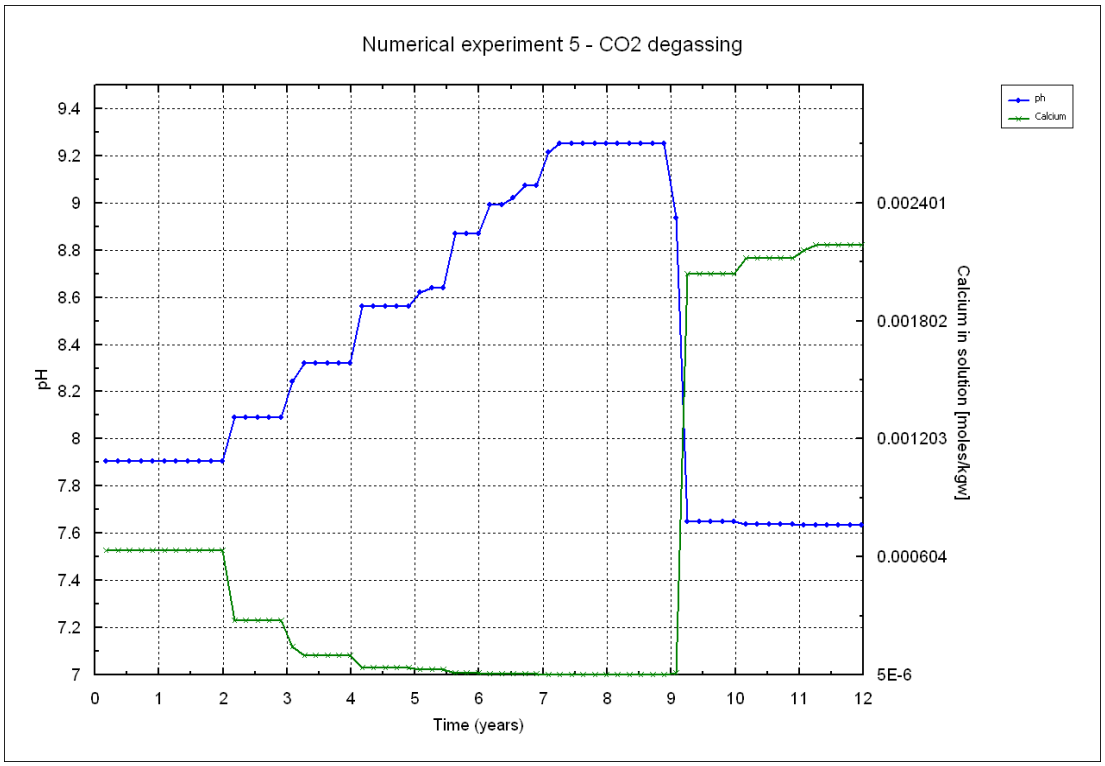

Figure 44 A: Results from numerical experiment 5 showing pH and Ca^{2+} in solution using AOM rates and time steps from table 9 and considering CO_2 degassing.

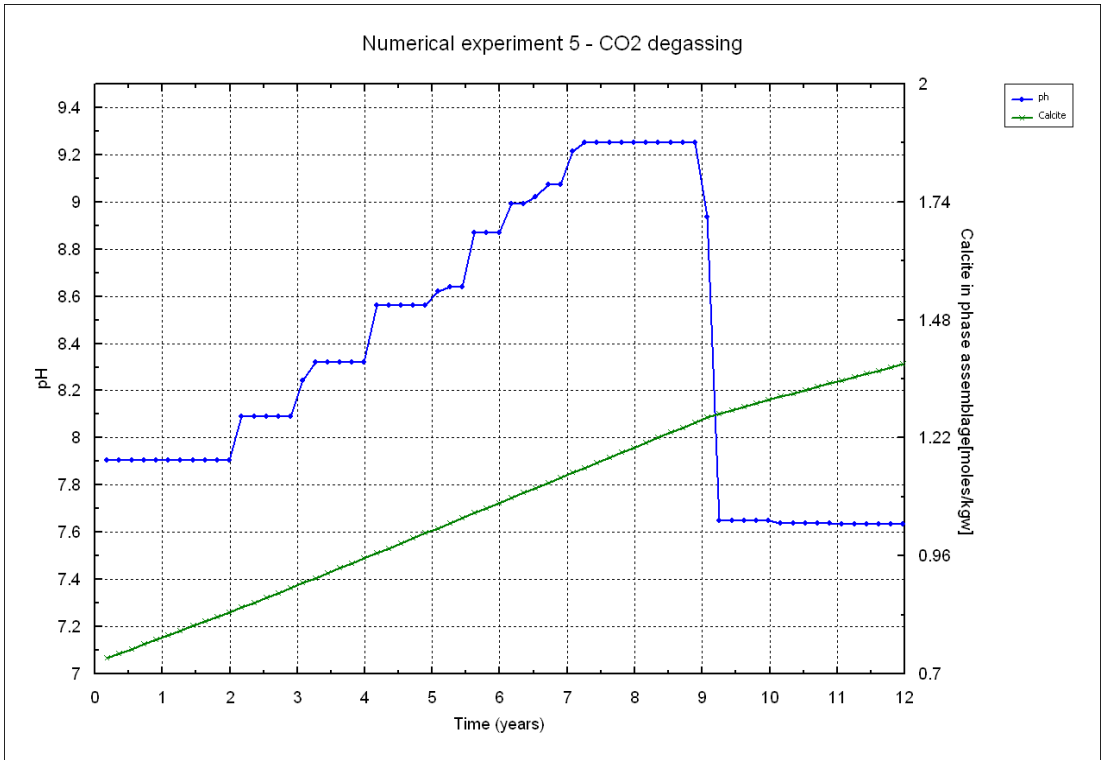

Figure 44 B: Results from numerical experiment 5 showing pH and calcite in phase assemblage using AOM rates and time steps from table 9 and considering CO_2 degassing.

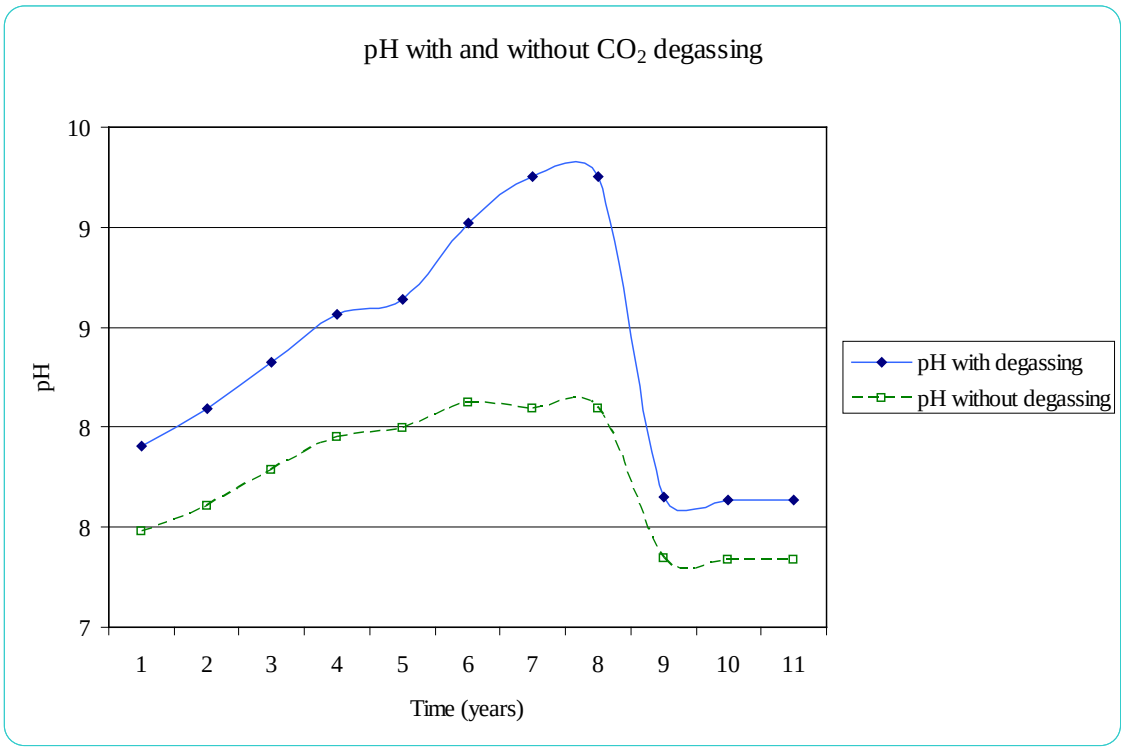

Figure 45: Results from numerical experiment 5 comparing pH values with and without CO_2 degassing using AOM rates and time steps from table 9.

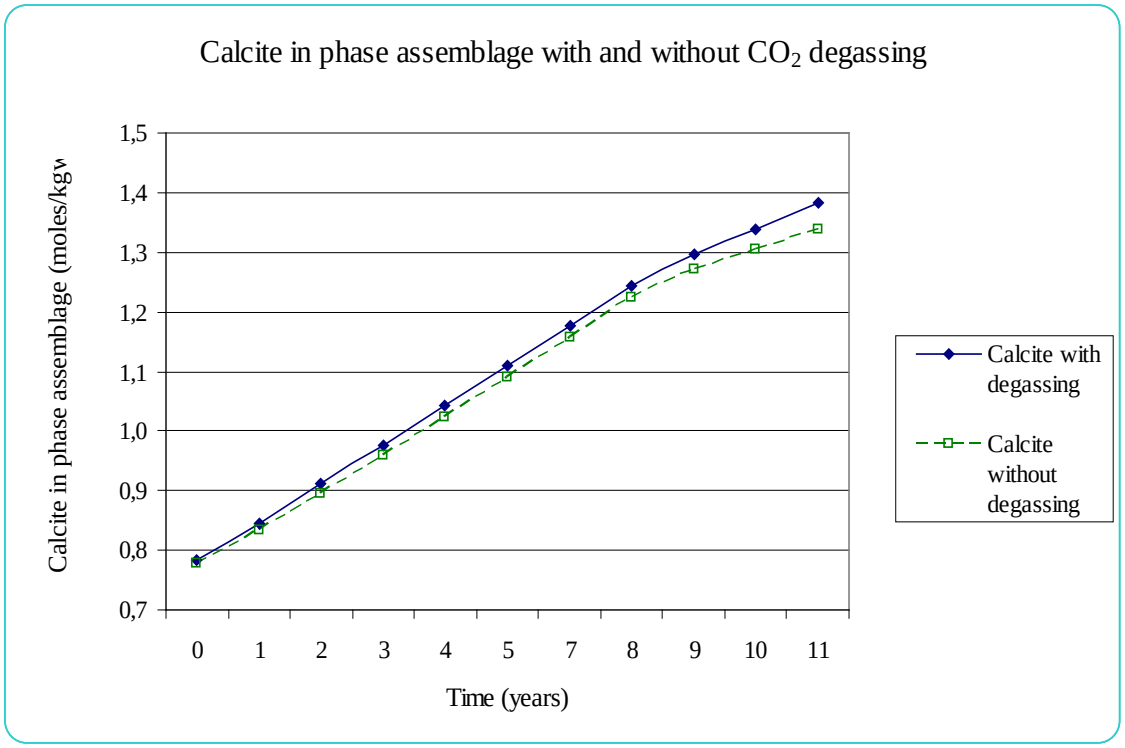

Figure 46: Results from numerical experiment 5 comparing amounts of calcite in the solid phase assemblage with and without CO_2 degassing using AOM rates and time steps from table 9.

Figures 45 and 46 illustrate the effects of CO_2 degassing on solution pH and amounts of calcite in the phase assemblage (data shown in the appendix).

6.2.2 – Numerical experiment 6

Reactive transport; effect of changing AOM rates over 12 years with CO_2 degassing and altering fluid flux rate

Numerical experiment 5 has shown that varying AOM rates influence solution pH and heterogeneous reactions with solid calcium carbonate. Another parameter that affects porewater species is the flux rate of the upwardly advecting fluid though the sediment column. Up to this point, the fluid flux rate was kept at a constant 0.16 cm/d (see methods for details). In this experiment, the fluid flux rate was halved to 0.08 cm/d and compared to the former rate:

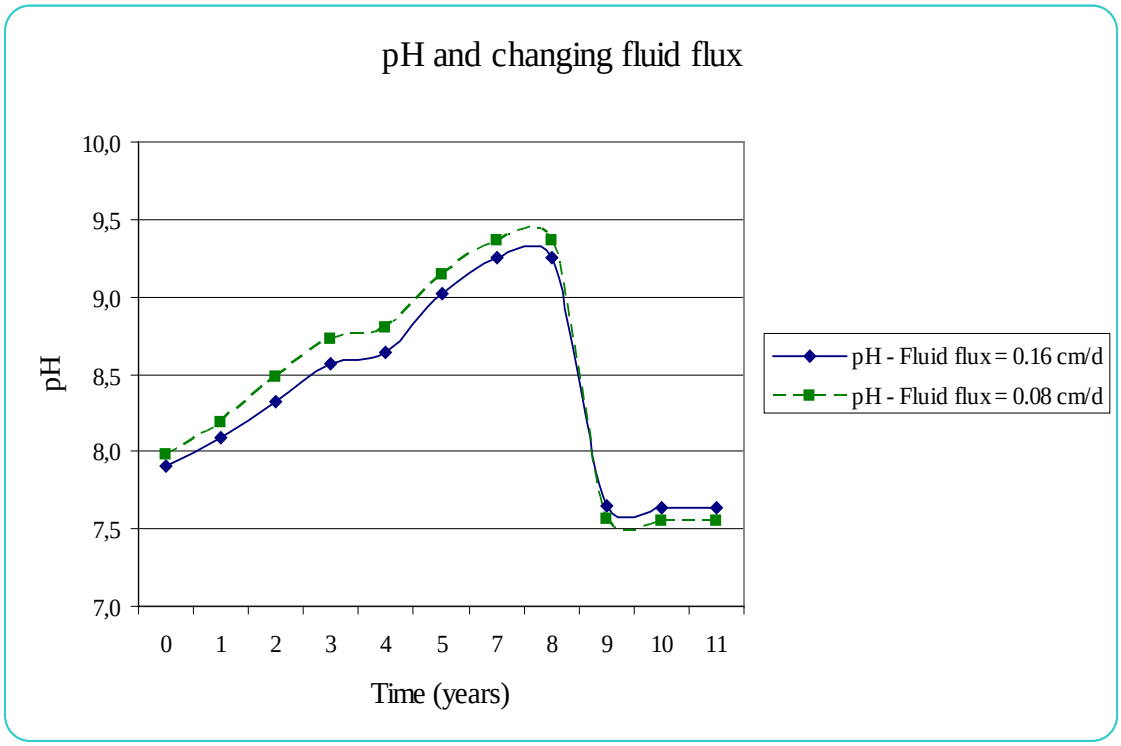

Figure 47: Results from numerical experiment 6 comparing pH under altering fluid flux rates using AOM rates and time steps from table 9.

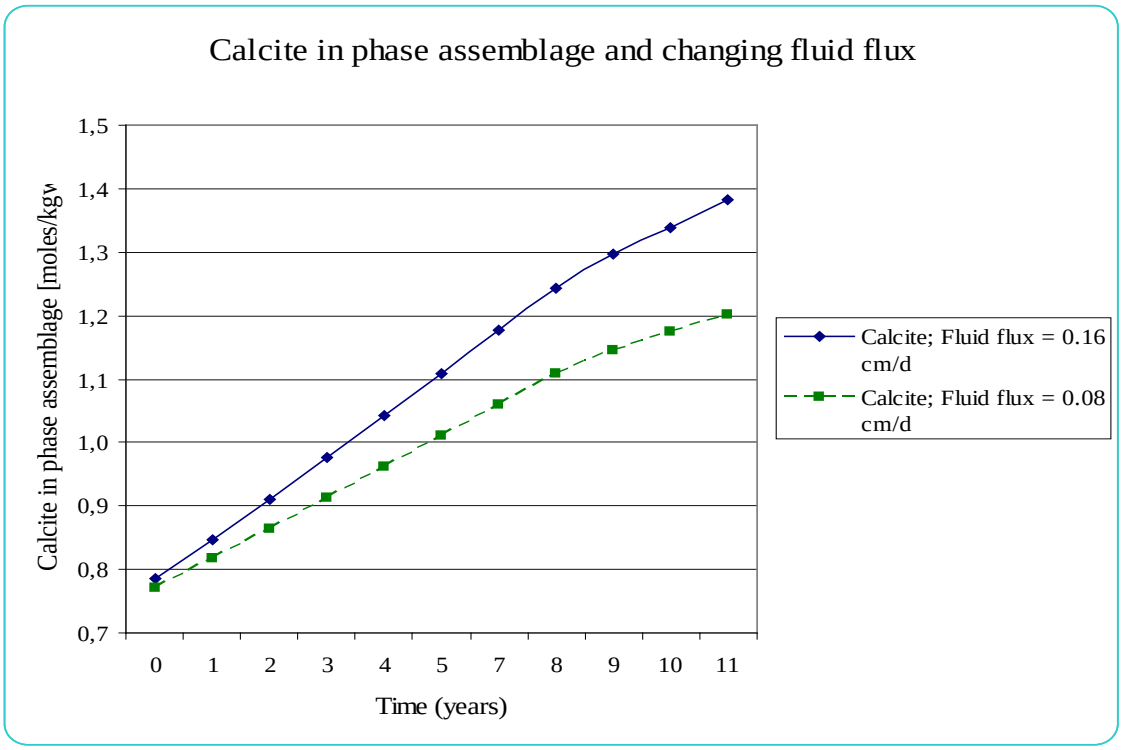

Figure 48: Results from numerical experiment 6 comparing the amount of calcite in phase assemblage under altering fluid flux rates using AOM rates and time steps from table 9.

6.2.3 – Numerical experiment 7

Reactive transport; effect of changing AOM rates over 12 years including CO_2 degassing and heterogeneous reactions with amorphous silica

The last 2 experiments showed that AOM rates and CO_2 affect chemical conditions at a hydrocarbon seep site. This experiment (7) demonstrates these effects on biogenic silica dissolution rates and soluble silica concentrations under consideration of silica dissolution kinetics (see methods for details). Two simulation runs are conducted, with and without CO_2 degassing. As described in the methods section, silica dissolution rates after Dove (1994) are applied. However, these were determined for 1 m^2 surface area. In the following two tables, dissolution rates at varying pH values are listed for 1 m^2 and 230 m^2 of reactive biogenic silica surface area. The constants adopted for silica dissolution rates at various pH values according to Dove (1994) are shown below:

pH	**Silica dissolution rate [mol/m²/s]**	**log rate [mol/m²/s]**
10.8	$3.0027848469*10^{-12}$	-11.52
10.4	$2.7033241626*10^{-12}$	-11.57
10	$2.4101256675*10^{-12}$	-11.62
9.6	$2.1241210430*10^{-12}$	-11.67
9.2	$1.8463727272*10^{-12}$	-11.73
8.8	$1.5784355123*10^{-12}$	-11.80
8.4	$1.3218516036*10^{-12}$	-11.88
8	$1.0792090670*10^{-12}$	-11.97
7.6	$8.5335857656*10^{-13}$	-12.07
7.2	$6.4836783063*10^{-13}$	-12.19

Table 10: pH dependent dissolution rates, calculated using data from Dove (1994) for 1 m^2

pH	Silica dissolution rate [mol/230m²/s]	log rate [mol/230m²/s]
10.8	3.0027848469e-12	-9.158
10.4	2.7033241626e-12	-9.208
10	2.4101256675e-12	-9.258
9.6	2.1241210430e-12	-9.308
9.2	1.8463727272e-12	-9.368
8.8	1.5784355123e-12	-9.438
8.4	1.3218516036e-12	-9.518
8	1.0792090670e-12	-9.608
7.6	8.5335857656e-13	-9.708
7.2	6.4836783063e-13	-9.828

Table 11: pH dependent dissolution rates, calculated using data from Dove (1994) for 230 m²

The graph below shows dissolved silica concentrations over the 12 year period, varying pH and CO_2 degassing:

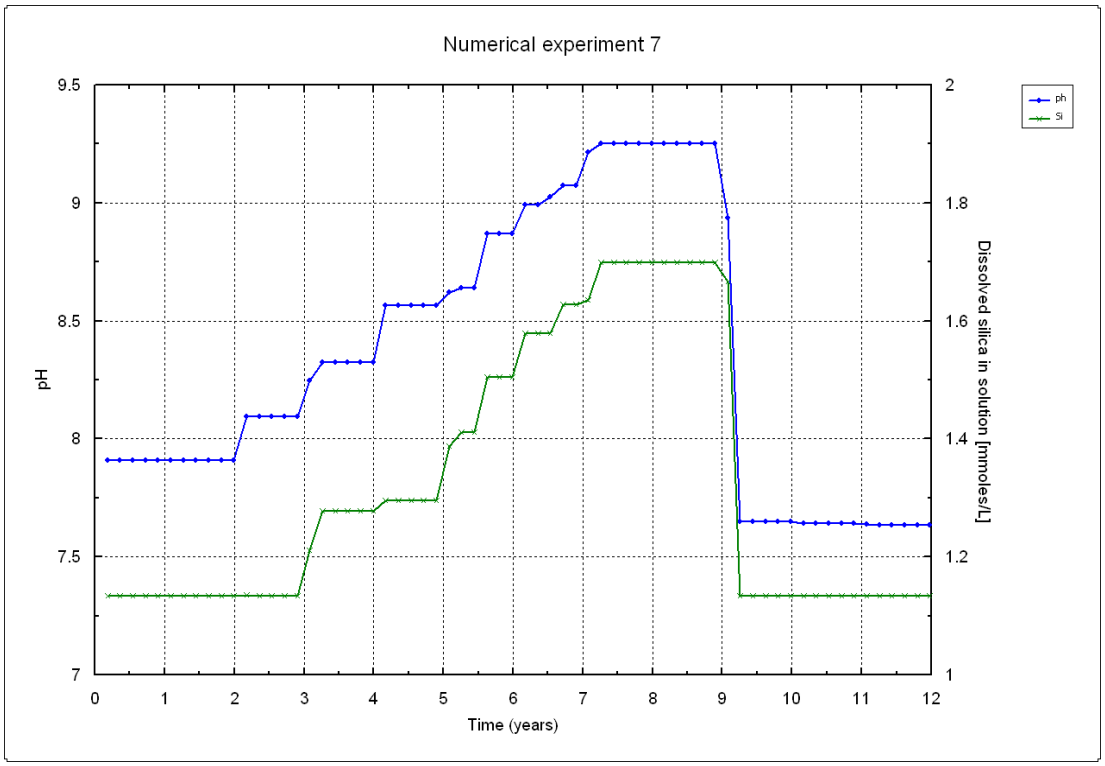

Figure 49: Results from numerical experiment 7 showing pH and dissolved silica in solution

Figure 49 shows that dissolved silica, under application of the dissolution rate equation, increases in the solution with increasing pH. Figure 50 (below) depicts decreasing biogenic silica in the solid phase assemblage with time. The rate of silica depletion (i.e. the first derivative of the biogenic silica solids concentration over time) changes upon strong pH variations. Furthermore, differences in dissolved silica concentrations in solution (Fig. 51) and silica in the solid phase assemblage (Fig. 52) are shown with and without CO_2 degassing. All data are listed in the appendix.

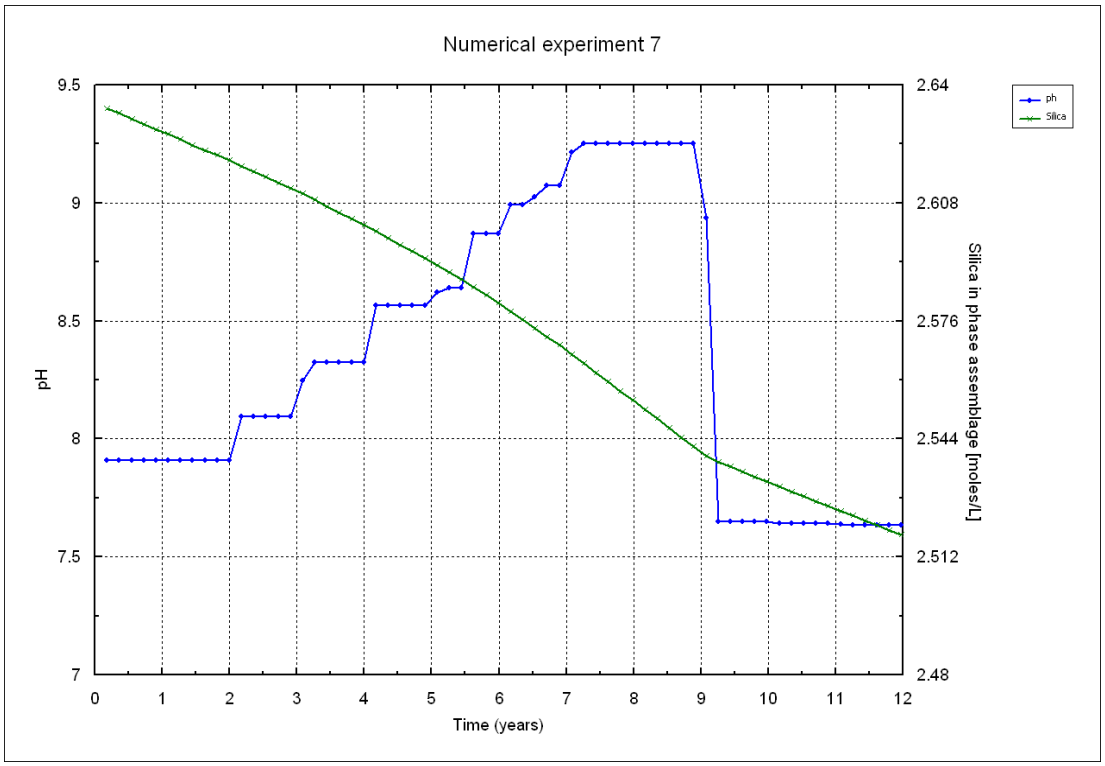

Figure 50: Results from numerical experiment 7 showing pH and biogenic silica in phase assemblage.

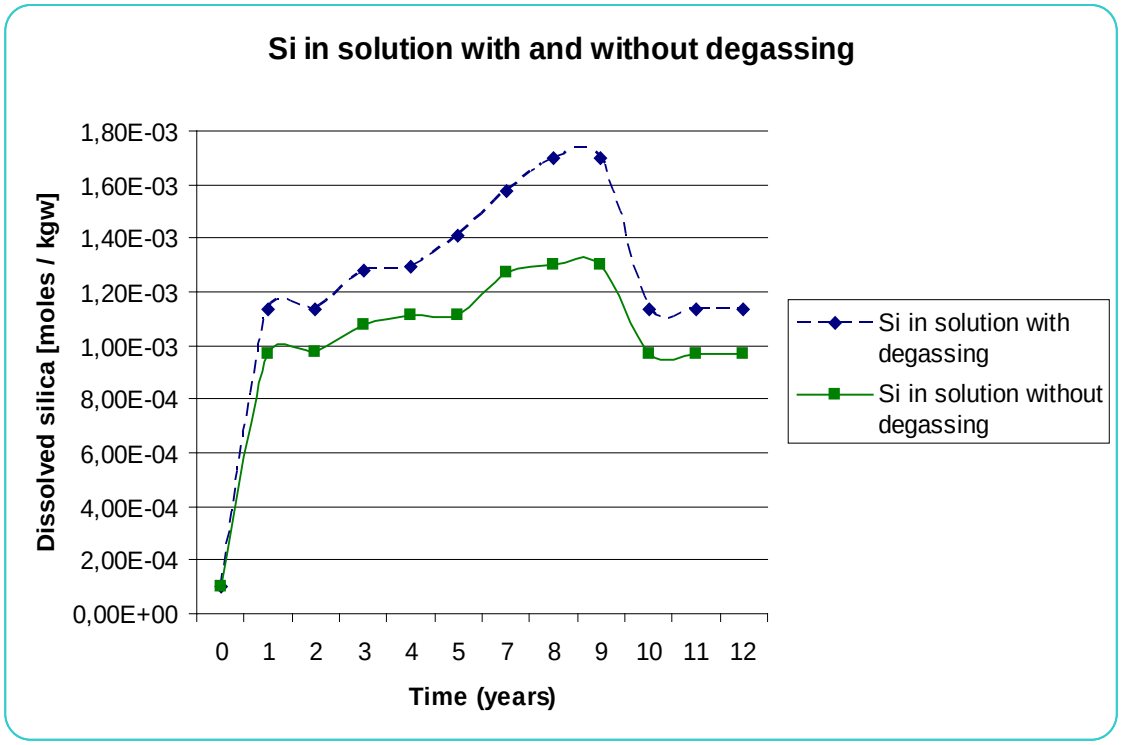

Figure 51: Results from numerical experiment 7 showing dissolved silica in solution with and without CO_2 degassing

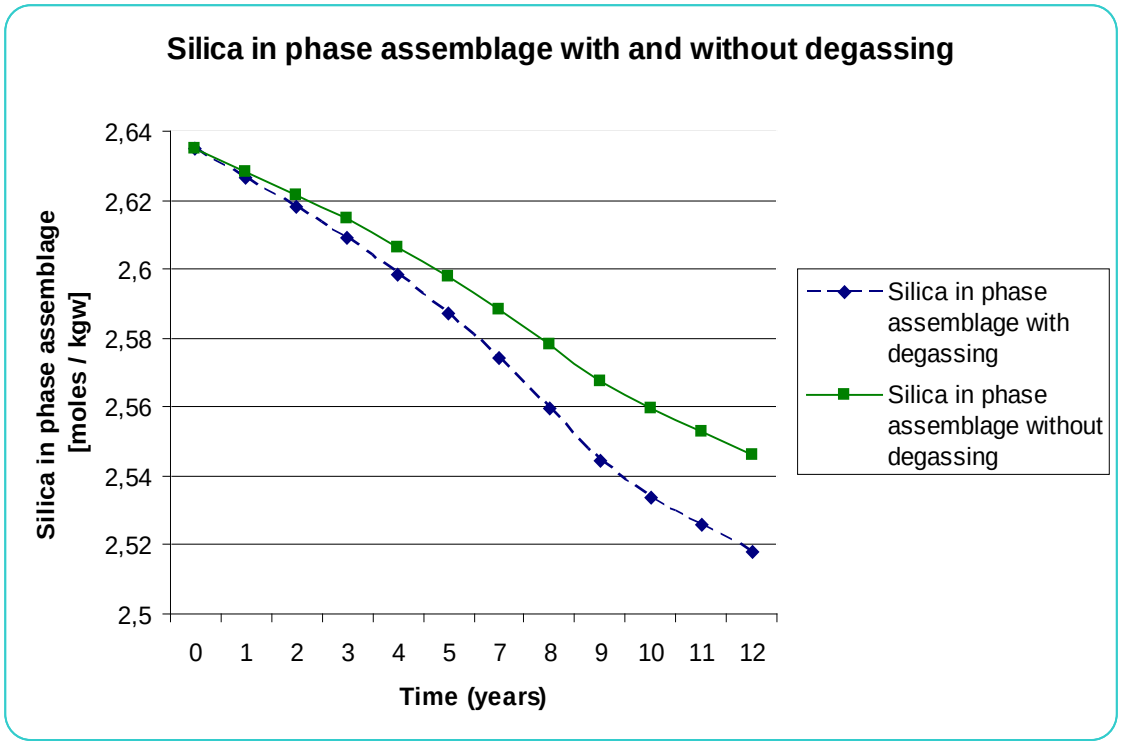

Figure 52: Results from numerical experiment 7 showing silica in solid phase assemblage with and without CO_2 degassing

6.3 – Implications from numerical experiments

Batch reaction experiments demonstrated the effect of various chemical parameters on mineral authigenesis in an AOM – influenced sediment. Carbonate precipitation is controlled by the availability of Ca^{2+} ions in solution triggering a pH decrease due to the release of protons according to reaction (8). Increasing alkalinity produced by AOM enhances precipitation and should therefore lead to a local pH decrease. When considering reaction stoichiometry only, AOM and carbonate authigenesis do not trigger a pH increase, but rather a pH decrease. An additional process is necessary to induce an increase in pH. When considering the carbonate equilibrium (7), pH increases when the reaction equilibrium is shifted to the left. This may occur when CO_2 degasses from the system, leading to protonation of carbonate and bicarbonate ions, compensating the loss of carbonic acid and reducing H^+ concentrations in solution. It has been shown that although methane gas makes up the better part of gasses escaping from modern cold seep sites (over 95% e.g. Römer et al., 2012), gasses seeping out from such systems do contain small amounts of CO_2. The corresponding low CO_2 partial pressure provides a driving force for degassing. Local calcite precipitation in seep sediments add protons to solution, reacting with bicarbonate and producing carbonic acid according to reaction (9). If during more vigorous seepage methane gas is being moved upward towards the sediment – water interface via advection, CO_2 gas may also be purged from the system by methane degassing. Hence, the removal of carbon dioxide via gas seepage is ultimately responsible for local pH changes. Accordingly, variations of advective fluid flux influences the rate of calcite precipitation, leading to increased calcite in the solid phase assemblage due to enhanced CO_2 degassing (Figs. 47 and 48). These considerations are supported by the fact that AOM is common in most marine sediments (e.g. Knittel and Boetius, 2009), yet carbonates do not precipitate everywhere in amounts comparable to those encountered at more active methane seeps. Heterogeneous reactions with silica, which were considered in the last numerical experiment, are discussed in detail in the following section.

7 – Biogenic silica

The occurrence of gas seepage, subsequent removal of CO_2 from sedimentary porewaters and the resulting pH changes may have an important influence on the geochemical behavior of biogenic silica in seep sediments such as the Siltstones of Shoalwater Bay Formation. Authigenic silica phases have been found in various ancient hydrocarbon seep carbonates (e.g. Peckmann et al., 2002, 2011; Kuechler et al., 2012). In this context, the elucidation of dissolution and precipitation processes of biogenic silica phases in ancient seep carbonate rocks is one of the main goals of this study. The following excursion will give an overview on what is known about the behavior of biosiliceous material in modern sediments.

7.1 – Biogenic silica – geochemical implications

Dissolved silica sustains a significant fraction of the oceanic primary production, which is carried out by diatoms (Nelson et al., 1995). Biogenic silica that survives water column dissolution processes reaches the seafloor, and the main sink for silica in the oceans is burial within marine sediments (Tréguer et al., 1995; Schlüter and Rickert, 1998; DeMaster, 2002). Average compositions of several silica phases of modern marine sediments may range between 25% and 90% biogenic silica content (Van Cappellen and Qiu, 1997). Silica dissolution in the sediments produces an efflux of dissolved silica into the porewater (Van Cappellen and Qiu, 1997). Solubilities of silica phases can depend on numerous factors, the most prominent being pH, temperature, pressure (Loucaides et al., 2012) and Al content of the porewater (Van Cappellen and Qiu, 1997). The solubility of diatom frustules particularly depends on additional factors such as the physicochemical properties of the material, water and impurity content and the specific surface morphology and area (Hurd and Birdwhistell, 1983; Beck et al., 2002; Dixit and Van Cappellen, 2002).

Effect of pH on dissolution rates

The effect of pH on silica dissolution rates is of particular interest in this study since AOM, carbonate precipitation and particularly CO_2 degassing has an effect on porewater pH at seeps as shown by the numerical experiments. It is generally accepted that dissolution rates of silica phases, biogenic and synthetic, depend on the pH value of the solution (e.g. Hurd, 1972; Crerar and Dove, 1990; Van Cappellen and Qiu, 1997b; Schlüter and Rickert, 1998; Dove, 1999). The effect of pH on silica dissolution rates is shown in figure 53. When water molecules advance towards the surface of a silica mineral, it weakens and breaks siloxane groups. These open

linkages bind with the dissociated water molecules producing silanol groups (=Si-OH) on the surface of the mineral. A consequence of pH increase of a solution is deprotonation of functional groups on mineral surfaces. Silanol groups are such functional surface groups, which deprotonate; a process facilitating the breaking of siloxane bonds (Wirth and Gieskes, 1979; Fleming, 1986; Brady and Walther, 1990; Dove and Elston, 1992). This catalyzing effect of higher pH on silica dissolution has not only been shown for marine diatoms (Van Cappellen and Qiu, 1997) but also for plant phytoliths (Fraysse et al., 2006). Appreciable dissociation of surface silanol groups only occur at pH values greater than 6, and even at pH values of 8.5 - 9, the majority of silanol groups remains undissociated (Dixit and Van Cappellen, 2002) and the increase of surface charge on biogenic silica can be explained in terms of the abundance and acidity of surface silanol groups (Dixit and Van Cappellen, 2002). Dissolution kinetics of silica and other minerals are further related to mineral surface charge (Stumm, 1992), and pH dependent silica dissolution rates have been correlated to the distribution and abundance of these surface SiO^- groups (e.g. Dove and Elston, 1992; Dove and Rimstidt, 1994; Dixit and Van Cappellen, 2002).

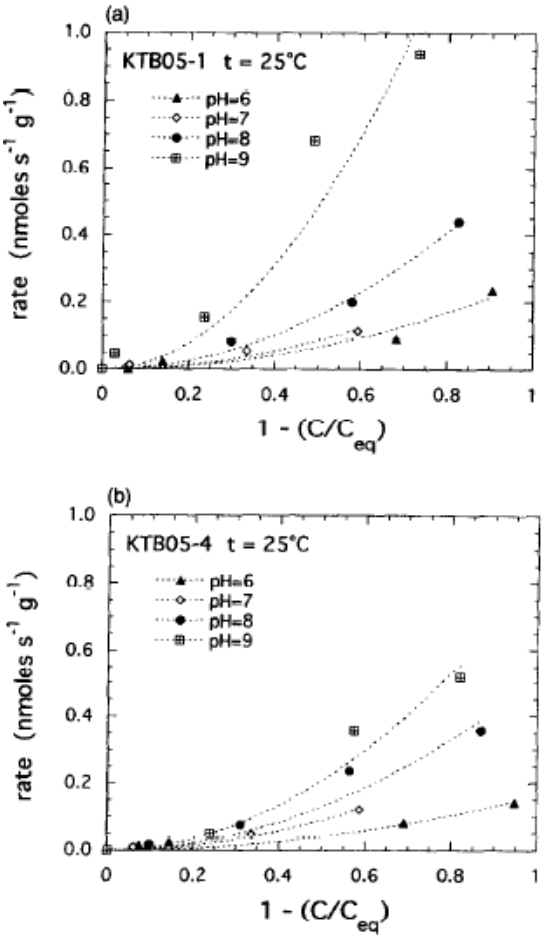

Figure 53: Effect of pH on the net silica dissolution rate at 25°C in modern marine sediments (Taken from Van Cappellen and Qiu, 1997).

Surface area, reactivity and aging

Dissolution rates of biogenic silica are related to the reactive surface area of the mineral. This reactivity declines with ongoing burial in the sediment (Van Cappellen, 1996). It was shown that decreasing reactivity and dissolution rates are related to the progressive loss of reactive surface sites. Additionally, biosiliceous material in modern marine sediments has a lower reactive site density than cultured or planktonic diatoms (Dixit and Van Cappellen, 2002). Aging processes lower the intrinsic reactivity of biogenic silica surfaces during burial in sediments, an effect that was demonstrated by Van Cappellen and Qiu (1997). However, this trend did not correlate with variations in specific surface area, composition or inorganic coatings (Van Cappellen et al., 2002; Dixit and Van Cappellen, 2002). On the other hand, decreasing reactivity of biogenic silica does

apparently increase at sediment depths where no net dissolution occurs and correlates with decreasing adsorption capacity of ions such as cobalt (Van Cappellen and Qiu, 1997). These observations provide indirect evidence of biogenic silica aging and a corresponding disappearance of reactive surface sites (Dixit and Van Cappellen, 2002).

7.2 – Biogenic silica – Siltstone of Shoalwater Bay

Implications from numerical experiments – AOM and silica dissolution

The influence of the advent and cessation of AOM at seep sediments on silica transformation has been observed previously (e.g. Kuechler et al., 2012). Diagenetic transitions of biogenic silica in sediments are also controlled by kinetic processes that are highly dependent on pH (e.g. Dove, 1994). The influence of AOM in cold seeps on pore-water pH was shown above. In numerical experiment 7, the effect of AOM-related pH changes on silica dissolution was investigated. The initial solution used for this experiment used data from Zabel et al. 2008, who measured porewater parameters including pH and dissolved concentrations of silica, hydrogen sulfide and sulfate. Experimental dissolution rates of silica were re-calculated for 230 m^2, adapted to experimental solubility results (see methods), corresponding to ~0.6 m^2/g of biogenic silica actually reacting with the solution. This surface area is very small and would mean that almost none of the biogenic silica within the sediment dissolves at all and exhibits very little reactive surface sites. Aging processes, i.e. the reduction of reactive surface sites with time, are not included in the model, however the low surface area assumed for biogenic silica corresponds to a state where silica particles have already been altered to a large extent. Under application of the equation after Dove (1994) and dissolution rates from table 11, solubilities of silica as shown in figure 49 are not surprising. However, if dissolution rates from table 11 are applied, silica dissolution continues up to a point where the pH is much lower. In figure 50 it appears that the rate at which silica dissolves from its solid state does not change dramatically during the sharp drop in pH. During the 12-year period, 0.117 moles of silica are dissolved from the phase assemblage, amounting to ~4.5% of the total initial amount (see appendix for data). This would mean that it would take ~270 years for the total silica present to dissolve using AOM rates from table 9. Under simple modification of AOM rates, 6.2% and 3.3% of the total silica will be dissolved using highest (80x the measured rate by Wallmann et al., 2006, see table 9) and no AOM rates respectively. This corresponds to total silica depletion in ~190 and ~360 years respectively. To summarize, total solid silica depletion would occur around 50% faster at high, persistent AOM rates than without AOM.

Biogenic silica at Knappton – diffusion and precipitation

Silica dissolution rates calculated for numerical experiment 7 solely account for dissolution of silica phases. Silica dissolution occurs at faster rates at high pH due to effects discussed above, and high AOM rates in seep sediments subsequently produce local, increased concentrations of dissolved silica. The outcome of this effect is twofold, (i) it locally increases the saturation state with respect to all silicate minerals and (ii) produces a $H_4SiO_{4(aq)}$-concentration gradient from the site of AOM towards the peripheral sediments and the already precipitated carbonate, where AOM does not occur. The input solution used data from Zabel et al., 2008 who measured porewater concentrations of silica in the periphery of an active methane seep. Unfortunately, it is difficult to measure porewater pH and concentrations of dissolved species directly at an AOM hotspot, as penetration of measuring tools (i) may be obstructed by the presence of solid carbonate and (ii) would disrupt and alter the delicate redox conditions below the sediment-water interface leading to erroneous measurements (J. Peckmann pers. comm., 2012). Measured concentrations in the surrounding sediments range between 0.3 and 0.6 mmoles/L, whereas calculated dissolved silica concentrations from numerical experiment 7 lie between 1.1 and 1.7 mmoles/L at no and high AOM rates respectively. This shows that dissolved silica concentrations may be 3 to 5 times higher in zones of high AOM than in peripheral sediments. AOM produces local microenvironments in which pH and dissolved silica concentrations are higher than elsewhere, and the resulting concentration gradient in dissolved silica allows diffusive transport from the zone of AOM towards the surrounding sediments, as well as towards and into already existing seep carbonate slabs. These slabs grow downward relative to the sediment-water interface SWI as a result from (i) carbonate precipitation within the zone of AOM and (ii) due to sedimentation and burial. As carbonate precipitates move downward, so does the zone of active AOM and with it the zone of where silica dissolution is facilitated by higher pH. Two schematic diagrams below (Figs. 54 & 55) illustrate the proposed scenario for the Siltstone of Shoalwater Bay deposits:

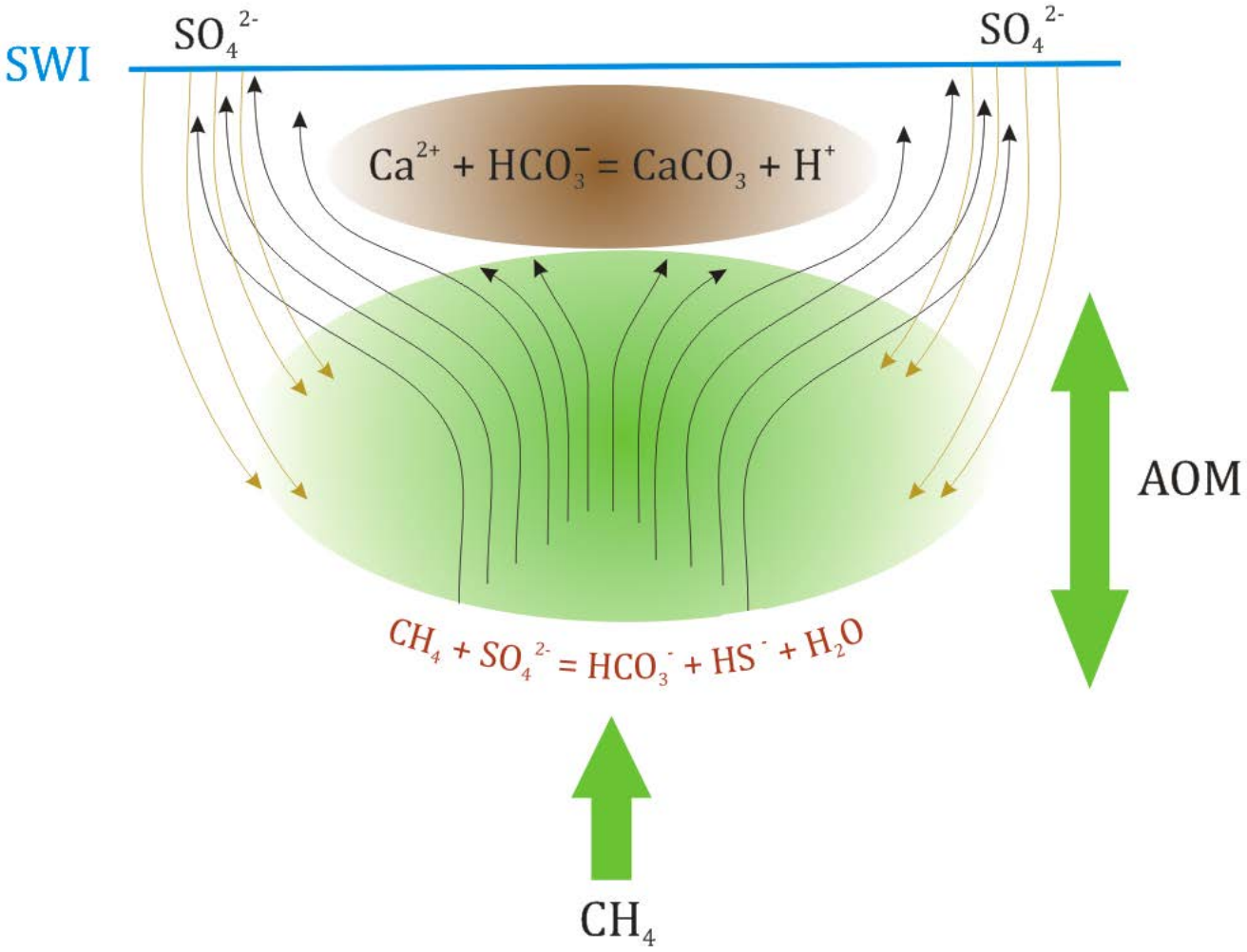

Figure 54: Schematic diagram of an ancient methane seep. Anaerobic oxidation of methane (AOM) induced precipitation of carbonates (brown ellipse) formed below the sediment-water interface (SWI). Green ellipse displays the influence of AOM radiating outwards from an AOM hotspot in the centre. Black arrows pointing upward indicate the direction of methane flux from below around the carbonate slab towards the SWI. Yellow arrows pointing downward indicate sulfate influx into the sediment from ocean bottom waters. Drawn by Smrzka and Zwicker.

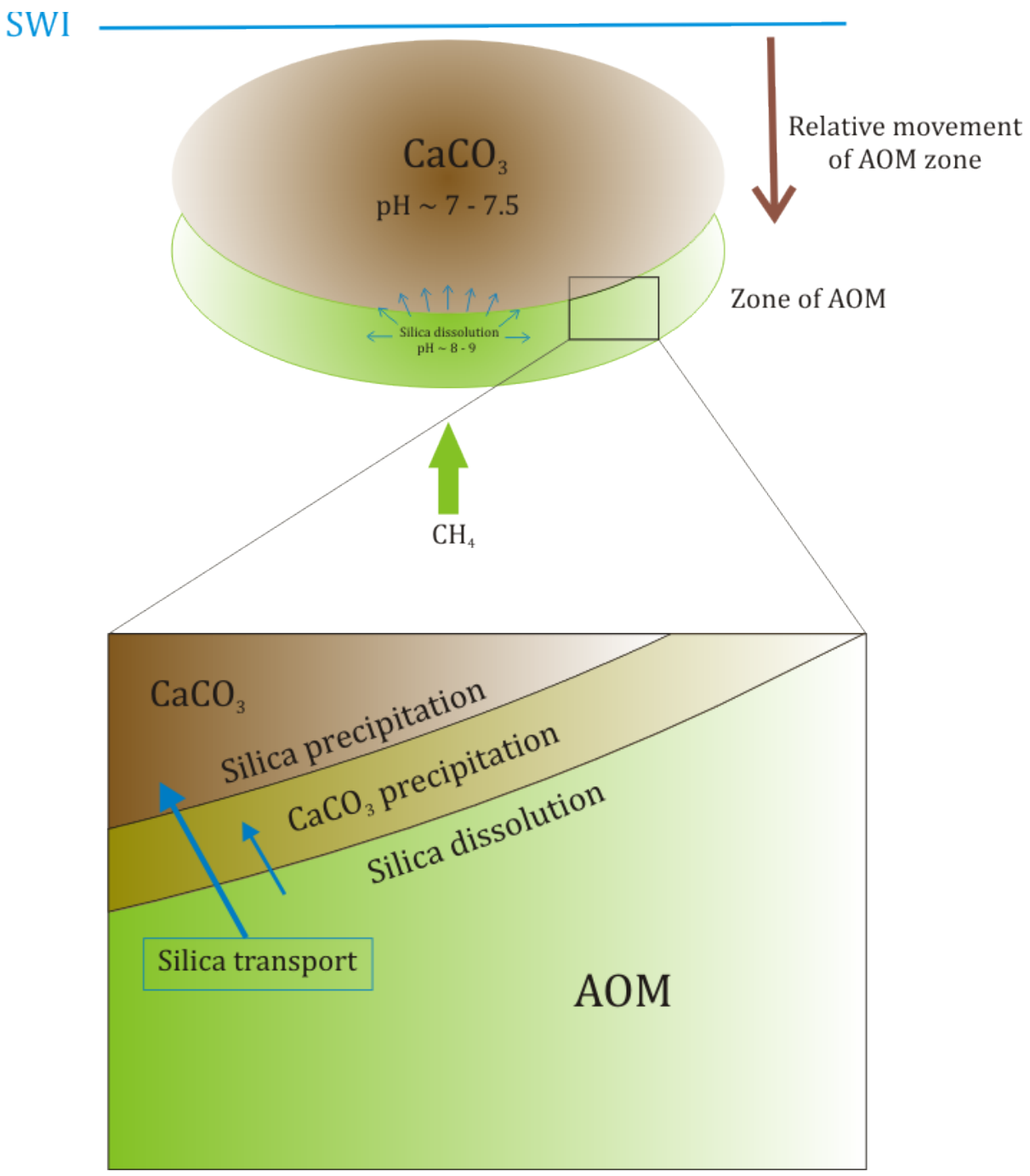

Figure 55: Schematic diagram showing a carbonate slab (brown ellipse) surrounded by a zone of active AOM around it (green zone). Precipitation leads to a relative downward movement of the AOM zone. Large rectangle shows processes in detail. Silica dissolution occurs within the AOM zone at higher pH, together with carbonate precipitation on the rim of the carbonate slab, causing a relative downward growth of the deposit (indicated by the brown arrow). Dissolved silica moves towards the carbonate slab and lower pH via diffusion as indicated by the blue arrows, and may occur simultaneously or after carbonate dissolution. Drawn by Smrzka and Zwicker.

Biogenic silica at Knappton – silica diagenesis

Petrographical evidence implies that silicification of samples occurred after cementation by AOM-related, early carbonate cements and, in most cases, before precipitation of the late equant calcite spar. This suggests that dissolved silica has been transported into already consolidated carbonate rocks and precipitated in response to (i) the dissolved silica concentration gradient and (ii) the pH gradient resulting from lower AOM rates in the surrounding sediments. The presence of silicified botryoids (Figs. 14 & 21) support the idea that pH was higher during carbonate cementation and precipitation, and lower during silicification as they clearly show an alteration of banded and botryoidal cement by silica. Such a scenario would require that a certain porosity was retained within the rock, enabling diffusive or even advective flow. In the case of the Willapa Bay deposits, where carbonate cementation is largely absent, silica often occurs directly after the primary micrite, filling pores completely.

Most marine sediments contain amorphous silica or opal-A (Williams et al., 1985). During early diagenesis, this primary phase is transformed into a less soluble cristobalite-tridymite phase (opal-CT; (Jones and Sengit, 1971)).

Thermodynamically, the most stable silica phase is quartz, which forms last (e.g. Murata and Norman, 1976; Fig. 56). These transformations occur via dissolution and reprecipitation reactions, which are dependent on solubility, surface area, ionic strength and the presence of detrital minerals in the sediment (Williams et al., 1985). From petrography alone it is difficult to evaluate the crystallography of the present silica phases at Knappton, and to determine to which part of the opal-A → opal-CT → quartz transition stage (Fig. 56) these silica minerals belong to. Furthermore, it is difficult to assess the influence of AOM on silica phase transition after its initial precipitation, since silica phase transformations occur just as well in non-seep sediments during advanced burial through subsequent dissolution and re-precipitation reactions (Hurd and Theyer, 1975; Kastner et al., 1977; Garrison et al., 1980). At the Siltstone of Shoalwater Bay deposit, it is most likely that the periodical advent and cessation of AOM over time additionally altered the silica phase transition after its initial dissolution by changing the geochemical environment. From petrographic observations alone, silica phases in Knappton and Willapa Bay deposits resemble granular cryptocrystalline to microcrystalline

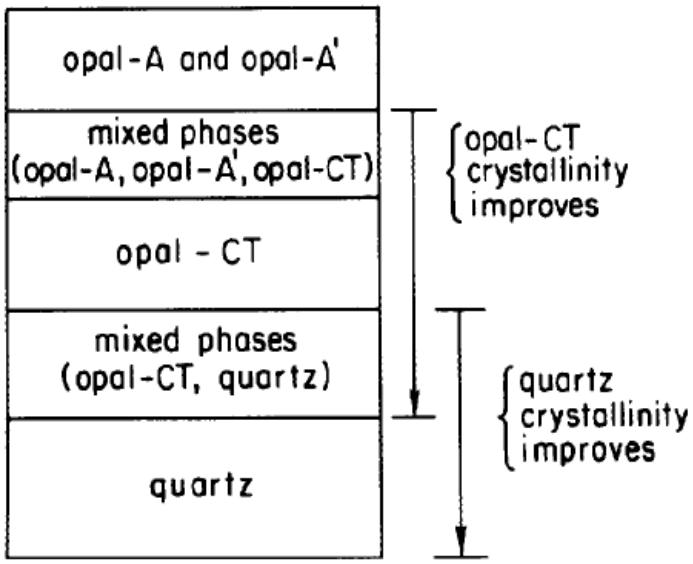

Figure 56: Schematic diagram of diagenetic zones in a sedimentary rock stratigraphic column that would theoretically results from diagenetic reactions predicted. Taken from Williams et al., 1985.

quartz. At the former deposit, there are additional clues regarding the paragenesis of authigenic silica phases: Oxygen isotope studies on silica minerals have stressed the importance of temperature on silica phase transitions in marine diagenesis (e.g. Knauth and Epstein, 1976; Murata et al., 1977; Knauth, 1994) and have enabled an estimation of ambient temperatures during silica precipitation: opal-A converts to opal-CT completely at ~45°C and quartz forms extensively at ~80°C (Kastner, 1981; Pisciotto, 1981; Knauth, 1994). Both localities of the Siltstone of Shoalwater Bay deposit have been studied for their lipid biomarker content, which is not included in this thesis. Hydrocarbon distribution of the Knappton samples indicate that the rocks were heated to temperatures within the oil window and perhaps beyond, as many *n*-alkanes and fatty acids are only partially preserved (data not shown). Finally, rocks containing carbonate minerals are known to promote the formation of quartz and increase transition rates from opal-CT (Greenwood, 1973; Kastner et al., 1977; Isaacs, 1982). Additionally, early quartz forms much quicker in clay-poor calcareous sediments than in clay-rich sediments (Von Rad et al., 1977; Robertson, 1977). Although the host sediments at Knappton and Willapa Bay were most likely clay-rich marine sediments, authigenesis of carbonates has altered the bulk composition towards calcite-rich sediments, favoring and accelerating the transition towards quartz. These details constrain temperatures of diagenetic silica alterations and influences of bulk sediment mineralogy, pointing towards the fact that most of the Knappton biogenic silica is indeed cryptocrystalline to microcrystalline quartz.

7.3 – Conclusions from geochemical modeling

The numerical batch-reaction and reaction-transport experiments lead to the following conclusions:

- Carbonate precipitation via AOM alone does not increase local pH of sedimentary porewaters
- Methane degassing and ebullition at active seeps enables CO_2-removal from porewaters, triggering a pH increase
- At cold seeps, pH is controlled by AOM rate, fluid flux, carbonate precipitation and CO_2 degassing
- Silica dissolution and precipitation reactions are controlled by pH, which is again dependent on the factors mentioned above
- Silica phases of Knappton and Willapa Bay deposits were produced by dissolution and re-precipitation reactions controlled by AOM, additionally influencing the diagenetic sequence of silica phases.

8 – Acknowledgments

Thanks are due to all who contributed to this work

Jörn Peckmann – For introducing me into the wondrous realm of marine sciences, for providing key literature, for his support during sample preparation and microscopy, for vital advice and guidance during the writing process and for the reading and correction of drafts. Finally, I greatly appreciate his time invested into this work, his constant, reliable support at all times and for being a great supervisor.

Stephan Krämer – For introducing me into geochemical modeling, for his advice and enthusiasm concerning PHREEQC, for his time spent on lively debates and discussions, and on inspections and corrections of drafts.

James Goedert – For providing rock samples, without which this work could not have been accomplished. Furthermore, I thank him for documents, photographs and recommendations crucial to this work.

David Fischer and **Sabine Kasten** – For sharing their collected data, which proved essential to geochemical modeling.

Daniel Birgel – For supportive discussions and suggestions regarding early diagenesis and biomarkers.

Sylvain Richoz – For collection and geochemical analyses of rock samples.

Thomas Pape – For advice, counsel and sharing of documents regarding CO_2 degassing.

Jennifer Zwicker – For development and graphical assistance of figures 54 and 55.

Leopold Slawek – For preparation of thin sections.

Christian Baal – For assistance with fluorescence microscopy.

9 – Appendix

This appendix lists all data calculated for the various numerical experiments described in the "materials and methods" and "geochemical modeling" chapters, where descriptions and setups of each experiment are specified.

9.1 – Batch reaction calculations

Numerical experiment 1

step	pH	Alkalinity [moles / kgw]	Ionic strength	Ca [moles / kgw]	Calcite in phase assemblage [moles / kgw]	Calcite precipitated [moles / kgw]
1	7.37748	0.00596185	0.706517	9.4601e-03	7.2267e-01	2.7087e-04
2	7.34714	0.00706535	0.70725	9.1672e-03	7.2296e-01	2.9297e-04
3	7.32323	0.00813817	0.707947	8.8589e-03	7.2327e-01	3.0826e-04
4	7.30425	0.00919047	0.708619	8.5404e-03	7.2359e-01	3.1849e-04
5	7.28919	0.0102301	0.709276	8.2156e-03	7.2392e-01	3.2479e-04
6	7.27733	0.0112633	0.709925	7.8877e-03	7.2424e-01	3.2796e-04
7	7.26816	0.0122952	0.710573	7.5591e-03	7.2457e-01	3.2857e-04
8	7.26126	0.01333	0.711224	7.2320e-03	7.2490e-01	3.2705e-04
9	7.25632	0.0143714	0.711884	6.9083e-03	7.2522e-01	3.2373e-04
10	7.2531	0.0154224	0.0154224	6.5894e-03	0.712556	3.1888e-04
11	7.25141	0.0164856	0.713243	6.2767e-03	7.2585e-01	3.1271e-04
12	7.25106	0.0175633	0.713948	5.9713e-03	7.2616e-01	3.0541e-04
13	7.25192	0.0186574	0.714673	5.6741e-03	7.2646e-01	2.9715e-04
14	7.25387	0.0197696	0.715421	5.3861e-03	7.2674e-01	2.8807e-04
15	7.2568	0.291506	0.0209011	0.716192	5.1077e-03	7.2702e-01
16	7.26061	0.0220531	0.716988	4.8397e-03	7.2729e-01	2.6803e-04
17	7.26522	0.0232263	0.717811	4.5824e-03	7.2755e-01	2.5733e-04
18	7.27054	0.0244214	0.71866	4.3361e-03	7.2779e-01	2.4632e-04

19	7.27651	0.0256387	0.719537	4.1009e-03	7.2803e-01	2.3513e-04
20	7.28304	0.0268784	0.720441	3.8771e-03	7.2825e-01	2.2386e-04

Table 12: AOM in a sediment column; total time = 1 month

step	pH	Alkalinity [moles / kgw]	Ionic strength	Ca [moles / kgw]	Calcite in phase assemblage [moles / kgw]	Calcite precipitated [moles / kgw]
1	7.25113	0.0177692	0.714084	5.9143e-03	7.2622e-01	3.8166e-03
2	7.31683	0.0325656	0.724716	3.0273e-03	7.2910e-01	2.8870e-03
3	7.42839	0.0502179	0.738845	1.5822e-03	7.3055e-01	1.4452e-03
4	7.5323	0.06942	0.06942	9.2795e-04	0.754875	6.5425e-04
5	7.61791	0.089259	0.771701	6.0808e-04	7.3152e-01	3.1987e-04
6	7.68717	0.109358	0.78887	4.3355e-04	7.3170e-01	1.7454e-04
7	7.74362	0.129567	0.806204	3.2891e-04	7.3180e-01	1.0464e-04
8	7.79018	0.149821	0.823626	2.6138e-04	7.3187e-01	6.7539e-05
9	7.82907	0.17009	0.841101	2.1520e-04	7.3192e-01	4.6181e-05
10	7.86192	0.190358	0.858612	1.8215e-04	7.3195e-01	3.3051e-05
11	7.88994	0.210618	0.876146	1.5761e-04	7.3197e-01	2.4540e-05
12	7.91405	0.230865	0.893699	1.3883e-04	7.3199e-01	1.8778e-05
13	7.93495	0.251096	0.911266	1.2410e-04	7.3201e-01	1.4733e-05
14	7.9532	0.27131	0.27131	1.1229e-04	0.928843	1.1229e-04
15	7.96923	0.291506	0.946428	1.0266e-04	7.3203e-01	9.6319e-06
16	7.98338	0.311685	0.96402	9.4680e-05	7.3204e-01	7.9811e-06
17	7.99592	0.331847	0.981616	8.7977e-05	7.3204e-01	6.7028e-06
18	8.0071	0.351992	0.999214	8.2281e-05	7.3205e-01	5.6961e-06
19	8.01709	0.372121	1.01681	7.7390e-05	7.3205e-01	4.8911e-06
20	8.02605	0.392234	1.03441	7.3152e-05	7.3206e-01	4.2389e-06

Table 13: AOM in a sediment column; total time = 1 year

Numerical experiment 2

All units in moles/kgw except pH and ionic strength (mu), time period = 1 month

step	pH	Alkalinity [moles / kgw]	Ionic strength	Ca [moles / kgw]	Calcite in phase assemblage [moles / kgw]	Calcite precipitated [moles / kgw]
1	7.36577	0.00593689	0.706723	9.7586e-03	7.2268e-01	2.8336e-04
2	7.32446	0.00699449	0.707637	9.7536e-03	7.2300e-01	3.1592e-04
3	7.29002	0.00800061	0.708489	9.7230e-03	7.2334e-01	3.4164e-04
4	7.2608	0.00896543	0.00896543	0.70929	9.6717e-03	7.2370e-01
5	7.23565	0.00989675	0.71005	9.6036e-03	7.2408e-01	3.7898e-04
6	7.21377	0.0108007	0.710777	9.5219e-03	7.2447e-01	3.9266e-04
7	7.19456	0.011682	0.711476	9.4290e-03	7.2488e-01	4.0392e-04
8	7.17758	0.0125447	0.712153	9.3267e-03	7.2529e-01	4.1321e-04
9	7.16247	0.0133921	0.712811	9.2168e-03	7.2571e-01	4.2089e-04
10	7.14897	0.0142267	0.713453	9.1005e-03	7.2614e-01	4.2722e-04
11	7.13685	0.0150508	0.714083	8.9790e-03	7.2657e-01	4.3243e-04
12	7.12593	0.0158664	0.714702	8.8533e-03	7.2701e-01	4.3667e-04
13	7.11608	0.0166752	0.715313	8.7242e-03	7.2745e-01	4.4009e-04
14	7.10716	0.0174784	0.715917	8.5923e-03	7.2789e-01	4.4280e-04
15	7.09909	0.0182775	0.716517	8.4584e-03	7.2834e-01	4.4488e-04
16	7.09176	0.0190734	0.717112	8.3229e-03	7.2878e-01	4.4643e-04
17	7.0851	0.0198672	0.0198672	0.717705	8.1864e-03	7.2923e-01
18	7.07905	0.0206596	0.718297	8.0492e-03	7.2968e-01	4.4815e-04
19	7.07356	0.0214513	0.718888	7.9117e-03	7.3013e-01	4.4843e-04
20	7.06857	0.0222432	0.719479	7.7743e-03	7.3058e-01	4.4837e-04

Table 14: AOM with stoichiometric Ca^{2+} addition; total time = 1 month

step	pH	Alkalinity [moles / kgw]	Ionic strength	Ca [moles / kgw]	Calcite in phase assemblage [moles / kgw]	Calcite precipitated [moles / kgw]
1	7.12399	0.01602	0.714818	8.8291e-03	7.2709e-01	4.6922e-03
2	7.05168	0.0257243	0.722084	7.1798e-03	7.3253e-01	5.4396e-03
3	7.03216	0.0357242	0.729729	5.6827e-03	7.3782e-01	5.2876e-03
4	7.0332	0.0463507	0.0463507	4.5040e-03	0.738157	4.9691e-03
5	7.0423	0.0575706	0.0575706	3.6278e-03	0.747331	4.6665e-03
6	7.05382	0.0692488	0.757083	2.9871e-03	7.5189e-01	4.4312e-03
7	7.06532	0.0812523	0.767252	2.5154e-03	7.5615e-01	4.2621e-03
8	7.07582	0.0934797	0.777714	2.1622e-03	7.6029e-01	4.1436e-03
9	7.08506	0.105861	0.788382	1.8920e-03	7.6435e-01	4.0606e-03
10	7.09304	0.118347	0.799197	1.6810e-03	7.6835e-01	4.0014e-03
11	7.09987	0.130907	0.810119	1.5128e-03	7.7231e-01	3.9586e-03
12	7.10569	0.143517	0.821121	1.3764e-03	7.7624e-01	3.9268e-03
13	7.11064	0.156164	0.832183	1.2640e-03	7.8014e-01	3.9028e-03
14	7.11483	0.168836	0.843291	1.1700e-03	7.8403e-01	3.8844e-03
15	7.11838	0.181525	0.854436	1.0904e-03	7.8790e-01	3.8700e-03
16	7.12138	0.194226	0.865609	1.0224e-03	7.9175e-01	3.8585e-03
17	7.1239	0.206934	0.206934	9.6350e-04	0.876805	3.8493e-03
18	7.12602	0.219646	0.88802	9.1219e-04	7.9945e-01	3.8417e-03
19	7.12777	0.23236	0.89925	8.6710e-04	8.0328e-01	3.8355e-03
20	7.12921	0.245074	0.910492	8.2719e-04	8.0711e-01	3.8303e-03

Table 15: AOM with stoichiometric Ca^{2+} addition; total time = 1 year

Numerical experiment 3

All units in moles/kgw except pH and ionic strength (mu)

step	pH	Alkalinity [moles / kgw]	Ionic strength	Ca [moles / kgw]	Calcite in phase assemblage [moles / kgw]	Calcite precipitated [moles / kgw]
1	7.36702	0.0140548	0.713063	7.8453e-03	7.2808e-01	5.6757e-03
2	7.42995	0.0231439	0.720408	5.8860e-03	7.3383e-01	5.7495e-03
3	7.49747	0.0330242	0.728772	4.3250e-03	7.3918e-01	5.3512e-03
4	7.56741	0.0436572	0.738095	3.1440e-03	7.4415e-01	4.9714e-03
5	7.63704	0.0549354	0.74823	2.2896e-03	7.4879e-01	4.6448e-03
6	7.70389	0.0667131	0.758984	1.6895e-03	7.5318e-01	4.3906e-03
7	7.76636	0.0788473	0.770173	1.2725e-03	7.5739e-01	4.2075e-03
8	7.82378	0.0912233	0.781653	9.8124e-04	7.6147e-01	4.0817e-03
9	7.87612	0.103759	0.793321	7.7470e-04	7.6547e-01	3.9970e-03
10	7.92372	0.116399	0.805111	6.2525e-04	7.6941e-01	3.9399e-03
11	7.96705	0.129108	0.816978	5.1471e-04	7.7331e-01	3.9010e-03
12	8.0066	0.141862	0.141862	0.828896	4.3119e-04	7.7718e-01
13	8.04285	0.154645	0.840845	3.6680e-04	7.8104e-01	3.8548e-03
14	8.07619	0.167446	0.852816	3.1624e-04	7.8488e-01	3.8410e-03
15	8.107	0.18026	0.18026	2.7586e-04	0.864799	3.8308e-03
16	8.13557	0.19308	0.876789	2.4314e-04	7.9253e-01	3.8231e-03
17	8.16217	0.205904	0.888784	2.1626e-04	7.9635e-01	3.8173e-03
18	8.18702	0.218729	0.90078	1.9391e-04	8.0016e-01	3.8128e-03
19	8.21031	0.231553	0.912776	1.7513e-04	8.0397e-01	3.8092e-03
20	8.2322	0.244375	0.244375	1.5918e-04	0.92477	3.8064e-03

Table 16: AOM with stoichiometric Ca^{2+} addition and CO2 degassing; total time = 1 year

Numerical experiment 4

All units in moles/kgw except pH and ionic strength (mu)

step	pH	Alkalinity [moles / kgw]	Ionic strength	Si [moles / kgw]	Amorphous silica in phase assemblage [moles / kgw]	Amorphous silica precipitated [moles / kgw]
1	7.36699	0.0140575	0.713094	1.1260e-03	2.6350e+00	3.1047e-06
2	7.42991	0.0231469	0.720438	1.1237e-03	2.6350e+00	2.2061e-06
3	7.49741	0.0330275	0.728803	1.1213e-03	2.6350e+00	2.3645e-06
4	7.56734	0.0436608	0.738127	1.1187e-03	2.6350e+00	2.4975e-06
5	7.63696	0.0549392	0.748262	1.1160e-03	2.6350e+00	2.5953e-06
6	7.70379	0.0667171	0.759016	1.1133e-03	2.6350e+00	2.6584e-06
7	7.76626	0.0788515	0.770206	1.1105e-03	2.6350e+00	2.6947e-06
8	7.82367	0.0912279	0.781686	1.1077e-03	2.6350e+00	2.7141e-06
9	7.876	0.103764	0.103764	1.1049e-03	0.793354	2.7242e-06
10	7.9236	0.116405	0.116405	1.1021e-03	0.805144	2.7298e-06
11	7.96692	0.129114	0.817012	1.0993e-03	2.6350e+00	2.7334e-06
12	8.00647	0.141868	0.82893	1.0965e-03	2.6350e+00	2.7364e-06
13	8.04272	0.154651	0.84088	1.0937e-03	2.6350e+00	2.7393e-06
14	8.07606	0.167453	0.852851	1.0909e-03	2.6350e+00	2.7423e-06
15	8.10686	0.180267	0.864835	1.0880e-03	2.6350e+00	2.7455e-06
16	8.13543	0.193088	0.876826	1.0852e-03	2.6350e+00	2.7488e-06
17	8.16203	0.205912	0.888821	1.0824e-03	2.6350e+00	2.7523e-06
18	8.18688	0.218738	0.900818	1.0796e-03	2.6350e+00	2.7558e-06
19	8.21017	0.231562	0.912814	1.0767e-03	2.6351e+00	2.7593e-06
20	8.23207	0.244385	0.92481	1.0739e-03	2.6351e+00	2.7627e-06

Table 17: AOM with stoichiometric Ca^{2+} addition and CO_2 degassing and heterogeneous reactions with amorphous silica; total time = 1 year

step	pH	Alkalinity [moles / kgw]	Ionic strength	Si [moles / kgw]	Quartz in phase assemblage [moles / kgw]	Quartz precipitated [moles / kgw]
1	7.36702	0.0140548	0.713063	4.7122e-05	2.6350e+00	1.3013e-07
2	7.42995	0.0231439	0.720408	4.7026e-05	2.6350e+00	9.2326e-08
3	7.49747	0.0330242	0.728772	4.6924e-05	2.6350e+00	9.8951e-08
4	7.56741	0.0436572	0.738095	4.6816e-05	2.6350e+00	1.0451e-07
5	7.63704	0.0549354	0.74823	4.6704e-05	2.6350e+00	1.0861e-07
6	7.70389	0.0667131	0.758984	4.6590e-05	2.6350e+00	1.1124e-07
7	7.76636	0.0788473	0.770174	4.6474e-05	2.6350e+00	1.1276e-07
8	7.82378	0.0912234	0.781653	4.6357e-05	2.6350e+00	1.1357e-07
9	7.87612	0.103759	0.793321	4.6240e-05	2.6350e+00	1.1399e-07
10	7.92372	0.116399	0.805111	4.6122e-05	2.6350e+00	1.1423e-07
11	7.96705	0.129108	0.816978	4.6005e-05	2.6350e+00	1.1438e-07
12	8.0066	0.141862	0.141862	4.5887e-05	0.828896	4.5887e-05
13	8.04285	0.154645	0.840845	4.5769e-05	2.6350e+00	1.1463e-07
14	8.07619	0.167446	0.852816	4.5651e-05	2.6350e+00	1.1475e-07
15	8.107	0.18026	0.18026	4.5533e-05	0.864799	1.1489e-07
16	8.13557	0.19308	0.876789	4.5415e-05	2.6350e+00	1.1503e-07
17	8.16217	0.205904	0.888784	4.5297e-05	2.6350e+00	1.1517e-07
18	8.18702	0.218729	0.90078	4.5178e-05	2.6350e+00	1.1532e-07
19	8.2103	0.231553	0.231553	4.5060e-05	0.912776	4.5060e-05
20	8.2322	0.244375	0.244375	0.92477	4.4941e-05	2.6350e+00

Table 18: AOM with stoichiometric Ca^{2+} addition and CO_2 degassing and heterogeneous reactions with quartz; total time = 1 year

9.2 – Reaction – transport experiments

Numerical experiment 5

Time [s]	pH	Ca in solution [moles / kgw]	Calcite in phase assemblage [moles / kgw]	Calcite precipitated [moles / kgw]
0	7.65508	1.0672e-02	7.2251e-01	1.0672e-02
3.4344e+07	7.48205	1.3192e-03	7.7797e-01	9.0175e-03
6.8688e+07	7.60981	6.9068e-04	8.3286e-01	9.7946e-03
1.03032e+08	7.7825	2.9481e-04	2.9481e-04	8.9404e-01
1.37376e+08	7.94823	1.2586e-04	9.5855e-01	1.0916e-02
1.7172e+08	7.99307	9.8084e-05	1.0242e+00	1.0960e-02
2.06064e+08	8.12214	3.6445e-05	1.0904e+00	1.1059e-02
2.40408e+08	8.09372	2.5785e-05	1.1569e+00	1.1077e-02
2.74752e+08	8.09372	2.5785e-05	1.2233e+00	1.1077e-02
3.09096e+08	7.34113	3.0130e-03	1.2704e+00	5.8570e-03
3.4344e+08	7.33753	3.0927e-03	1.3049e+00	5.6999e-03
3.77784e+08	7.33466	3.1590e-03	1.3384e+00	5.5691e-03

Table 19: Reactive transport; effect of changing AOM rates over 12 years without CO_2 degassing

Time [s]	pH	Ca in solution [moles / kgw]	Calcite in phase assemblage [moles / kgw]	Calcite precipitated [moles / kgw]
0	7.65508	7.65508	7.2251e-01	1.0672e-02
3.4344e+07	7.90666	6.3599e-04	7.8499e-01	1.0113e-02
6.8688e+07	8.09126	2.8039e-04	8.4611e-01	1.0559e-02
1.03032e+08	8.32188	1.0407e-04	9.1063e-01	1.0966e-02
1.37376e+08	8.56218	3.9805e-05	9.7654e-01	1.1054e-02
1.7172e+08	8.6388	3.0013e-05	3.0013e-05	1.0429e+00
2.06064e+08	9.0225	9.2754e-06	9.2754e-06	1.1095e+00
2.40408e+08	9.25132	5.1793e-06	1.1762e+00	1.1111e-02
2.74752e+08	9.25132	5.1793e-06	1.2428e+00	1.1111e-02
3.09096e+08	7.64819	2.0408e-03	1.2959e+00	7.3991e-03
3.4344e+08	7.63981	2.1200e-03	1.3395e+00	7.2352e-03
3.77784e+08	7.633	2.1865e-03	2.1865e-03	1.3822e+00

Table 20: Reactive transport; effect of changing AOM rates over 12 years with CO_2 degassing

Numerical experiment 6

Time [s]	pH	Calcite in phase assemblage [moles / kgw]	Calcite precipitated [moles / kgw]
0	7.65508	7.2251e-01	1.0597e-04
3.4344e+07	7.90666	7.8499e-01	1.0113e-02
6.8688e+07	8.09126	8.4611e-01	1.0559e-02
1.03032e+08	8.32188	9.1063e-01	1.0966e-02
1.37376e+08	8.56218	9.7654e-01	1.1054e-02
1.7172e+08	8.6388	1.0429e+00	1.0429e+00
2.06064e+08	9.0225	1.1095e+00	1.1095e+00
2.40408e+08	9.25132	1.1762e+00	1.1111e-02
2.74752e+08	9.25132	1.2428e+00	1.1111e-02
3.09096e+08	7.64819	1.2959e+00	7.3991e-03
3.4344e+08	7.63981	1.3395e+00	7.2352e-03
3.77784e+08	7.633	1.3822e+00	1.3822e+00

Table 21: Fluid flux rate = 0.16 cm/d

Time [s]	pH	Calcite in phase assemblage [moles / kgw]	Calcite precipitated [moles / kgw]
0	7.65508	7.2251e-01	1.0597e-04
3.4344e+07	7.9772	7.7065e-01	7.7065e-01
6.8688e+07	8.18943	8.1664e-01	1.5576e-02
1.03032e+08	8.47635	8.6444e-01	1.6051e-02
1.37376e+08	8.72229	9.1287e-01	1.6199e-02
1.7172e+08	8.79764	9.6146e-01	1.6204e-02
2.06064e+08	9.14402	1.0101e+00	1.6229e-02
2.40408e+08	9.36834	1.0588e+00	1.6237e-02
2.74752e+08	9.36834	1.1076e+00	1.6237e-02
3.09096e+08	7.56919	1.1459e+00	9.6713e-03
3.4344e+08	7.55612	1.1740e+00	9.2774e-03
3.77784e+08	7.54562	1.2010e+00	8.9450e-03

Table 22: Fluid flux rate = 0.08 cm/d

Numerical experiment 7

Time [s]	pH	Dissolved silica in solution [moles/kgw]	Biogenic silica in phase assemblage [moles/kgw]	Biogenic silica dissolved [moles/kgw]
0	7.65508	1,03E-04	2,63E+00	0
3.4344e+07	7.90848	1,13E-03	2,63E+00	1,42E-03
6.8688e+07	8.09319	1,13E-03	2,62E+00	1,42E-03
1.03032e+08	8.32408	1,28E-03	2,61E+00	1,69E-03
1.37376e+08	8.5642	1,30E-03	2,60E+00	1,83E-03
1.7172e+08	8.64096	1,41E-03	2,59E+00	1,95E-03
2.06064e+08	9.02408	1,58E-03	2,57E+00	2,26E-03
2.40408e+08	9.25223	1,70E-03	2,56E+00	2,52E-03
2.74752e+08	9.25223	1,70E-03	2,54E+00	2,52E-03
3.09096e+08	7.64944	1,13E-03	2,53E+00	1,32E-03
3.4344e+08	7.64103	1,13E-03	2,53E+00	1,32E-03
3.77784e+08	7.6342	1,13E-03	2,52E+00	1,32E-03

Table 23: Reactive transport; effect of changing AOM rates over 12 years with and without CO_2 degassing and heterogeneous reactions with biogenic silica and CO_2 degassing.

Time [s]	pH	Dissolved silica in solution [moles/kgw]	Biogenic silica in phase assemblage [moles/kgw]	Biogenic silica dissolved [moles/kgw]
0	7,65508	1,03E-04	2,635E+00	0
3.4344e+07	7,48418	9,65E-04	2,63E+00	1,12E-03
6.8688e+07	7,61244	9,75E-04	2,62E+00	1,13E-03
1.03032e+08	7,78631	1,08E-03	2,61E+00	1,35E-03
1.37376e+08	7,95253	1,11E-03	2,61E+00	1,39E-03
1.7172e+08	7,9973	1,12E-03	2,60E+00	1,44E-03
2.06064e+08	8,12497	1,27E-03	2,59E+00	1,68E-03
2.40408e+08	8,09505	1,30E-03	2,58E+00	1,72E-03
2.74752e+08	8,09505	1,30E-03	2,57E+00	1,72E-03
3.09096e+08	7,34282	9,65E-04	2,56E+00	1,12E-03
3.4344e+08	7,33921	9,65E-04	2,55E+00	1,12E-03
3.77784e+08	7,33633	9,65E-04	2,55E+00	1,12E-03

Table 24: Reactive transport; effect of changing AOM rates over 12 years with and without CO_2 degassing and heterogeneous reactions with biogenic silica and without CO_2 degassing.

9 – References

Aharon P. and Fu B., 2000. Microbial sulfate reduction rates and sulfur and oxygen isotope fractionations at oil and gas seeps in deepwater Gulf of Mexico. *Geochimica et Cosmochimica Acta* **64**, pp. 233–246.

Aloisi G., Pierre C., Rouchy J.-M., Foucher J.-P. and Woodside J., 2000. Methane-related authigenic carbonates of Eastern Mediterranean Sea mud volcanoes and their possible relation to gas hydrate destabilisation. *Earth and Planetary Science Letters* **184**, pp. 321–338.

Bacon M. P., Brewer P. G., Spemcer D. W., Murray J. W. and Goddard J., 1980. Lead - 210, polonium . 201, manangese and iron in the Cariaco Trench. *Deep Sea Research Part A, Oceanographic Research Papers* **27**, pp. 119–135.

Bacon M. P. P. and Edmond J. M. M., 1972. Barium at Geosecs III in the southwest Pacific. *Earth and Planetary Science Letters* **16**, pp. 66–74.

Baker P. A. and Burns S. J., 1985. Occurrence and formation of dolomite in organic-rich continental margin sediments. *Bulletin, American Association of Petroleum Geologists* **69**, pp. 1917–1930.

Barnes R. O. and Goldberg E. D., 1976. Methane production and consumption in anoxic marine sediments. *Geology* **4**, pp. 297–300.

Bathurst R. G. C., 1975. *Carbonate sediments and their diagenesis*. 2nd ed., Elsevier, Amsterdam, pp. 658.

Beal E. J., House C. H. and Orphan V. J., 2009. Manganese- and iron-dependent marine methane oxidation. *Science* **325**, pp. 184–187.

Beauchamp B. and Von Bitter P., 1992. Annual meeting of the geological association of Canada on hydrothermal vent - cold seep chemosynthetic communities. Geological processes and their products from modern and ancient times. Vancouver, British Columbia, Canada, May, 1990. *Palaios* **7**, pp. 338–484.

Beauchamp B. and Savard M., 1992. Cretaceous chemosynthetic carbonate mounds in the Canadian Arctic. *Palaios* **7**, pp. 434–450.

Beck L., Gehlen M., Flank A.-M., Van Bennekom A. J. and Van Beusekom J. E. E., 2002. The relationship between Al and Si in biogenic silica as determined by PIXE and XAS. *Nuclear Instruments and Methods in Physics Research, Section B: Beam Interactions with Materials and Atoms* **189**, pp. 180–184.

Berger W. H., Smetacek V. and Wefer G., eds. 1989. *Prodictivity of the ocean: Past and present.*, Wiley, Chichester.

Berner R. A., 1970. Sedimentary pyrite formation. *American Journal of Science* **268**, pp. 1–23.

Berner R. A., 1984. Sedimentary pyrite formation: An update. *Geochimica et Cosmochimica Acta* **48**, pp. 605–615.

Boetius A., Ravenschlag K., Schubert C. J., Rickert D., Widdel F., Gleseke A., Amann R., Jørgensen B B, Witte U. and Pfannkuche O., 2000. A marine microbial consortium apparently mediating anaerobic oxidation methane. *Nature* **407**, pp. 623–626.

Bohrmann G., Greinert J., Suess E. and Torres M., 1998. Authigenic carbonates from the Cascadia subduction zone and their relation to gas hydrate stability. *Geology* **26**, pp. 647–650.

Bots P., Benning L. G., Rickaby R. E. M. and Shaw S., 2011. The role of SO4 in the switch from calcite to aragonite seas. *Geology* **39**, pp. 331–334.

Boudreau B. P., 1996. A method-of-lines code for carbon and nutrient diagenesis in aquatic sediments. *Computers and Geosciences* **22**, pp. 479–496.

Boudreau B. P. and Canfield D. E., 1988. A provisional diagenetic model for pH in anoxic porewaters: application to the FOAM Site. *Journal of Marine Research* **46**, pp. 429–455.

Bradshaw A. L., Brewer P. G., Shafer D. K. and Williams R. T., 1981. Measurements of total carbon dioxide and alkalinity by potentiometric titration in the (GEOSECS) program. *Earth and Planetary Science Letters* **55**, pp. 99–115.

Brady P. V and Walther J. V, 1990. Kinetics of quartz dissolution at low temperatures. *Chemical Geology* **82**, pp. 253–264.

Brandon M. T. and Calderwood A. R., 1990. High-pressure metamorphism and uplift of the Olympic subduction complex. *Geology* **18**, pp. 1252–1255.

Burton E. A., 1993. Controls on marine carbonate cement mineralogy: review and reassessment. *Chemical Geology* **105**, pp. 163–179.

Burton E. A. and Walter L. M., 1991. he effects of pCO2 and temperature on magnesium incorporation in calcite in seawater and MgCl2-CaCl2 solutions. *Geochimica et Cosmochimica Acta* **55**, pp. 777–785.

Butler I. B. and Rickard D., 2000. Framboidal pyrite formation via the oxidation of iron (II) monosulfide by hydrogen sulphide. *Geochimica et Cosmochimica Acta* **64**, pp. 2665–2672.

Campbell K. A., 2006. Hydrocarbon seep and hydrothermal vent paleoenvironments and paleontology: Past developments and future research directions. *Palaeogeography, Palaeoclimatology, Palaeoecology* **232**, pp. 362–407.

Campbell K. A., Farmer J. D. and Des Marais D., 2002. Ancient hydrocarbon seeps from the Mesozoic convergent margin of California: Carbonate geochemistry, fluids and paleoenvironments. *Geofluids* **2**, pp. 63–94.

Canfield D. E., Raiswell R. and Bottrell S., 1992. The reactivity of sedimentary iron minerals toward sulfide. *American Journal of Science* **292**, pp. 659–683.

Claypool G. E. and Kaplan I. R., 1974. The origin and distribution of methane in marine sediments. In *Natural gases in marine sediments* (ed. I. R. Kaplan).

Claypool G. E. and Kvenvolden K. A., 1983. Methane and other hydrocarbon gases in marine sediment. *Annual Review of Earth and Planetary Sciences* **11**, pp. 299–327.

Coleman M. L., 1985. Geochemistry of diagenetic non-silicate minerals: kinetic considerations. *Philosophical Transactions of the Royal Society of London*, pp. 1531.

Coleman M. L. and Raiswell R., 1995. Source of carbonate and origin of zonation in pyritiferous carbonate concretions: evaluation of a dynamic model. *American Journal of Science* **295**, pp. 282–308.

Crerar D. A. and Dove P. M., 1990. Kinetics of quartz dissolution in electrolyte solutions using a hydrothermal mixed flow reactor. *Chemical Geology* **84**, pp. 301–304.

Culkin and Cox, 1966. Sodium, potassium, magnesium, calcium and strontium in sea water. *Deep-Sea Research* **13**.

Curtis C. D., 1977. Sedimentary geochemistry: environments and processes dominated by involvement of an aqueous phase. *Philosophical Transactions of the Royal Society of London* **286a**, pp. 353–372.

Dale A.W., Regnier P., Knab N. J., Jørgensen B.B. and Van Cappellen P., 2008. Anaerobic oxidation of methane (AOM) in marine sediments from the Skagerrak (Denmark): II. Reaction-transport modeling. *Geochimica et Cosmochimica Acta* **72**, pp. 2880–2894.

Davis K. J., Dove P M and De Yoreo J. J., 2000. The role of Mg2+ as an impurity in calcite growth. *Science* **290**, pp. 1134–1137.

DeMaster D. J., 2002. The accumulation and cycling of biogenic silica in the Southern Ocean: revisiting the marine silica budget. *Deep-Sea Research Part II* **49**, pp. 3155–3167.

Devol A. H. and Ahmed S. I., 1981. Are high rates of sulphate reduction associated with anaerobic oxidation of methane? *Nature* **291**, pp. 407–408.

Devol A. H., Anderson J. J., Kuivila K. and Murray J. W., 1984. A model for coupled sulfate reduction and methane oxidation in the sediments of Saanich Inlet. *Geochimica et Cosmochimica Acta* **48**, pp. 993–1004.

Dixit S. and Van Cappellen P., 2002. Surface chemistry and reactivity of biogenic silica. *Geochimica et Cosmochimica Acta* **66**, pp. 2559–2568.

Dixit S., Van Cappellen P. and Van Bennekom A. J., 2001. Processes controlling solubility of biogenic silica and pore water build-up of silicic acid in marine sediments. *Marine Chemistry* **73**, pp. 333–352.

Dove P. M., 1999. The dissolution kinetics of quartz in aqueous mixed cation solutions. *Geochimica et Cosmochimica Acta* **63**, pp. 3715–3727.

Dove P. M. and Elston S. F., 1992. Dissolution kinetics of quartz in sodium chloride solutions: Analysis of existing data and a rate model for 25°C. *Geochimica et Cosmochimica Acta* **56**, pp. 4147–4156.

Dove P. M. and Rimstidt J. D., 1994. Silica - water interactions. In *Reviews in Mineralogy vol. 29: Silica - Physical behavior, geochemistry and materials applications* (eds. P. J. Heaney, C. Prewitt, and G. V Gibbs). Mineralogical Society of America, Washington D.C., pp. 259–308.

Dove P. M., 1994. The dissolution kinetics of quartz in sodium chloride solutions at 25° to (300°C). *American Journal of Science* **294**, pp. 665–712.

Edmond J. M., 1974. On the dissolution of carbonate and silicate in the deep ocean. *Deep-Sea Research and Oceanographic Abstracts* **21**, pp. 455–480.

Elvert M., Suess E. and Whiticar M. J., 1999. Anaerobic methane oxidation associated with marine gas hydrates: Superlight C-isotopes from saturated and unsaturated C20 and C25 irregular isoprenoids. *Naturwissenschaften* **86**, pp. 295–300.

Emerson S. and Hedges J. I., 1988. Processes controlling the organic matter content of open ocean sediments. *Paleoceanography* **3**, pp. 621–634.

Fleming B. A., 1986. Kinetics of reaction between silicic acid and amorphous silica surfaces in NaCl solutions. *Journal of Colloid And Interface Science* **110**, pp. 40–64.

Flügel E., 1982. *Microfacies analysis of limestones.* Springer-Verlag Berlin Heidelberg, pp. 652.

Flügel E., 2004. *Microfacies of carbonate rocks.* Springer-Verlag Berlin Heidelberg, pp. 1007.

Fraysse F., Pokrovsky O. S., Schott J. and Meunier J.-D., 2006. Surface properties, solubility and dissolution kinetics of bamboo phytoliths. *Geochimica et Cosmochimica Acta* **70**, pp. 1939–1951.

Froelich P. N., Klinkhammer G. P., Bender M. L., Luedtke N. A., Heath G. R., Cullen D., Dauphin P., Hammond D., Hartman B. and Maynard V., 1979. Early oxidation of organic matter in pelagic sediments of the eastern equatorial Atlantic: suboxic diagenesis. *Geochimica et Cosmochimica Acta* **43**, pp. 1075–1090.

Garrison R. E., Mack L. E., Lee Y. G. and Chun H. Y., 1980. Petrology, sedimentology and diagenesis of Miocene diatomaceous and opal-CT mudstones in the Pohang area, Korea. *Journal of the Geological Survey of Korea* **15**, pp. 230–252.

Goedert J. L. and Benham S. R., 2003. Biogeochemical processes at ancient methane seeps: The Bear River site in southwestern Washington. *Geological society of America, Field Guide* **4**, pp. 1–8.

Goedert J. L., Peckmann J. and Reitner J., 2000. Worm tubes in an allochthonous cold-seep carbonate from lower Oligocene rocks of western Washington. *Journal of Paleontology* **74**, pp. 992–999.

Goedert J. L. and Squires R. L., 1990. Eocene deep-sea communities in localized limestones formed by subduction-related methane seeps, southwestern Washington. *Geology* **18**, pp. 1182–1185.

Greenwood R., 1973. Cristobalite: Its relationship to chert formation in selected samples from the Depp Sea Drilling Project. *Journal of Sedimentary Petrology* **43**, pp. 700–708.

Gross G., 1965. The carbonate content of surface sediment from the northeast Pacific Ocean. *Northwest Science* **39**, pp. 85–92.

Gundersen and Mountain C. W., 1973. Oxygen utilization and pH change in ocean resulting from biological nitrate formation. *Deep-Sea Research* **20**, pp. 1083–1091.

Hagemann A., Leefmann T., Peckmann J., Hoffmann V.-E. and Thiel V., 2013. Biomarkers from individual carbonate phases of an Oligocene cold-seep deposit, Washington State, USA. *Lethaia* **46**, pp. 7–18.

Henrichs S. M. and Reeburgh W. S., 1987. Anaerobic mineralization of marine sediment organic matter: rates and the role of anaerobic processes in the oceanic carbon economy. *Geomicrobiology Journal* **5**, pp. 191–237.

Himmler T., Freiwald A., Stollhofen H. and Peckmann J., 2008. Late Carboniferous hydrocarbon-seep carbonates from the glaciomarine Dwyka Group, southern Namibia. *Palaeogeography, Palaeoclimatology, Palaeoecology* **257**, pp. 185–197.

Hinrichs K.-U., Hayes J. M., Sylva S. P., Brewert P. G. and DeLong E. F., 1999. Methane-consuming archaebacteria in marine sediments. *Nature* **398**, pp. 802–805.

Holler T., Wegener G., Niemann H., Deusner C., Ferdelman T. G., Boetius A., Brunner B. and Widdel F., 2011. Carbon and sulfur back flux during anaerobic microbial oxidation of methane and coupled sulfate reduction. *Proceedings of the National Academy of Sciences of the United States of America* **108**, pp. 1484–1490.

Hunter K. S., Wang Y. and Van Cappellen P., 1998. Kinetic modeling of microbially-driven redox chemistry of subsurface environments: Coupling transport, microbial metabolism and geochemistry. *Journal of Hydrology* **209**, pp. 53–80.

Hurd D. C., 1972. Factors affecting solution rate of biogenic opal in seawater. *Earth and Planetary Science Letters* **15**, pp. 411–417.

Hurd D. C. and Birdwhistell S., 1983. On producing a more general model for biogenic silica dissolution. *American Journal of Science* **283**, pp. 1–28.

Hurd D. C. and Theyer F., 1975. Changes in physical and chemical properties of biogenic silica from the central equatorial PAcific, Pt. I. Solubility, specific surface area and solution rate constants of acid-cleaned samples (Chap. 18). *ACS Advances in Chemistry Series* **147**, pp. 211–230.

Irwin H., Curtis C. and Coleman M., 1977. Isotopic evidence for source of diagenetic carbonates formed during burial of organic-rich sediments. *Nature* **269**, pp. 209–213.

Isaacs C. M., 1982. Influence of rock composition on kinetics of silica phase changes in the Monterey formation, Santa Barbara area, California. *Geology* **10**, pp. 304–308.

Iversen N. and Jørgensen B. B., 1985. Anaerobic methane oxidation rates at the sulfate-methane transition in marine sediments from Kattegat and Skagerrak (Denmark). *Limnology & Oceanography* **30**, pp. 944–955.

Jones J. B. and Sengit E. R., 1971. The nature of opal, I. Nomenclature and constituent phases. *Journal of the Geological Society of Australia* **18**, pp. 57–68.

Jørgensen B. B., 2006. Bacteria and marine biogeochemistry. In *Marine Geochemistry* (eds. H. Schulz and M. Zabel). Springer-Verlag Berlin Heidelberg, pp. 169–201.

Jørgensen B. B., 1977. Bacterial sulfate reduction within reduced microniches of oxidized marine sediments. *Marine Biology* **41**, pp. 7–17.

Jørgensen B. B. and Kasten S., 2006. Sulfur cycling and methane oxidation. In *Marine Geochemistry* (eds. H. Schulz and M. Zabel). Springer-Verlag Berlin Heidelberg, pp. 271–309.

Kastner M., 1981. Authigenic silicates in deep-sea sediments: Formation and Diagenesis. In *The Sea* (ed. C. Emiliani). Harvard University Press, pp. 1754.

Kastner M., Keene J. B. and Gieskes J. M., 1977. Diagenesis of siliceous oozes-I. Chemical controls on the rate of opal-A to opal-CT transformation-an experimental study. *Geochimica et Cosmochimica Acta* **41**, pp. 1041–1051,1053–1059.

Kauffman E. G., Arthur M. A., Howe B. and Scholle P. A., 1996. Widespread venting of methane-rich fluids in late Cretaceous (Campanian) submarine springs (Tepee Buttes), Western Interior Seaway, (USA). *Geology* **24**, pp. 799–802.

Kiel S., 2010. An Eldorado for Paleontologists: The Cenozoic Seeps of Western Washington State, (USA). In *Vent and Seep biota: aspects from microbes to ecosystems* (ed. S. Kiel). pp. 433–448.

Knauth L. P. and Epstein S., 1976. Hydrogen and oxygen isotope ratios in nodular and bedded cherts. *Geochimica et Cosmochimica Acta* **40**, pp. 1095–1108.

Knauth P. L., 1994. Petrogenesis of Chert. In *Reviews in Mineralogy vol. 29: Silica - Physical behavior, geochemistry and materials applications* (eds. P. J. Heaney, C. T. Prewitt, and G. V Gibbs). Mineralogical Society of America, Washington D.C. pp. 233–258.

Knittel K. and Boetius A., 2009. Anaerobic oxidation of methane: Progress with an unknown process. *Annual Reviews in Microbiology* **63**, pp. 311–334.

Knittel K., Lösekann T., Boetius A., Kort R. and Amann R., 2005. Diversity and distribution of methanotrophic archaea at cold seeps. *Applied and Environmental Microbiology* **71**, pp. 467–479.

Kuechler R. R., Birgel D., Kiel S., Freiwald A., Goedert J. L., Thiel V. and Peckmann J., 2012. Miocene methane-derived carbonates from southwestern Washington, (USA) and a model for silicification at seeps. *Lethaia* **45**, pp. 259–273.

Kulm L. D., Suess E., Moore J. C., Carson B., Lewis B. T., Ritger S. D., Kadko D. C., Thornburg T. M., Embley R. W., Rugh W. D., Massoth G. J., Langseth M. G., Cochrane G. R. and Scamman R. L., 1986. Oregon subduction zone: Venting, fauna, and carbonates. *Science* **231**, pp. 561–566.

Linke P., Wallmann K., Suess E., Hensen C. and Rehder G., 2005. In situ benthic fluxes from an intermittently active mud volcano at the Costa Rica convergent margin. *Earth and Planetary Science Letters* **235**, pp. 79–95.

Loucaides S., Koning E. and Van Cappellen P., 2012. Effect of pressure on silica solubility of diatom frustules in the oceans: Results from long-term laboratory and field incubations. *Marine Chemistry* **136-137**, pp. 1–6.

Lovley D. R., Chapelle F. H. and Phillips E. J. P., 1990. Fe(II)-reducing bacteria in deeply buried sediments of the Atlantic coastal plain. *Geology* **18**, pp. 954–957.

Luff R., Greinert J., Wallmann K., Klaucke I. and Suess E., 2005. Simulation of long-term feedbacks from authigenic carbonate crust formation at cold vent sites. *Chemical Geology* **216**, pp. 157–174.

Luff R. and Wallmann K., 2003. Fluid flow, methane fluxes, carbonate precipitation and biogeochemical turnover in gas hydrate-bearing sediments at Hydrate Ridge, Cascadia Margin: Numerical modeling and mass balances. *Geochimica et Cosmochimica Acta* **67**, pp. 3403–3421.

Luff R., Wallmann K. and Aloisi G., 2004. Numerical modeling of carbonate crust formation at cold vent sites: Significance for fluid and methane budgets and chemosynthetic biological communities. *Earth and Planetary Science Letters* **221**, pp. 337–353.

MacDonald I. R., Sager W. W. and Peccini M. B., 2003. Gas hydrate and chemosynthetic biota in mounded bathymetry at mid-slope hydrocarbon seeps: Northern Gulf of Mexico. *Marine Geology* **198**, pp. 133–158.

Mackenzie F. T. and Morse J. W., 1992. Sedimentary carbonates through Phanerozoic time. *Geochimica et Cosmochimica Acta* **56**, pp. 3281–3295.

Mackenzie F. T., Stoffyn M. and Wollast R., 1978. Aluminum in seawater: Control by biological activity. *Science* **199**, pp. 680–682.

Martens C S and Berner R. A., 1974. Methane production in the interstitial waters of sulfate depleted marine sediments. *Science* **185**, pp. 1167–1169.

Martens C S and Klump J., 1984. Biogeochemical cycling in an organic-rich coastal marine basin 4. An organic carbon budget for sediments dominated by sulfate reduction and methanogenesis. *Geochimica et Cosmochimica Acta* **48**, pp. 1987–2004.

Martens Christopher S, Haddad R. I. and Chanton J. P., 1992. Organic matter accumulation, remineralization and burial in an anoxic coastal sediment. In *Organic matter: Productivity, accumulation and preservation in recent and ancient sediments* (eds. J. K. Whelan and J. W. Farrington). Columbia University Press, New York. pp. 82–98.

Milkov A. V, Claypool G. E., Lee Y.-J. and Sassen R., 2005. Gas hydrate systems at Hydrate Ridge offshore Oregon inferred from molecular and isotopic properties of hydrate-bound and void gases. *Geochimica et Cosmochimica Acta* **69**, pp. 1007–1026.

Millero F. J. J., Yao W. and Aicher J., 1995. The speciation of Fe(II) and Fe(III) in natural waters. *Marine Chemistry* **50**, pp. 21–39.

Mogollón J. M., L'Heureux I., Dale A W and Regnier P., 2009. Methane gas-phase dynamics in marine sediments: A model study. *American Journal of Science* **309**, pp. 189–220.

Morris and Riley, 1966. The bromide/chlorinity and sulphate/chlorinity ratio in sea water. *Deep-Sea Research* **13**, pp. 699–705.

Morse J. W., Wang Q. and Tsio M. Y., 1997. Influences of temperature and Mg:Ca ratio on CaCO3 precipitates from seawater. *Geology* **25**, pp. 85–87.

Müller P. J. and Suess E., 1979. Productivity, sedimentation rate and sedimentary organic matter in the oceans - organic carbon preservation. *Deep-Sea Research* **27**, pp. 1347–1362.

Murata K. J., Friedman I. and Gleason J. D., 1977. Oxygen isotope relations between diagenetic silica minerals in Monterey Shale, Temblor Range, California. *American Journal of Science* **277**, pp. 259–272.

Murata K. J. and Norman M. B., 1976. An index of crystallinity for quartz. *American Journal of Science* **276**, pp. 1120–1130.

Nelson D. M., Treguer P., Brzezinski M. A., Leynaert A. and Queguiner B., 1995. Production and dissolution of biogenic silica in the ocean: revised global estimates, comparison with regional data and relationship to biogenic sedimentation. *Global Biogeochemical Cycle* **9**, pp. 359–372.

Neretin L. N., Böttcher M. E., Lüschen H., Jørgensen B. B., Volkov I. I. and Hilgenfeldt K., 2004. Pyritization processes and greigite formation in the advancing sulfidization front in the upper Pleistocene sediments of the Black Sea. *Geochimica et Cosmochimica Acta* **68**, pp. 2095–2118.

Neuendorf E. K., Mehl J. P. J. and Jackson J. A., 2005. *Glossary of Geology*. 5th ed., Springer-Verlag Berlin Heidelberg, Alexandria, pp. 800.

Neumann T., Rausch N., Leipe T., Dellwig O., Berner Z. and Böttcher M. E., 2005. Intense pyrite formation under low-sulfate conditions in the Achterwasser lagoon, SW Baltic Sea. *Geochimica et Cosmochimica Acta* **69**, pp. 3619–3630.

Orphan V. J., Hinrichs K.-U., Ussler III W., Paull C. K., Taylor L. T., Sylva S. P., Hayes J. M. and Delong E. F., 2001. Comparative Analysis of Methane-Oxidizing Archaea and Sulfate-Reducing Bacteria in Anoxic Marine Sediments. *Applied and Environmental Microbiology* **67**, pp. 1922–1934.

Orphan V. J., House C. H., Hinrichs K.-U., McKeegan K. D. and DeLong E. F., 2002. Multiple archaeal groups mediate methane oxidation in anoxic cold seep sediments. *Proceedings of the National Academy of Sciences of the United States of America* **99**, pp. 7663–7668.

Parkhurst D. and Appelo C., 1999. A user´s guide to PHREEQC (version 2) - A computer program for speciation, batch - reaction, one - dimensional transport and inverse geochemical calculations: Denver Colorado. *U.S. Geological Survey*, pp. 1–312.

Paull C. K., Jull A. J. T., Toolin L. J. and Linick T., 1985. Stable isotope evidence for chemosynthesis in an abyssal seep community. *Nature* **317**, pp. 709–711.

Peckmann J., Birgel D. and Kiel S., 2009. Molecular fossils reveal fluid composition and flow intensity at a Cretaceous seep. *Geology* **37**, pp. 847–850.

Peckmann J. and Goedert J. L., 2005. Geobiology of ancient and modern methane-seeps. *Palaeogeography, Palaeoclimatology, Palaeoecology* **227**, pp. 1–5.

Peckmann J., Goedert J. L. L., Heinrichs T., Hoefs J. and Reitner J., 2003. The Late Eocene "Whiskey Creek" methane-seep deposit (western Washington State). Part II: Petrology, stable isotopes, and biogeochemistry. *Facies*, pp. 241–254.

Peckmann J., Goedert J. L., Thiel V., Michaelis W. and Reitner J., 2002. A comprehensive approach to the study of methane-seep deposits from the Lincoln Creek Formation, western Washington State, (USA). *Sedimentology* **49**, pp. 855–873.

Peckmann J., Kiel S., Sandy M. R., Taylor D. G. and Goedert J. L., 2011. Mass occurrences of the Brachiopod *Halorella* in Late Triassic methane-seep deposits, Eastern Oregon. *Journal of Geology* **119**, pp. 207-220.

Peckmann J., Reimer A., Luth U., Luth C., Hansen B. T., Heinicke C., Hoefs J. and Reitner J., 2001. Methane-derived carbonates and authigenic pyrite from the northwestern Black Sea. *Marine Geology* **177**, pp. 129–150.

Peckmann J., Senowbari-Daryan B., Birgel D. and Goedert J. L., 2007. The crustacean ichnofossil Palaxius associated with callianassid body fossils in an Eocene methane-seep limestone, Humptulips Formation, Olympic Peninsula, Washington. *Lethaia* **40**, pp. 273–280.

Peckmann J. and Thiel V., 2004. Carbon cycling at ancient methane-seeps. *Chemical Geology* **205**, pp. 443–467.

Peckmann J., Thiel V., Michaelis W., Clari P., Gaillard C., Martire L. and Reitner J., 1999. Cold seep deposits of Beauvoisin (Oxfordian; southeastern France) and Marmorito (Miocene; northern Italy): Microbially induced authigenic carbonates. *International Journal of Earth Sciences* **88**, pp. 60–75.

Peckmann J., Walliser O. H., Riegel W. and Reitner J., 1999. Signatures of hydrocarbon venting in a Middle Devonian Carbonate Mound (Hollard Mound) at the Hamar Laghdad (Antiatlas, Morocco). *Facies* **40**, pp. 281–296.

Pisciotto K. A., 1981. Diagenetic trends in the siliceous facies of the Monterey Shale in the Santa Maria region, California. *Sedimentology* **28**, pp. 547–571.

Raiswell R. and Berner R. A., 1985. Pyrite formation in euxinic and semi-euxinic sediments. *American Journal of Science* **285**, pp. 710–724.

Raiswell R. and Canfield D. E., 1998. Sources of iron for pyrite formation in marine sediments. *American Journal of Science* **298**, pp. 219–245.

Reeburgh W. S., 1980. Anaerobic methane oxidation: Rate depth distributions in Skan Bay sediments. *Earth and Planetary Science Letters* **47**, pp. 345–352.

Reeburgh W. S., 1976. Methane consumption in Cariaco Trench waters and sediments. *Earth and Planetary Science Letters* **28**, pp. 337–344.

Reeburgh W. S., 2007. Oceanic methane biogeochemistry. *Chemical Reviews* **107**, pp. 486–513.

Regnier P., Dale A.W., Arndt S., LaRowe D. E., Mogollón J. and Van Cappellen P., 2011. Quantitative analysis of anaerobic oxidation of methane (AOM) in marine sediments: A modeling perspective. *Earth-Science Reviews* **106**, pp. 105–130.

Rickard D. T., Schoonen M. A. A. and Luther G. W., 1995. Kinetics of pyrite formation by the H2S oxidation of iron (II) monosulfide in aqueous solution between 25 and 125°C. In *Geochemical transformations of sedimentary sulfur.* (eds. M. A. Vairavamurthy and M. A. A. Schoonen). ACS Symposium Series, Washington D.C. pp. 168–193.

Riding R. and Liang L., 2005. Geobiology of microbial carbonates: Metazoan and seawater saturation state influences on secular trends during the Phanerozoic. *Palaeogeography, Palaeoclimatology, Palaeoecology* **219**, pp. 101–115.

Rigby J. K. and Goedert J. L., 1996. Fossil sponges from a localized cold-seep limestone in oligocene rocks of the olympic Peninsula, Washington. *Journal of Paleontology* **70**, pp. 900–908.

Ritger S., Carson B. and Suess E., 1987. Methane-derived authigenic carbonates formed by subduction-induced pore-water expulsion along the Oregon/Washington margin. *Bulletin of the Geological Society of America* **98**, pp. 147–156.

Roberts H. H. and Aharon P., 1994. Hydrocarbon-derived carbonate buildups of the northern Gulf of Mexico continental slope: A review of submersible investigations. *Geo-Marine Letters* **14**, pp. 135–148.

Robertson A. H. F., 1977. The origin and diagenesis of cherts from Cyprus. *Sedimentology* **24**, pp. 11–30.

Römer M., Sahling H., Pape T., Bohrmann G. and Spieß V., 2012. Quantification of gas bubble emissions from submarine hydrocarbon seeps at the Makran continental margin (offshore Pakistan). *Journal of Geophysical Research C: Oceans* **117**.

Rullkötter J., 2006. Organic Matter: The driving force for early diagenesis. In *Marine Geochemistry* (eds. H. Schulz and M. Zabel). Springer-Verlag Berlin Heidelberg. pp. 125–162.

Sassen R., Joye S., Sweet S. T., Defreitas D. A., Milkov A. V and MacDonald I. R., 1999. Thermogenic gas hydrates and hydrocarbon gases in complex chemosynthetic communities, Gulf of Mexico continental slope. *Organic Geochemistry* **30**, pp. 485–497.

Savard M. M., Beauchamp B. and Veizer J., 1996. Significance of aragonite cements around cretaceous marine methane seeps. *Journal of Sedimentary Research* **66**, pp. 430–438.

Schippers A. and Jørgensen B. B., 2001. Oxidation of pyrite and iron sulfide by manganese dioxide in marine sediments. *Geochimica et Cosmochimica Acta* **65**, pp. 915–922.

Schlüter M. and Rickert D., 1998. Effect of pH on the measurement of biogenic silica. *Marine Chemistry* **63**, pp. 81–92.

Schweitzer C. E. and Feldmann R. M., 2008. New eocene hydrocarbon seep decapod crustacean (Anomura: Galatheidae: Shinkaiinae) and its paleobiology. *Journal of Paleontology* **82**, pp. 1021–1029.

Sibuet M. and Olu K., 1998. Biogeography, biodiversity and fluid dependence of deep-sea cold-seep communities at active and passive margins. *Deep-Sea Research Part II: Topical Studies in Oceanography* **45**, pp. 517–567.

Squires R. L. and Goedert J. L., 1991. New late Eocene mollusks from localized limestone deposits formed by subduction-related methane seeps, southwestern Washington. *Journal of Paleontology* **65**, pp. 412–416.

Stakes D. S., Orange D., Paduan J. B., Salamy K. A. and Maher N., 1999. Cold-seeps and authigenic carbonate formation in Monterey Bay, California. *Marine Geology* **159**, pp. 93–109.

Stewart R. and Brandon M., 2004. Detrital-zircon fission-track ages for the "Hoh Formation": Implications for late Cenozoic evolution of the Cascadia subduction wedge. *Geological Society of America Bulletin* **116**, pp. 60–75.

Stumm W., 1992. *Chemistry of the solid-water interface: processes at the mineral- water and particle-water interface in natural systems*. Wiley-Interscience, New York, pp. 444.

Suess E. and Whiticar M. J., 1989. Methane-derived CO2 in pore fluids expelled from the Oregon subduction zone. *Palaeogeography, Palaeoclimatology, Palaeoecology* **71**, pp. 119–136.

Thullner M., Van Cappellen P. and Regnier P., 2005. Modeling the impact of microbial activity on redox dynamics in porous media. *Geochimica et Cosmochimica Acta* **69**, pp. 5005–5019.

Thullner M., Dale A.W. and Regnier P., 2009. Global-scale quantification of mineralization pathways in marine sediments: A reaction-transport modeling approach. *Geochemistry, Geophysics, Geosystems* **10**, art. no. Q10012.

Torres M E, Bohrmann G., Dubé T. E. and Poole F. G., 2003. Formation of modern and Paleozoic stratiform barite at cold methane seeps on continental margins. *Geology* **31**, pp. e64–e65.

Torres ME E, McManus J., Hammond D. E., De Angelis M. A., Heeschen K. U., Colbert S. L., Tryon M. D., Brown K. M. and Suess E., 2002. Fluid and chemical fluxes in and out of sediments hosting methane hydrate deposits on Hydrate Ridge, (OR), I: Hydrological provinces. *Earth and Planetary Science Letters* **201**, pp. 525–540.

Tréguer P. and Le Corre P., 1979. Ratios of nitrate, phosphate and silicate during uptake and regeneration phases of the Moroccan upwelling regime. *Deep Sea Research Part A, Oceanographic Research Papers* **26**, pp. 163–184.

Tréguer P., Nelson D. M., Van Bennekom A. J., DeMaster D. J., Leynaert A. and Quéguiner B., 1995. The silica balance in the world ocean: A reestimate. *Science* **268**, pp. 375–379.

Treude T., Boetius A., Knittel K., Wallmann K. and Jørgensen B.B., 2003. Anaerobic oxidation of methane above gas hydrates at Hydrate Ridge, NE Pacific Ocean. *Marine Ecology Progress Series* **264**, pp. 1–14.

Tucker M. E. and Wright V. P., 1990. *Carbonate Sedimentology*., Blackwell Science, pp. 498.

Van Cappellen P., 1996. Reactive surface area control of the dissolution kinetics of biogenic silica in deep-sea sediments. *Chemical Geology* **132**, pp. 125–130.

Van Cappellen P., Dixit S. and Van Beusekom J., 2002. Biogenic silica dissolution in the oceans: Reconciling experimental and field-based dissolution rates. *Global Biogeochemical Cycles* **16**, pp. 21–23.

Van Cappellen P. and Qiu L., 1997a. Biogenic silica dissolution in sediments of the Southern Ocean. I. Solubility. *Deep-Sea Research Part (II:) Topical Studies in Oceanography* **44**, pp. 1109–1128.

Van Cappellen P. and Qiu L., 1997b. Biogenic silica dissolution in sediments of the Southern Ocean. II. Kinetics. *Deep-Sea Research Part (II:) Topical Studies in Oceanography* **44**, pp. 1128–1149.

Von Rad U., Reich V. and Rosch H., 1977. Silica Diagenesis in Continental Margin Sediments off Northwest Africa. *Initial reports of the Deep Sea Drilling Project* **41**, pp. 879–905.

Wakeham S. G. and Lee C., 1989. Organic geochemistry of particulate matter in the ocean: The role of particles in oceanic sedimentary cycles. *Organic Geochemistry* **14**, pp. 83–96.

Wallmann K., Drews M., Aloisi G. and Bohrmann G., 2006. Methane discharge into the Black Sea and the global ocean via fluid flow through submarine mud volcanoes. *Earth and Planetary Science Letters* **248**, pp. 544–559.

Wallmann K., Linke P., Suess E., Bohrmann G., Sahling H., Schlüter M., Dählmann A., Lammers S., Greinert J. and Von Mirbach N., 1997. Quantifying fluid flow, solute mixing, and biogeochemical turnover at cold vents of the eastern Aleutian subduction zone. *Geochimica et Cosmochimica Acta* **61**, pp. 5209–5219.

Wang Q. and Morse J. W., 1996. Pyrite formation under conditions approximating those in anoxic sediments: I. Pathway and morphology. *Marine Chemistry* **52**, pp. 99–121.

Wang Y. and Van Cappellen P., 1996. A multicomponent reactive transport model of early diagenesis: Application to redox cycling in coastal marine sediments. *Geochimica et Cosmochimica Acta* **60**, pp. 2993–3014.

Wells R. E., 1989. Geologic map of the Cape Disappointment - Naselle River area, Pacific and Wahkiakum counties, Washington. *USGS Miscellaneous Investigations Series* **I**.

Whiticar M. J., Faber E. and Schoell M., 1986. Biogenic methane formation in marine and freshwater environments: CO2 reduction vs. acetate fermentation-Isotope evidence. *Geochimica et Cosmochimica Acta* **50**, pp. 693–709.

Wilkin R. T. and Barnes H. L., 1996. Pyrite formation by reactions of iron monosulfides with dissolved inorganic and organic sulfur species. *Geochimica et Cosmochimica Acta* **60**, pp. 4167–4179.

Wilkin R. T., Barnes H. L. and Brantley S. L., 1996. The size distribution of framboidal pyrite in modern sediments: An indicator of redox conditions. *Geochimica et Cosmochimica Acta* **60**, pp. 3897–3912.

Wilkinson B. H., Buczynski C. and Owen R. M., 1984. Chemical control of carbonate phases: implications from Upper Pennsylvanian calcite- aragonite ooids of southeastern Kansas. *Journal of Sedimentary Petrology* **54**, pp. 932–947.

Williams L. A., Parks G. A. and Crerar D. A., 1985. Silica diagenesis: I. Solubility controls. *Journal of Sedimentary Petrology* **55**, pp. 301–311.

Wirth G. S. and Gieskes J. M., 1979. The initial kinetics of the dissolution of vitreous silica in aqueous media. *Journal of Colloid And Interface Science* **68**, pp. 492–500.

Zabel M., Boetius A., Emeis K-C., Ferdelman T. G., and Spieß V., 2008. RV METEOR Cruise Report M76/L1, M76/L2, M76/L3a+b, *PROSA process Studies in the Eastern South Atlantic,* DFG Senatskommission für Ozeanogrphie, pp. 223.

Zusammenfassung

Mineralbildung gebunden an sulfatabhängige anaerobe Methanoxidation (AMO) in marinen Sedimenten ist eine der faszinierendsten Entdeckungen der Marinen Geowissenschaften der letzten Jahrzehnte und hat das Interesse der internationalen Forschungsgemeinschaft geweckt. Die Zahl der Publikationen zu diesem Thema stieg rasch an und neue Entdeckungen werden bis heute gemacht. Die Rolle von Methan in mikrobiellen und geochemischen Prozessen in marinen Sedimenten ist mittlerweile anerkannt und AMO durch Archaeen und Bakterien wird als Hauptmechanismus der Mineralfällung an Methanaustritten (sog. „seeps“ oder auch „cold-seeps“) angesehen. Diese Arbeit beschreibt die Petrographie und Geochemie von eozänen Seep-Karbonaten der Siltstone of Shoalwater Bay Formation aus Washington State, USA. Hauptziele der Arbeit sind eine petrographische Beschreibung der Mineralphasen und eine geochemische Modellierung von Mineralneubildung mit Hilfe der hydrochemischen Software PHREEQC. Zusätzlich wurde Fluoreszenzmikroskopie und Geochemie der stabilen Isotope von Sauerstoff und Kohlenstoff in den Karbonatphasen eingesetzt. Ersteres wurde angewandt, um den Gehalt an organischem Material in den Phasen abzuschätzen, letzteres um die Genese der Phasen zu rekonstruieren. Spezielles Augenmerk wurde auf die Verkieselung der untersuchten Seep-Karbonaten gelegt. Mit Hilfe der Modellierung wurden verschiedene Parameter wie pH, heterogene Reaktionen von Festphasen sowie Auflösungskinetik und Thermodynamik und die Zusammensetzung der Lösung untersucht, um Mechanismen der Silikatfällung und Lösung an Seep-Karbonaten zu identifizieren und zu verstehen. Diese Erkenntnisse wurden dann mit Beobachtungen unter dem Mikroskop (i.e. Petrographie) in Verbindung gebracht, um ein Gesamtbild der Mineralgenese zu erlangen.

Abstract

Mineral formation related to sulfate-dependent anaerobic oxidation of methane (AOM) in marine sediments is one of the most intriguing discoveries in marine geosciences of the last decades, and has subsequently triggered the interest of scientists worldwide. There has been a steady increase in publications on this topic and new discoveries are still emerging to this day. The role of methane in microbial and geochemical processes in marine sediments is increasingly recognized and AOM mediated by archaeal and bacterial communities is regarded as main mechanism triggering mineral precipitation at methane seeps. This work features a petrographical and geochemical description of Eocene cold-seep carbonates from the Siltstone of Shoalwater Bay Formation located in Washington State, USA. The approach of this work relied on petrographical thin section description and geochemical modeling using the software code PHREEQC to constrain mineral formation at the Eocene seeps. The former was complemented by fluorescence microscopy to assess the organic matter content of mineral phases, and stable carbon and oxygen isotopes to reconstruct the precipitation environment of the carbonates. Comparison of numerical simulations with PHREEQC and petrographic observations allowed me to ascertain the relevance of pH, solution composition and heterogeneous reactions with solid phases (i.e. dissolution and precipitation). The specific purpose of the model was to arrive at a mechanistic understanding of processes governing precipitation and dissolution of silica minerals, which was the main target of this work. Both methods, modelling and petrography were linked to deliver an overall picture of mineral authigenesis at this ancient seep location.

Daniel Smrzka, BSc

Email: a0547217@unet.univie.ac.at

AUSBILDUNG

Pre-school 1990 - 1991

American International School, Riyadh, Saudi Arabia

Elementary School 1991 - 1997

British International School, Riyadh, Saudi Arabia

Gymnasium 1997 - 2005

Theresianische Akademie Wien

Matura 2005

Theresianische Akademie Wien

Akademischer Grad

Bachelor of Science: 2011

Absolvierung des Studiums der Erdwissenschaften an der Universität Wien

Masterstudent 2011 - 2013

Student des Studiums „Erdwissenschaften“ an der Universität Wien

Wird im Mai 2013 abgeschlossen

BERUFSERFAHRUNG

Universität Wien 2009 - 2010

Projekt „AIP – Austrian Interfacing Project: Paleoseismology of Temelin's Near-Regional Faults": Untersuchungen einer seismischen Störungszone im Wiener Becken bei Markgrafneusiedl. Kartierungsarbeit eines sedimentologischen Profils

Österreichische Mineralölverwaltung (OMV) Februar, 2010

Hydrogeologisches und petrophysikalisches Praktikum, Autonome Region Kurdistan, Irak. Hydrogeologische Untersuchungen des Shorish Blocks, Kurdistan, Irak. Teilnahme an Kursen in wireline logging, petrophysikalischer Interpretation und Bohrlochgeologie.

SPRACHKENNTNISSE

Deutsch: Muttersprache

Englisch: Fließend, erworben durch Besuch der Britischen Schule, Saudi Arabien

Französische: Grundkenntnisse, 8 Jahre Sprachunterreich im Gymnasium

Russisch: 3 Jahre Sprachunterricht im Gymnasium

COMPUTERKENNTNISSE

Software

Microsoft Office

Corel Draw

Adobe Photoshop

Matrix laboratory (MATLAB)

Beginner's All-purpose Symbolic Instruction Code (BASIC)

Fachspezifische Software

ArcGIS	(ESRI)
Processing ModFlow	(Modellierung hydrodynamischer Prozesse)
PhreeqC	(Modellierung hydrochemischer Prozesse)
Schlumberger Petrel	(Reservoir Modellierung)